ULTRASOUND IMAGING OF CELLS USING GAS VESICLES AND PERFLUOROCARBON NANODROPLETS

A Dissertation presented to
The Academic Faculty

by

Phoebe J. Welch

In Partial Fulfillment
of the Requirements for the Degree
Doctor of Philosophy in
Bioengineering

Georgia Institute of Technology

May 2023

ULTRASOUND IMAGING OF CELLS USING GAS VESICLES AND PERFLUOROCARBON NANODROPLETS

Dr. Chengzhi Shi, Advisor
School of Mechanical Engineering
Georgia Institute of Technology

Dr. Craig R. Forest, Advisor
School of Mechanical Engineering
Georgia Institute of Technology

Dr. Costas Arvanitis
School of Mechanical Engineering
Georgia Institute of Technology

Dr. Brooks Lindsey
School of Biomedical Engineering
Georgia Institute of Technology

Dr. Lilo D. Pozzo
School of Chemical Engineering
University of Washington

Dr. Levi Wood
School of Mechanical Engineering
Georgia Institute of Technology

Date Approved: 4/14/2023

ACKNOWLEDGMENTS

I am grateful for the supportive research environments within my co-advisors' labs, Chengzhi Shi and Craig Forest, as well as the Bioengineering and Georgia Tech community as a whole. The tools, resources, and expertise available to me during my doctoral research is unrivaled, and I feel immense gratitude that I had the opportunity to work in laboratory space in the Petit Institute for Bioengineering and Biosciences.

I would like to thank my committee members, Prof. Costas Arvanitis, Prof. Brooks Lindsey, Prof. Levi Wood, and Prof. Lilo D. Pozzo for their guidance, support, and encouragement over the past few years.

Thank you to Dr. David S. Li, a kind mentor and collaborator who guided me through my first major experiments and paper revisions. You gave me countless hours of your evenings and weekends helping me debug my image analysis code. I learned so much from you about ultrasound imaging of perfluorocarbon nanodroplets and how to properly set-up and troubleshoot experiments. Thank you for everything!

Thank you to the lab members in Chengzhi Shi's lab and Craig Forest's lab, past and present, who supported me through research training, writing help, and emotional support in the form of venting sessions during lunch in our IBB office and after work at various bars and restaurants near Georgia Tech's campus. I would like to especially thank (in alphabetical order): Mohamed Badawy, Athena Chien, Dr. Steven Craig, Nina Sara

Fraticelli Guzman, Mercedes Gonzalez, John Kim, Dr. Corey Landry, Dr. Timothy Lee, Dr. Colby Lewallen, Dr. Bo Yang, and Mighten Yip. I am grateful for your friendship, camaraderie, and support throughout these past five years.

The Bioengineering program at Georgia Tech holds a special place in my heart and I feel fortunate for being a part of this community and having served in leadership roles in the Bioengineering Graduate Association (BGA). Thank you to the other leadership members in BGA, including Dan Zhang, Vishwa Vasani, Vishal Manickam, Sara Bitarafan, Yanina Kuzimich, Sam Waters, KC Jacobson, Lucinda Peng, Felicia Davenport, Yusen Zhu, Valencia Watson, Jay Wroe, Spencer Zhang, Erin Shappell, Carla Kumbale, Hyoann Choi, and Gabriela Sanchez Rodriguez. Thank you especially to Ms. Laura Paige, the backbone of the BioE program, who keeps every student on track towards success. Laura, you are an indispensable person to all BioE students and faculty, and I will miss you dearly. I will come back and visit you soon!

One of the many special things about Georgia Tech is its extensive shared user facilities, which enable the highest caliber interdisciplinary research to be conducted at this university. I was a user at many shared research facilities and had so many positive interactions with the staff members who maintained the equipment and trained all users. Thank you especially to Mr. Andrew Shaw, who managed the Optical Microscope Core, and Dr. Yolande Berta, who managed the Transmission Electron Microscope and other Materials Characterization equipment at the Paper Tricentennial Building.

Thank you to my undergraduate and high school researchers who supported my research by assisting me on many experiments. I have had the privilege of mentoring sixteen undergraduate students and three high school students in my time at Georgia Tech and have learned so much from all of them. Thank you especially to Eli Ricker and John Kim, both of whom are now Georgia Tech graduate students, who helped tremendously on our ultrasound imaging experiments, and to Matthew Johnson, Jeremy Ortmann, Jingchu Chen, and DeShea Chasko, who collaborated on 3D cell culture experiments. Best of luck to all of you, and please keep in touch!

Thank you so much to my family, Robert, Helen, and Sylvia, for listening to my graduate research endeavors during our weekly family FaceTime sessions. I felt close to you even though I was 900 miles away from home. While I will miss Atlanta dearly, I look forward to moving closer to you.

Most of all, thank you Roan. Atlanta would not have felt like home without you and our two cats, Pebble and Boba. You cheered me on in my highest moments and consoled me during my lowest lows. You drove me to and from work at every hour of the day and listened to my rants about experiment failures and paper resubmissions. I could list everything I love about you and what you have done to support me, but the page count of this thesis would double at a minimum. I love you so much and cannot wait to start the next chapter of our lives.

TABLE OF CONTENTS

ACKNOWLEDGMENTS iii
LIST OF TABLES viii
LIST OF FIGURES ix
LIST OF ABBREVIATIONS xi
SUMMARY xiv
CHAPTER 1. SUMMARY OF SPECIFIC AIMS 1
1.1 Aim 1: Refine mammalian acoustic reporter gene (mARG) integration into human cell lines using drug selection techniques ($mARG_{ds}$). 3
1.2 Aim 2: Fabricate and characterize perfluorocarbon nanodroplets designed for safe, non-destructive biomedical imaging applications. 4
1.3 Aim 3: Test feasibility of perfluorocarbon nanodroplet injection in cells via patch clamp for subsequent ultrasound imaging. 5
CHAPTER 2. ULTRASOUND CONTRAST AGENTS FOR INTRACELLULAR IMAGING APPLICATIONS 7
2.1 Ultrasound Imaging 7
2.2 Ultrasound Contrast Agents 10
2.2.1 Microbubbles as Ultrasound Contrast Agents 11
2.2.2 Gas Vesicle Ultrasound Contrast Agents 15
2.2.3 Perfluorocarbon Nanodroplets Ultrasound Contrast Agents 17
2.3 Patch Clamp for Small Molecule Delivery into Single Cells 20
CHAPTER 3. A DRUG-MEDIATED ACOUSTIC REPORTER GENE SYSTEM FOR HUMAN CELL ULTRASOUND IMAGING 22
3.1 Acoustic Reporter Genes 22
3.1.1 Abstract 22
3.1.2 Introduction 23
3.2 Materials and Methods 26
3.2.1 Maintenance of HEK293T Cells 26
3.2.2 Drug selectable mARG plasmid cloning 26
3.2.3 Development of drug selectable mARG HEK293T clonal lines 27
3.2.4 Flow Cytometry 27
3.2.5 Ultrasound Imaging and Data Analysis 29
3.2.6 Phase Contrast and Fluorescence Imaging 32
3.3 Results 32
3.3.1 Drug selectable mARG design ($mARG_{ds}$) 32
3.3.2 Development of $mARG_{ds}$ HEK293T clonal lines 33
3.3.3 Development of $mARG_{ds}$ HEK293T mixed population cell lines 35
3.4 Discussion 38
3.5 Conclusions 39
CHAPTER 4. PERFLUOROCARBON NANODROPLET DYNAMICS AFFECED BY LIPID SHELL COMPOSITION 41
4.1 Perfluorocarbon nanodroplets for ultrasound imaging 41
4.1.1 Abstract 41
4.1.2 Introduction 42
4.2 Materials and Methods 45

4.2.1 Nanodroplet fabrication and size exclusion techniques 45
4.2.2 Ultrasound imaging and calibration 49
4.2.3 Acoustic droplet vaporization characterization 51
4.2.4 Inertial cavitation characterization 52
4.2.5 Statistical analysis 54
4.3 Results and Discussion 55
4.3.1 Nanodroplet filtration 55
4.3.2 Acoustic droplet vaporization intensity vs. shell composition 58
4.3.3 Acoustic droplet vaporization duration vs. shell composition 63
4.3.4 Pressure differential between acoustic droplet vaporization onset and inertial cavitation onset 65
4.4 Conclusion 68
CHAPTER 5. NANODROPLET INJECTION INTO CELLS USING PATCH CLAMP FOR SUBSEQUENT ULTRASOUND IMAGING 70
5.1 Introduction 70
5.2 Materials and Methods 74
5.2.1 HEK293T Cell Culture on Glass Coverslips 74
5.2.2 PDMS coverslip preparation 75
5.2.3 HEK293T Cell Culture onto PDMS Coverslips 76
5.2.4 Perfluorocarbon nanodroplet fabrication via spontaneous nucleation 76
5.2.5 Nanodroplet Injection via Patch Clamp 77
5.2.6 Cell preparation for ultrasound imaging 80
5.2.7 Ultrasound Imaging Set-Up 81
5.2.8 Data Analysis 82
5.3 Results 82
5.3.1 Pressure and duration parameters for perfluorocarbon nanodroplet injection into HEK293T cells 82
5.3.2 Nanodroplet spread throughout HEK293T cells 88
5.3.3 Ultrasound imaging of intracellular PFCnDs 91
5.4 Discussion 98
5.5 Conclusions 102
CHAPTER 6. CONCLUSIONS AND FUTURE DIRECTIONS 104
6.1 Review of Findings 104
6.2 Implications and Future Directions 106
6.2.1 Gas vesicle expression in pluripotent stem cells 106
6.2.2 Super-resolution ultrasound imaging of single cells 107
6.2.3 Ultrasound contrast agents for brain imaging and therapies 110
REFERENCES 113

LIST OF TABLES

5.1 Patch clamp attempts and successes at different stages of the patch clamp process. Out of 66 patch attempts, 63 gigaseals were achieved, 55 resulted in break-ins, and 29 yielded successful nanodroplet injection. 83

5.2 Incidence of perfluorocarbon nanodroplets spread throughout HEK293T cells as a function of the farthest measured nanodroplet from injection origin. 90

LIST OF FIGURES

2.1	Microbubble dynamics under ultrasound insonation.	13
2.2	Gas vesicle dynamics within mammalian cells.	16
2.3	Perfluorocarbon nanodroplet dynamics.	18
2.4	Whole cell patch clamp configuration.	21
3.1	Design of $mARG_{ds}$ clones.	28
3.2	Experimental set-up for ultrasound imaging of $mARG_{ds}$-expressing cells.	30
3.3	Single cell $mARG_{ds}$ HEK293T cells express gas vesicles and produce ultrasound contrast.	34
3.4	Mixed population HEK293T $mARG_{ds}$ cells produce sufficient ultrasound contrast after several days of antibiotic selection and doxycycline treatment.	37
4.1	Spontaneous nucleation method of fabricating perfluorocarbon nanodroplets.	48
4.2	Methods used for B-mode image and RF data collection for acoustic droplet vaporization and inertial cavitation characterization.	54
4.3	Size exclusion techniques on perfluorocarbon nanodroplet diameters.	57
4.4	Perfluorocarbon nanodroplet size distribution vs. lipid shell composition.	58
4.5	Comparison of lipid shell PFCnD B-mode image intensity.	59
4.6	Representative duration data from one dataset depicting the differences in Mean Echo Power (MEP) across all nanodroplet types.	63
4.7	ADV and IC onset of PFCnDs is influenced by their lipid shell composition.	66
5.1	Polydopamine-treated perfluorocarbon nanodroplet uptake by HEK293T cells.	73
5.2	Methods to achieve patch clamp nanodroplet injection into HEK293T cells on glass coverslips.	79

5.3 Pressure and duration parameters yielding successful PFCnD injection via patch clamp into HEK293T cells. 85

5.4 Patch clamp nanodroplet injection procedures. 88

5.5 Distribution of perfluorocarbon nanodroplets post-patch clamp microinjection. 89

5.6 HEK293T cell morphology grown on PDMS coverslips versus glass coverslips. 92

5.7 Methods for single cell localization of nanodroplet-injected HEK293T cells on PDMS coverslips. 94

5.8 Fixed HEK293T cells on PDMS coverslips after patch clamp microinjection of perfluorocarbon nanodroplets. 95

5.9 Phase transitioning of perfluorocarbon nanodroplets after fixation in 4% paraformaldehyde. 96

5.10 Patch clamp microinjected HEK293T cell fixed on a PDMS coverslip produces ultrasound contrast. 98

5.11 Cell viability after patch clamp microinjection. 101

6.1 Non-Hermitian complementary metamaterial (NHCMM) for noninvasive ultrasonic brain imaging. 111

6.2 NHCMM matching of sloped skull conditions. 112

LIST OF ABBREVIATIONS

2-D	two dimensional
ADV	acoustic droplet vaporization
ANOVA	analysis of variance
ATP	adenosine triphosphate
B-mode	brightness mode ultrasound
BBB	blood brain barrier
bp	boiling point
BSA	bovine serum albumin
Bsd	blasticidin
c	sound speed
CaCl2	calcium chloride
CHO-K1	Chinese hamster ovary cells
cm	centimeter
CMUT	capacitive micromachined ultrasonic transducers
CT	computed tomography
dB	decibel
DI	deionized
DIC	differential interference contrast
DMEM	Dulbecco's Modified Eagle Medium
DMSO	dimethyl sulfoxide
DNA	deoxyribonucleic acid
Dox	doxycycline
DPPC	dipalmitoyl phosphatidylcholine (16:0 phosphocholine)
DSPE-mPEG2000	1,2-distearoyl-sn-glycero-3-phosphoethanolamine-N-[methoxy(polyethylene glycol)-2000] ammonium salt (i.e., 18:0 PEG2000 PE)
E. coli	Escherichia coli bacteria
EDTA	ethylenediaminetetraacetic acid
EGTA	egtazic acid
f	frequency
FACS	fluorescence activated cell sorting
FBS	fetal bovine serum
FDA	Food and Drug Administration
g	gram
G418	Geneticin
GFP	green fluorescent protein
GV	gas vesicle
Gvp	gas vesicle protein
HEK293T	human embryonic kidney 293T cell line
HEPES	N-2-hydroxyethylpiperazine-N'-2-ethanesulfonic acid
hr	hour
IC	inertial cavitation
iPSC	induced pluripotent stem cell

K-gluconate	potassium gluconate
KCl	potassium chloride
kHz	kilohertz
m	meter
M	mole
mBar	millibar
mARG	mammalian acoustic reporter gene
$mARG_{ds}$	drug-selectable mammalian acoustic reporter gene
MDA-MB-231	M.D. Anderson metastatic breast 231 cells
MEMS	microelectromechanical systems
MEP	mean echo power
mg	milligram
MgCL2	magnesium chloride
MgSO4	magnesium sulfate
MHz	megahertz
MI	mechanical index
mL	milliliter
mm	millimeter
mM	millimole
mol	mole
MPa	megapascal
MRI	magnetic resonance imaging
NA	numerical aperture
NaCl	sodium chloride
nD	nanodroplet
NHCMM	non-Hermitian complementary metamaterial
nm	nanometer
NS300	NanoSight 300
PALM	photoactivated localization microscopy
PBS	phosphate buffered saline
PCR	polymerase chain reaction
PDMS	polydimethylsiloxane
PEG	polyethylene glycol
PET	positron emission tomography
PFB	perfluorobutane
PFC	perfluorocarbon
PFCnD	perfluorocarbon nanodroplet
PFH	perfluorohexane
PFP	perfluoropentane
PNP	peak negative pressure
PRF	pulse repetition frequency
Puro	puromycin
rcf	relative centrifugal force
RF	radiofrequency
ROI	region of interest
rpm	revolutions per minute

SNR	signal to noise ratio
STORM	stochastic optical reconstruction microscopy
Tet	tetracycline
µg	microgram
µL	microliter
ULM	ultrasound localization microscopy
uULM	ultrafast ultrasound localization microscopy
µM	micromolar
µm	micrometer
US	ultrasound
UV	ultraviolet

SUMMARY

Ultrasound imaging greatly benefits from the use of contrast agents to highlight regions of the body that typically exhibit low contrast. Gas microbubbles have drastically improved blood vessel imaging, even enabling visualization of micron-scale capillaries and thus achieving super-resolution ultrasound, but their size and stability in physiological conditions have prevented microbubbles from use in cellular imaging applications. More recently, two ultrasound contrast agents are being investigated for their potential to achieve cellular imaging thanks to their smaller size and improved stability over gas microbubbles. Gas vesicles are protein nanostructures with a hollow gas core, and gene constructs called mammalian acoustic reporter genes (mARGs) were recently developed which enable gas vesicle expression in mammalian cell lines and can be used to locate cells genetically engineered with mARGs in deep tissue structures *in vivo*. Perfluorocarbon nanodroplets (PFCnDs) are a type of phase-change contrast agent that are small and stable enough to extravasate from blood vessels into surrounding tissue for ultrasound imaging or targeted drug delivery. This thesis advances the use of both gas vesicles and perfluorocarbon nanodroplets as intracellular ultrasound contrast agents for different applications of cellular imaging.

First, we examine gas vesicles and implement a way to improve gas vesicle expression yield in human cell lines. In Aim 1, we modify the original mARG construct to increase the proportion of cells that express gas vesicles by making the genes drug selectable. This modification reduces the steps required to generate a gas vesicle-expressing cell line with sufficient gas vesicle production to form ultrasound contrast

without the need to use fluorescent-activated cell sorting (FACS) or single-cell cloning. We implement these drug selectable mARGs ($mARG_{ds}$) in HEK293T cells and validate the presence of gas vesicles optically and ultrasonically. These findings simplify the process of generating gas vesicle-expressing cell lines and advance the field of acoustic reporter genes for intracellular ultrasound imaging applications.

Next, we shift our focus to PFCnDs. One cause for concern when using PFCnDs *in vivo* is the potential for inertial cavitation (IC), or rapid irreversible bubble collapse that can cause cellular damage. In Aim 2, we examine the lipid shell composition of PFCnDs to find an optimal ratio of lipid components that enable PFCnDs to generate ultrasound contrast with reduced risk of IC occurrence. This lipid shell ratio is used in all subsequent experiments involving PFCnDs. Next, we examine the feasibility of inserting nanodroplets into individual cells via patch clamp to achieve single-cell localization of these cells using ultrasound imaging. In Aim 3, we attempt to patch over 60 HEK293T cells and successfully inject nanodroplets into ~50% of these cells, noting pressure and time parameters that result in nanodroplet injection. Afterward, we develop a protocol to enable cell transfer from the patch clamp rig to an ultrasound imaging set-up for subsequent imaging of the nanodroplet-injected cells. We demonstrate proof of concept of this technique, which opens the field for not only single-cell localization, but also single-cell physiology reconstruction using super-resolution imaging techniques and long-term studies of cell migration and morphology *in vivo*.

I conclude this thesis by reflecting on the work presented in this dissertation and propose future directions and applications of gas vesicles and perfluorocarbon nanodroplets. This thesis contributes to the growing field of ultrasound contrast agents, and the studies and research findings contained within this thesis expand upon ultrasound contrast agents as tools for intracellular ultrasound imaging.

Chapter 1

SUMMARY OF SPECIFIC AIMS

Ultrasound is a safe, biocompatible, and versatile imaging modality used for various deep tissue imaging applications, including prenatal, cardiovascular, and abdominal tissue and organ imaging. While certain tissues naturally exhibit ultrasound contrast due to differences in acoustic properties, other body structures are challenging to image using ultrasound alone. As a result, ultrasound contrast agents were developed over the past 30 years to highlight certain low contrast structures. Gas microbubbles are the primary contrast agent used in the ultrasound imaging research field. These microbubbles can be injected into the bloodstream for substantially improved image contrast of blood vessels and can even be used to form super-resolved images (i.e., image resolution smaller than the diffraction limit of ultrasound) of capillaries using advanced image reconstruction techniques. While microbubble contrast agents are excellent for producing contrast in vasculature, their size (1-10 μm diameter) and stability in physiological conditions prevents them from being used for cellular imaging applications. In response to these limitations, two ultrasound contrast agents have recently emerged that can be utilized to ultrasonically image cells and tissues due to their size and stability *in vivo*: gas vesicles and perfluorocarbon nanodroplets (PFCnDs).

Gas vesicles are gas-filled protein nanostructures that naturally occur in certain species of cyanobacteria and archaea to provide buoyancy to these microorganisms. Ultrasound researchers have determined that these gas vesicles provide ultrasound contrast in liquid and tissue environments. In the past few years, research pioneered by Dr. Mikhail Shapiro and his team at the California Institute of Technology has enabled mammalian cell

lines to produce gas vesicles themselves by integrating mammalian acoustic reporter genes (mARG) into the cell genome. These mARGs hold great promise to revolutionize the field of deep tissue imaging by allowing researchers to differentiate between cell types *in vivo*, but significant work must be done to improve the efficiency in which cells express these gas vesicles to ensure that sufficient ultrasound contrast is produced by these cells.

Perfluorocarbon nanodroplets are in the same family of ultrasound contrast agents as microbubbles. While microbubbles possess a gas core that slowly diffuses out through their shell, causing the lifetime of microbubbles to be minutes long when placed in environments above room temperature, PFCnDs possess a liquid perfluorocarbon core that remains liquid even at physiological temperatures due to its superheated state. This core is surrounded by a lipid, protein, or surfactant shell which maintains its stability. While these liquid-core PFCnDs produce no ultrasound contrast, once they undergo ultrasound insonation with sufficient intensity, these nanodroplets phase change to gas microbubbles and provide contrast to their surrounding environment. After phase transitioning to microbubbles, PFCnDs can recondense back to liquid nanodroplets under the proper environmental conditions. Because of their improved stability and nanometer-scale size, PFCnDs could be a useful intracellular contrast agent for ultrasonically identifying individual cells or sparse subsets of cells. However, using intracellular PFCnDs for ultrasound imaging has not been widely studied, likely due to issues regarding biocompatibility and intracellular delivery of the PFCnDs.

The goal of this thesis is to investigate ultrasound contrast agents that can be generated by cells or delivered intracellularly for localization of a specific cell type or a particular cell, respectively. It begins by describing improvements made to the recently

developed mARG system that enabled gas vesicle production to occur in mammalian cell lines. These modifications simplify the process of creating gas vesicle-producing mammalian cell lines by making the mARG system drug selectable and inherently drug inducible; we call the new mARG system $mARG_{ds}$ for drug selectable. Next, we move towards utilizing perfluorocarbon nanodroplets for single cell imaging. We first begin by creating nanodroplets that behave more favorably to biological imaging applications by exploring the lipid shell parameter space. By altering the ratio of PEGylated and non-PEGylated lipids contained in the PFCnD lipid shell, we identify a ratio that creates PFCnDs with brighter B-mode image contrast compared to the other lipid shell compositions. This lipid shell ratio also poses less risk for inertial cavitation, the rapid and irreversible bubble collapse that can cause cellular damage. We use these nanodroplets to demonstrate proof of concept that PFCnDs can be delivered intracellularly using a precision microinjection technique called patch clamp. Once the cells are injected with PFCnDs, they can be localized on a coverslip encapsulated in a tissue-mimicking agarose phantom using ultrasound imaging.

1.1 Aim 1: Refine mammalian acoustic reporter gene (mARG) integration into human cell lines using drug selection techniques ($mARG_{ds}$).

The central hypothesis of this aim is that creating gas vesicle-producing mammalian cell lines can be simplified by making the mARG constructs drug selectable. We saw gaps in current mARG constructs and efficiency deficits in mARG expression within human cell lines and sought to improve upon these genes in two ways. First, we integrated a drug-inducible promoter directly into the mARG construct for controllable gas vesicle

expression, rather than relying on specially engineered cell lines. Next, we made each mARG plasmid drug selectable against a unique antibiotic. This resulted in cell lines with a high proportion of cells generating enough gas vesicles to produce ultrasound contrast when imaged. We integrated these drug selectable mARG genes, or $mARG_{ds}$, in HEK293T cells and demonstrated that the process to generate gas vesicle-expressing human cell lines was simplified using this new $mARG_{ds}$ system.

1.2 Aim 2: Fabricate and characterize perfluorocarbon nanodroplets designed for safe, non-destructive biomedical imaging applications.

The central hypothesis to this aim is that modifications can be made to the perfluorocarbon nanodroplet lipid shell, specifically regarding the ratio of non-PEGylated to PEGylated lipids, that will influence the nanodroplet behavior during ultrasound imaging applications. While PFCnDs are a temperature stable alternative to microbubbles, the energy required to phase transition them from liquid nanodroplets to gas microbubbles can be substantial and result in damage to surrounding tissues. While it is well documented in literature that increasing the diameters of the nanodroplets or using different perfluorocarbon cores with low boiling points (e.g., perfluorobutane (PFB), boiling point of -2^{o}C) helps reduce the pressure required for PFCnD phase transition, the impact of the encapsulating shell had not been thoroughly investigated, especially in regard to whether it influences the pressures required to induce vaporization or inertial cavitation. Therefore, we designed experiments that parametrically investigated the role of polyethylene glycol (PEG) and its influence on droplet size, ultrasound contrast, and behavior when ultrasonically insonated. Our findings revealed that PFCnDs with a 50:50 non-PEG:PEG

lipid shell ratio had the most uniformly sized droplets, produced the strongest ultrasound contrast, and had the largest pressure differential between pressures required to induce droplet vaporization and pressures at which inertial cavitation become evident.

1.3 Aim 3: Test feasibility of perfluorocarbon nanodroplet injection in cells via patch clamp for subsequent ultrasound imaging

The central hypothesis of this aim is that PFCnDs can be injected into cells using patch clamp, a precision neuroscience technique, in a repeatable manner that later enables ultrasound localization of that nanodroplet-injected cell. Previous work has demonstrated that PFCnDs can extravasate from blood vessels into tumors via large endothelial gaps for subsequent ultrasound imaging and targeted drug delivery. However, no work has been conducted on whether nanodroplets can be inserted into single cells for visualization of that cell. Because PFCnDs are a promising contrast agent with super-resolution imaging capabilities and improved stability *in vivo*, it is critical to test whether these PFCnDs can be inserted into single cells and whether those nanodroplets produce sufficient ultrasound contrast to locate the cell. The work in this aim demonstrates proof of concept that PFCnDs can be inserted into HEK293T cells using patch clamp microinjection and pressure modulation. We describe pressure and injection duration trends as well as nanodroplet distribution throughout the cell. Furthermore, we outline the steps necessary to achieve PFCnD injection in cells followed by ultrasound imaging *in situ* by culturing HEK293T cells on PDMS coverslips, rather than glass, and fixing the cells in place before inserting in an ultrasound imaging set-up. This aim culminates with the ultrasound localization of a single cell after the cell received an intracellular injection of PFCnDs via patch clamp, a

feat never before realized. We conclude this aim with future steps for researchers to take in order to make ultrasonic single cell localization and imaging easier to achieve and discuss potential biomedical imaging applications.

Chapter 2

ULTRASOUND CONTRAST AGENTS FOR INTRACELLULAR IMAGING APPLICATIONS

2.1 Ultrasound Imaging

Ultrasound imaging for medical and diagnostic purposes was first created in the late 1940's [1]. Since then, ultrasound has been used extensively to image body systems for a variety of applications, including echocardiography to study blood flow through the heart and heart valves, tumor detection in soft tissues, and prenatal imaging [2-4]. Ultrasound can be used to image such a wide variety of body tissues as it is incredibly safe, relying only on low intensity acoustic waves that can penetrate centimeters deep into body tissue. The backscattered acoustic waves returning to the ultrasound transducer are detected and images can be reconstructed in real time with good spatial (~150 micrometer) and temporal (millisecond) resolution [5,6]. Ultrasound is highly biocompatible and does not rely on ionizing radiation or harmful contrast agents in the way X-ray, computed tomography (CT), or positron emission tomography (PET) require. Furthermore, ultrasound can be made portable, and the equipment required to generate ultrasound images is significantly less expensive than equipment used for other imaging modalities, such as magnetic resonance imaging (MRI).

Ultrasound imaging uses sound waves in frequencies above human hearing capabilities (> 20 kHz) and most imaging ultrasound transducers operate between 2 – 18 MHz. For ultrasound applications requiring higher acoustic intensities, such as thermal ablation, lower frequencies (< 1.5 MHz) can be used as these are more efficient at transmitting the higher acoustic pressures into tissue required for such applications.

Piezoelectric transducers are the most common form of ultrasound transducers for medical imaging and are composed of a series of piezoelectric elements arranged in either a linear or grid pattern. Each piezoelectric element generates an acoustic wave when electrically stimulated. Conversely, an acoustic wave can stimulate each piezoelectric element and is recorded as a voltage. For therapeutic applications such as histotripsy, piezoelectric transducers can be composed of a single element with a curved aperture, which focuses the acoustic wave to generate high pressures at the focal point. The high pressure is desired for certain medical therapies as it can be used to damage and induce necrosis in targeted tissues without damaging surrounding or overlaying tissue [7]. While piezoelectric transducers are by far the most common type of ultrasound imaging transducers, capacitive micromachined ultrasonic transducers (CMUTs) are a newer form of MEMS-based ultrasound transducer and are excellent at transmitting and receiving in a broader range of ultrasound frequencies, although they cannot generate ultrasound with pressure amplitudes as high as piezoelectric transducers [8,9].

Brightness-mode ultrasound, known as B-mode, is frequently used for medical imaging and works using a pulse-echo format, where each element of the transducer transmits a pulse into tissue and records the echoes reflected from the tissue. A 2-D image is constructed by summing together these echoes across all elements in the transducer, with the brightness of the image corresponding to the amplitude of the echo [10]. The intensity reflection coefficient, α, is the ratio of the intensity of the reflected wave relative to the transmitted wave. This statement can be represented mathematically as:

$$\alpha = \frac{(Z_2 - Z_1)^2}{(Z_2 + Z_1)^2} \tag{2.1}$$

Where Z_1 and Z_2 are the acoustic impedances of the two media making up the boundary. The impedance, Z, of a material is defined as:

$$Z = \rho c \tag{2.2}$$

Where ρ is the density of the material and c is the speed of sound through the material. The speed of sound through most types of tissue are very similar and is often assumed to be 1540 m/s. As a result, the amount of reflected ultrasound at an interface is proportional to differences in density between the two media at the boundary[11].

While differences in density lead to reflected waves, and thus image contrast, too drastic of a difference can cause most of the incident waves to be reflected and none transmitted. This will result in an image with a dark acoustic shadow under a hyperechoic surface. The large difference in density is the reason why coupling gel must be used between the transducer and the subject, or the subject must be submerged in an aqueous environment. It is also the reason why ultrasound is not commonly used to image the brain (due to the presence of the skull) or lungs (due to the presence of air-filled sacs).

When operating ultrasound transducers to image *in vivo*, it is important to consider the mechanical index (MI) of the ultrasound being used as prolonged exposure to ultrasound at high intensities can cause damage to tissue due to heating or even cavitation of gas within the body. The Food and Drug Administration (FDA) created this MI index as a guideline for ultrasound imaging and is based on the pressure and frequency of the incident ultrasound wave. The MI can be calculated using the following formula:

$$MI = \frac{p}{\sqrt{f}} \tag{2.3}$$

Where p is the pressure amplitude of the incident ultrasound in MPa and f is the ultrasound's operating frequency in MHz. The MI limit for imaging applications is 1.9,

and while this can be exceeded for specific ultrasound applications such as thermal ablation of tissue using focused ultrasound, using a MI above 1.9 is not approved for the vast majority of ultrasound imaging applications. The MI becomes an important consideration when utilizing ultrasound contrast agents, which will be described in the next sections.

2.2 Ultrasound Contrast Agents

A contrast agent is a substance used to highlight a biological structure that, without the presence of the contrast agent, would be difficult to image or detect [12,13]. Contrast agents are widely used throughout various imaging modalities, originating in the early 20th century with radiological contrast agents such as barium sulfate, which can be ingested for X-ray imaging of the digestive system, or iodine-based contrast agents, which are injected into the bloodstream for vascular imaging [14,15]. While some define a contrast agent as a temporary source of contrast, the term contrast agent as used in this thesis includes genetically encodable proteins that permanently produce contrast to biological material, such as fluorescent proteins used in optical imaging or, more recently, genetically encodable gas vesicle proteins for ultrasound imaging.

Broadly speaking, all ultrasound contrast agents consist of two components: a gas core surrounded by an encapsulating shell made of lipids, proteins, surfactants, and/or polymers. In the case of perfluorocarbon nanodroplets, the core is in a liquid state until exposure to an energy source that induces a phase transition of the core from liquid to gas. The gas is what produces contrast in body structures as gas has a starkly different acoustic impedance compared to blood and tissue. Certain ultrasound contrast agents can oscillate nonlinearly under certain imaging conditions, producing harmonics and sub-harmonics of

the incident ultrasound wave. These nonlinear signals can be isolated from the surrounding, linearly scattering media using certain imaging techniques, such as pulse inversion, second harmonic, or amplitude modulation imaging, increasing image contrast further and providing an accurate representation of the contrast agent location without background signal interference.

Like most imaging modalities, ultrasound does not rely solely on contrast agents for creating images of body structures. As described in section 2.1, ultrasound can detect differences in certain types of tissue due to slight differences in tissue density. However, the development of contrast agents widely expands use cases for a particular imaging modality, and ultrasound is no exception. Excitingly, the field of ultrasound contrast agents is relatively recent, and new contrast agents and use cases for these contrast agents are growing areas of research. In this section, we will discuss the most widely used ultrasound contrast agent, gas-filled microbubbles, followed by two newer ultrasound contrast agents with significant potential: gas vesicles and perfluorocarbon nanodroplets.

2.2.1 Microbubbles as Ultrasound Contrast Agents

With the creation of microbubble contrast agents, ultrasound imaging applications have expanded significantly in the past few decades [16]. The first version of microbubble contrast agents was described in the seminal paper by Gramiak and Shah, where they injected saline into patients for echocardiographic imaging; they noted improved image contrast likely caused by gas bubbles in the saline. Microspheres filled with room air were the next version of microbubble contrast agents, but they quickly dissolved in blood and suffered from other stability issues. Coating these microbubbles in lipid or protein shells

and replacing air in the microbubble core with heavier gases like sulfur hexafluoride or perfluorocarbons decreased solubility in blood and improved their circulation lifetime *in vivo*.

Microbubble contrast agents have become a FDA-approved contrast agent [17]. These commercially available microbubble contrast agents contain low boiling point perfluorocarbon cores (e.g., octafluoropropane, bp = -36.7°C) surrounded by a lipid, protein, or polymer shell and range in size from 1-10 μm in diameter. Currently, several brands of microbubble contrast agents are widely used in clinical applications and have demonstrated their safety and efficacy time and time again [18-21]. These microbubbles scatter ultrasound both linearly and nonlinearly depending on the acoustic pressures used. At MI > 0.05, nonlinear ultrasound scattering occurs as the microbubble expands and contracts at different rates during periods of rarefaction and compression, respectively (**Fig. 2.1 a, b**) [22]. As a result, these microbubbles emit scattering ultrasound at harmonic frequencies, which nonlinear imaging techniques like pulse inversion, second harmonic, and amplitude modulation imaging, can detect and isolate to improve resolution and contrast with reduced tissue background signal [9,23,24].

At pressures exceeding MI > 1, microbubbles undergo a phenomenon called inertial cavitation (IC), which is the rapid and irreversible collapse of the bubble (**Fig. 2.1 c**). In many instances, IC can be a desirable effect. For example, if a drug is loaded or attached to the microbubble, the IC can create localized disruptions to cell and tissue membranes and enable drug uptake through the newly formed pores. This can be especially useful in transporting drugs through difficult to penetrate barriers, like the blood brain barrier. Microbubble IC can also be used for improving the efficacy of tissue histotripsy as the

cavitation increases the proportion of cells that are damaged during the process. However, if cellular/tissue structure disruption or destruction is not desirable, preventing IC from occurring is critical, and safety considerations must be factored in when using these microbubbles.

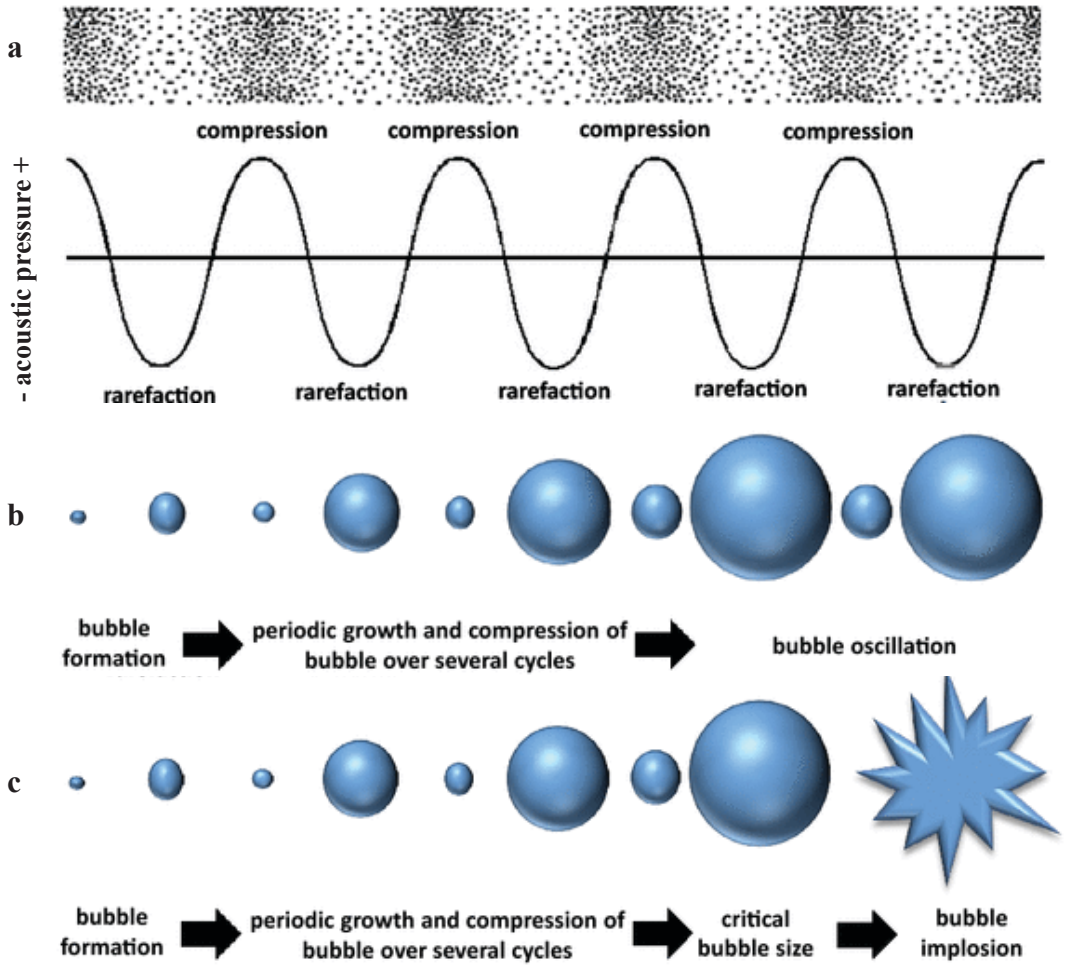

Figure 2.1. **Microbubble dynamics under ultrasound insonation. a**. Incident acoustic waves are mechanical forces with periods of compression and rarefaction, which influence microbubble behavior. **b**. At low mechanical indices (MI < 1.0) microbubbles will grow and oscillate in response to these changes in pressure. **c**. At high pressures (MI > 1.0) microbubbles can undergo inertial cavitation, or the rapid and irreversible bubble collapse. Adapted from Fig. 1 of Ref. 22.

Microbubble contrast agents can be used in several applications. Super-resolution ultrasound imaging of microvasculature in deep tissue structures including the brain, muscles, and kidneys, can be achieved using microbubbles [25-28]. By tracking microbubbles as flowing particles in a blood vessel, the precise location of each microbubble, which appears in the B-mode ultrasound image as a point spread function, can be identified; over time, an image is reconstructed as a map of all these microbubble locations. Clinically, microbubbles are useful for locating tumors in low contrast tissue due to the neovascularization phenomenon of tumors in which they rapidly recruit small microvessels to form around the tissue. Microbubbles can be functionalized with materials to target tumor angiogenesis growth factors to highlight the presence of the tumor [29-31]. Microbubbles can also be utilized for ultrasound-mediated drug delivery to blood clots and endothelial cells or for histotripsy, the non-thermal ablation of targeted tissues by focusing high pressure, short duration ultrasound pulses at tissues containing these microbubbles and inducing inertial cavitation of the microbubbles [32-34].

While there are many uses for microbubble contrast agents, there are limitations to how researchers and clinicians can implement these microbubbles. For one, their micron-scale diameter limits them to the bloodstream and they cannot extravasate into tissue via inter-endothelial gaps in blood vessels, which are typically < 2 μm [35,36]. Microbubbles are also unstable, only lasting minutes in the body before dissolution even with improved shell and core compositions [37]. As a result, microbubbles cannot be used to directly image cells or tissues as they are too large and too unstable to enter cells and remain there for durations longer than several minutes. Therefore, as researchers seek to expand the use cases of

ultrasound contrast agent imaging towards cell and tissue imaging applications, alternative contrast agents must be utilized.

2.2.2 Gas Vesicle Ultrasound Contrast Agents

An alternative ultrasound contrast agent to microbubbles has recently emerged as a potential candidate for intracellular ultrasound imaging applications in a variety of body systems. Gas vesicles are gas-filled protein nanocapsules naturally found in certain types of cyanobacteria and archaea [38]. Gas vesicles are created by these organisms to provide buoyance in aqueous environments. Within the past decade, Mikhail Shapiro has demonstrated their usefulness as ultrasound contrast agents in a variety of cells. Initially, E.coli was genetically engineered to generate gas vesicles and transplanted in mice to image the cells *in vivo* [39]. More recently, Shapiro's lab has developed a set of mammalian acoustic reporter genes (mARGs) that, in select mammalian cell lines (HEK293T, CHO-K1, and MDA-MB-231), induce gas vesicle expression without hindering cell health and development [40-42]. These gas vesicles are imaged by capturing ultrasound B-mode images of the gas vesicle-expressing cells, then transmitting ultrasound waves with sufficient intensity to collapse the gas vesicles (> 1 MPa). The collapse of gas vesicles causes a reduction in ultrasound contrast (**Fig. 2.2**). The cells and tissues containing these gas vesicles can be identified through differential image analysis. These gas vesicles can also be imaged using nonlinear ultrasound techniques, such as amplitude modulation [43-45].

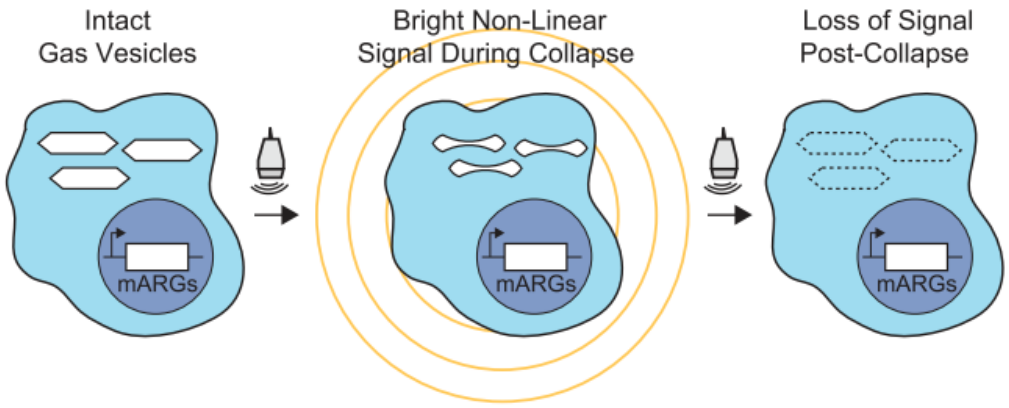

Figure 2.2: Gas vesicle dynamics within mammalian cells. When the mammalian acoustic reporter genes (mARGs) are expressed, the cell generates gas vesicles. Incident ultrasound with sufficient intensities can cause the gas vesicles to collapse, leading to a loss in signal. This collapse can be captured using either non-linear imaging techniques or by simple differential imaging. Adapted from Fig. 3 of Ref. 41.

These genes were given the name "acoustic reporter" as they highlight genetic activity within cells in a way that is ultrasonically detectable. mARGs act as an acoustic analog to fluorescent reporter genes like green fluorescent protein (GFP), which can be incorporated into plasmids and other non-host DNA sequences so that, after transferring the DNA into a cell, the cell expresses GFP along with the rest of the new gene sequences [46]. GFP and other fluorescent reporter genes have become indispensable for a variety of biological applications, but is limited in scope due to light scattering in tissue; fluorescently-tagged cells can only be detected in superficial tissue layers (< 2 mm depth) *in vivo* [47]. With mARGs, the tissue penetration is substantially improved, enabling ultrasonic detection of gas vesicle expression centimeters deep into tissue. Furthermore, since the gas vesicles are re-expressed every three days after collapse of the initial gas

vesicles, mARGs can be used for long-term imaging studies, enabling study of cellular function in deep tissue structures within intact organisms [41,48].

Currently, gas vesicle expression in mammalian cells using mARGs has only been demonstrated in certain mammalian cell strains and requires a Tet-ON promoter present in the cell line for drug-inducible (doxycycline) gas vesicle expression. Moreover, identifying cells that properly integrated the multiple plasmids required for mammalian gas vesicle expression requires significant efforts, including single cell cloning and fluorescent activated cell sorting (FACS). Modifications should be made to the generation and isolation of gas vesicle-expressing cells to improve the ratio of cells successfully expressing gas vesicles and simplify the process in which these cell lines are generated. Furthermore, implementing gas vesicle expression in other cell lines, such as stem cells, could prove extremely useful for monitoring the success of stem cell therapies and locating transplanted cells *in vivo*.

2.2.3 Perfluorocarbon Nanodroplets Ultrasound Contrast Agents

Perfluorocarbon nanodroplets (PFCnDs) are a similar ultrasound contrast agent to gas microbubbles. PFCnDs are composed of similar materials to microbubbles, a lipid, protein, or surfactant shell and perfluorocarbon core, but the core is liquid at room temperature, either because the perfluorocarbon has a high bulk vaporization temperature, or because the nanodroplets are in a superheated state [49,50]. After exposure to an ultrasound pulse with sufficient intensity, these nanodroplets phase transition into gas microbubbles and can be ultrasonically imaged using nonlinear imaging techniques for improved contrast in the liquid or tissue environment (**Fig. 2.3 a**) [51-53]. Once in a gas microbubble state, the

contrast agent can either remain as a microbubble for eventual dissolution into the surrounding environment or eliminated from the bloodstream, undergo inertial cavitation (**Fig. 2.3 b**), or recondense back into a liquid PFCnD under certain conditions, enabling repeatable ultrasound imaging of the same region.

Due to their small size, which can range from 100-500 nm in diameter, PFCnDs can extravasate into tumors via leaky vasculature, making them attractive candidates for targeted drug delivery and payload release [54-56]. Nanodroplets are also far more stable than microbubbles, lasting days *in vivo* as opposed to minutes. Additionally, PFCnDs can recondense after phase-transitioning back into a liquid nanodroplet, meaning they can be

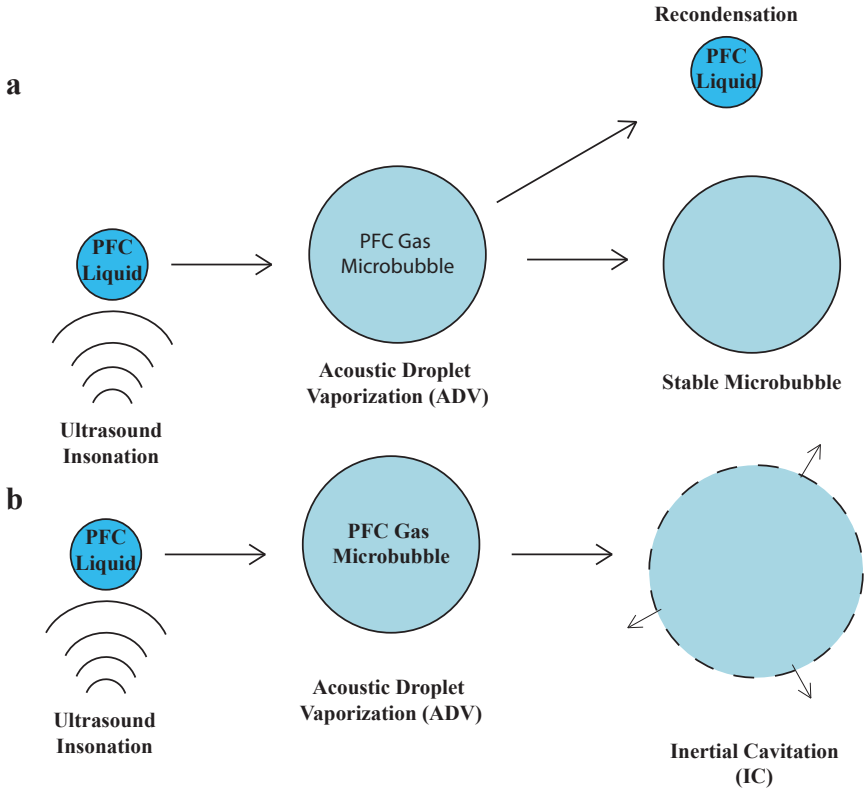

Figure 2.3 Perfluorocarbon nanodroplet dynamics. a. At lower insonation pressures, PFCnDs undergo acoustic droplet vaporization (ADV), phase transitioning from liquid nanodroplets to gas microbubbles. These phase transitioned droplets can remain as stable microbubbles or recondense back to PFCnDs under certain conditions. **b.** If insonating pressures are sufficiently high, rapid and irreversible bubble collapse can occur, also known as inertial cavitation (IC).

repeatedly imaged for long time durations (hours to several days) in the same object. This leads to PFCnDs being a potential contrast agent candidate to create an ultrasound analog to photoactivated localization microscopy (PALM) or stochastic optical recondensation microscopy (STORM). PALM and STORM are optical imaging techniques used to achieve single nanometer resolution in fluorescent images, overcoming the diffraction-limited resolution of optical imaging [57,58]. These super-resolution imaging techniques rely on fluorophores that stochastically excite and quench, which enables researchers to precisely pinpoint the location of each fluorophore so long as there is sufficient distance separating each fluorophore ($> \lambda/2$). Researchers then compile all recorded locations of each fluorophore, creating a pointillism-like image. PALM and STORM created super-resolved images with nanometer scale resolution, two orders of magnitude better than conventional fluorescent microscopy. Due to the stochastic phase-change behavior of PFCnDs and their ability to recondense, PFCnDs can behave like these PALM and STORM fluorophores and be used to create super-resolution images of cells, vasculature, and other body systems. Already, researchers are using these PFCnDs for super-resolution imaging *in vitro* and *in vivo*, and other researchers have determined that sub-micron ultrasound image resolution is feasible using contrast agents and ultrafast ultrasound localization microscopy (uULM) [59-61].

While PFCnDs improve upon microbubbles in terms of duration and stability at physiological temperatures and smaller size, there are a couple of major drawbacks that have prevented PFCnDs from greater widespread use. The pressure required to phase transition the PFCnDs from liquid droplets to gas microbubbles can exceed the MI limit outlined by the FDA for safe operation of ultrasound for biomedical imaging applications.

Furthermore, the pressure used to induce ADV can also cause some of the PFCnDs to undergo IC, inadvertently causing damage to the surrounding environment. As a result, precise control over the vaporization and cavitation conditions is crucial for certain biological and *in vivo* applications of PFCnDs.

2.3 Patch Clamp for Small Molecule Delivery into Single Cells

Patch clamp is a single cell electrophysiology technique used to measure cell activity *in vitro* and *in vivo*, particularly in neural cells, by measuring ion flow across membrane channels. A borosilicate micropipette with a 1 μm tip is filled with an internal solution with ion composition similar to that of a cell. This patch pipette is loaded onto a micro-positioner which precisely controls the movement of the pipette. A glass coverslip or tissue sample is placed in a sample holder under a microscope, and once a cell of interest is located, the tip of the patch pipette is lowered to that region. To achieve a whole-cell recording of the cell activity, the patch pipette applies gentle suction as it touches the top of the cell membrane, forming a gigaseal, or a tight seal with GΩ resistance. Once this gigaseal is achieved, short but powerful bursts of suction are applied to the pipette tip to rupture the cell membrane, allowing the internal solution of the pipette to mix with the intracellular components of the patched cell [62]. In this configuration, electrochemical activity of the cell can be recorded by the patch pipette (**Fig. 2.4**).

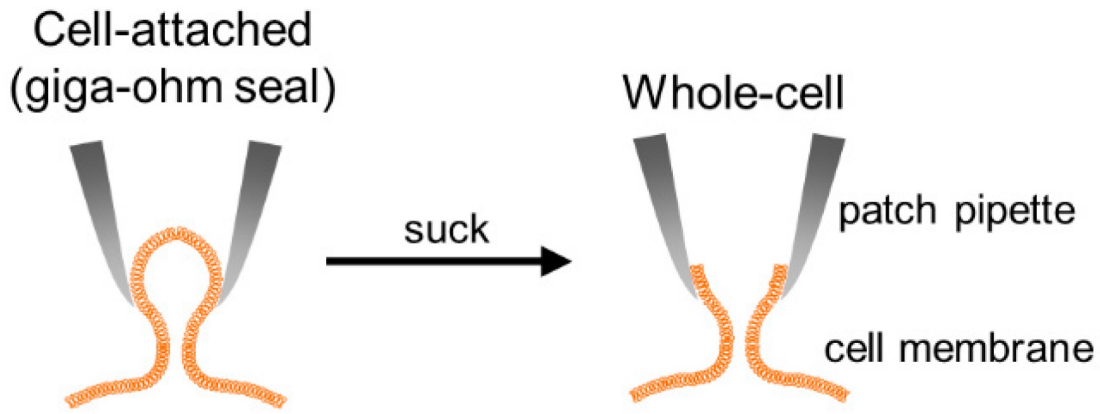

Figure 2.4: Whole cell patch clamp configuration. After the pipette is tightly sealed onto the cell of interest (left panel), brief but powerful periods of suction cause cell membrane rupture, enabling the pipette internal solution to interact with the intracellular components of the cell (right panel). Electrochemical activity of the whole cell activity is recorded in this configuration. In addition, small molecules (e.g., fluorescent dye, plasmids) contained within the patch pipette can diffuse down the concentration gradient into the cell for localization and morphology imaging optically after patch clamp experiments are complete. Figure reproduced with modifications from Ref. 62.

When patch clamping, whether in the whole cell configuration or by employing electroporation, dye and small molecules can enter the cell to locate that cell at later time points. These molecules are typically nanometer scale and can be either fluorescent stains like tdTomato or Alexa Fluor 488, or can be plasmids that cause the cell to express a genetically encoded fluorescent marker like GFP. These molecules are small enough to naturally diffuse into the cell due to the concentration gradient from the patch pipette to the cell. It has yet to be demonstrated whether patch clamp can be used to transport larger (>100 nm) structures like PFCnDs into cells, and what conditions are required to achieve this.

Chapter 3

A DRUG-MEDIATED ACOUSTIC REPORTER GENE SYSTEM FOR HUMAN CELL ULTRASOUND IMAGING

This chapter is in large part a reformatted version of the manuscript entitled "A drug-selectable acoustic reporter gene system for human cell ultrasound imaging" by Welch, P.J., Howells, A. R., Kim, J., Forest, C. R., Shi, C., and Lian, X. L. This paper was submitted for publication in Bioengineering and Translational Medicine in January 2023.

3.1 Acoustic Reporter Genes

3.1.1 Abstract

A promising new field of genetically encoded ultrasound contrast agents in the form of gas vesicles has recently emerged, which could extend the specificity of medical ultrasound imaging. However, given the delicate genetic nature of how these genes are integrated and expressed, current methods of producing gas vesicle-expressing mammalian cell lines requires significant cell processing to establish a clonal/polyclonal line that robustly expresses the gas vesicles sufficiently enough for ultrasound contrast. Here, we describe an inducible and drug-selectable acoustic reporter gene construct that can enable gas vesicle expression in mammalian cell lines, which we demonstrate using human HEK293T cells. Our drug-selectable construct design increases the stability and proportion of cells that successfully integrate all plasmids into their genome, thus reducing the amount of cell processing required. Additionally, we demonstrate that our drug-selectable strategy forgoes the need for single cell cloning or fluorescence-activated cell sorting, and that a drug selected mixed population is sufficient to generate robust ultrasound contrast.

Successful gas vesicle expression was optically and ultrasonically verified, with cells expressing gas vesicles exhibiting an 80% greater signal to noise ratio compared to negative controls and a 500% greater signal to noise ratio compared to wild type HEK293T cells. This technology presents a new reporter gene paradigm by which ultrasound can be harnessed to visualize specific cell types *in vitro* for applications including cellular reporting and cell therapies.

3.1.2 Introduction

The use of reporter genes to identify certain cell populations has become a ubiquitous laboratory technique, spanning many aspects of biological sciences. The most common demonstration of reporter genes in biological sciences are fluorescent proteins, which can be integrated into the cell for endogenous fluorescence labeling [63-66]. Hundreds of fluorophores that span nearly the entire visible spectrum have been discovered and optimized to fluoresce in response to photon absorption [67,68]. However, due to the scattering nature of tissue in the visible electromagnetic spectrum, imaging such fluorescent reporters *in vivo* is limited to several millimeters of depth in tissue or requires transparent animal models [69,70]. Alternatively, researchers utilize histology for observing tissue composition throughout the entire region of interest, but this requires animal euthanasia for tissue sectioning or biopsy, thus eliminating the opportunity for long-term *in vivo* monitoring of cell populations within the same animal [71,72].

Noninvasive imaging techniques, such as ultrasound, magnetic resonance imaging (MRI), and positron emission tomography (PET), exist in healthcare as tools to image tissue structures *in vivo* for clinical diagnostics [73]. Notably, ultrasound is a useful imaging

modality for various applications as it does not require any harmful ionizing radiation and can be achieved using relatively inexpensive and transportable equipment [74-77]. Ultrasound contrast agents can be used, such as the Food and Drug Administration-approved lipid or protein-shelled microbubbles, to improve the contrast of *in vivo* ultrasound imaging [13,25,78,79]. Newer ultrasound contrast agents, including nanobubbles and perfluorocarbon nanodroplets, are also being investigated for a variety of biomedical applications, including tumor extravasation and targeted drug delivery [54,55,80-85]. However, these newer nanodroplet and nanobubble contrast agents are still limited in their use cases as they function quite similarly to microbubbles, have limited stability *in vivo*, are not genetically encodable, and cannot currently be used to image precise locations of cells in deep tissue due to the small quantity of droplets that are taken up by cells [54,86,87]. Ideally, an ultrasound contrast agent would be developed that could be genetically encoded into cells and used as an acoustic analog to fluorescent reporter genes.

Work in the field of genetically-encodable ultrasound contrast agents has turned to gas vesicles (GVs), which many bacteria and archaea express to make these organisms buoyant in aqueous environments [38]. These nanoscale GVs are comprised of gas vesicle proteins (Gvps), which self-assemble to form a gas-filled space within the cytoplasm. Initially, GVs isolated from bacteria were shown to be a useful ultrasound contrast agent, both *in vitro* and *in vivo,* by using ultrasound pulses with sufficient pressure to induce gas vesicle collapse, causing a sudden loss in ultrasound contrast in the targeted region, or by using unique ultrasound wave patterns to isolate the nonlinear scattering of the gas vesicles from the surrounding environment [39,43-45,88]. More recently, genes encoding a specific combination of Gvps have been successfully expressed within mammalian cell lines and

form GVs, termed mammalian acoustic reporter genes (mARG) [41]. These mARGs integrate into the mammalian cell genome, and after 3 days of induced expression, the GVs generated by the cell provide ultrasound contrast sufficient to serve as a reporter of these cells. Furthermore, these cells can re-express the gas vesicles several days post-collapse [41].

Nevertheless, numerous challenges arise when developing mARGs. For one, finding a plasmid construct that generates appropriate stochiometric amounts of each individual Gvp necessary for robust GV assembly in mammalian cells proves to be challenging. Isolating the cells that have been properly transfected via random transposase integration requires single cell cloning or fluorescently activated cell sorting (FACS), a costly, inefficient, and time-consuming process. Lastly, current mARG constructs only enable inducible GV expression in Tet-On cell lines, limiting the application of this technology to engineered cells [41]. In order for the field of gas vesicle-aided ultrasound imaging to continue, it is crucial to create a universal mARG construct that is easy to integrate in a wide variety of cell types.

Here, we present our mammalian acoustic reporter gene construct that aims to improve accessibility and efficiency of this technology. We address accessibility by incorporating the doxycycline-inducible Tet-On 3G promoter into our design construct, thus enabling application of the doxycycline-inducible mARG technology into any cell line rather than only Tet-On cell lines. To address the efficiency bottleneck caused by single cell cloning and FACS, we opt to use a drug selectable strategy with several common antibiotics. We call this gene construct $mARG_{ds}$ for drug-selectable mammalian acoustic

reporter genes. We demonstrate the utility of our new $mARG_{ds}$ construct design within HEK293T cells by optically and ultrasonically validating gas vesicle expression.

3.2 Materials and Methods

3.2.1 Maintenance of HEK293T Cells

HEK293T cells were cultured in DMEM + 10% FBS (ThermoFisher) on uncoated Corning Falcon 6 well plates (Corning Inc). Complete media changes were performed daily by prewarming the DMEM + 10% FBS to 37ºC prior to aspirating and replacing old media. Passages were conducted when cells reached about 80% confluency by suspending the cells using 0.25% Trypsin-EDTA (ThermoFisher), centrifuging for 4 minutes at 1000 rpm, and sparsely replating in fresh media. Clonal stocks were frozen in DMEM + 10% DMSO + 10% FBS.

3.2.2 Drug selectable mARG plasmid cloning

DNA fragments of mARG1-1, mARG1- 2, and mARG1-3 (Addgene # 134343, 134344, 134345, respectively) were amplified using primers obtained from the In-Fusion Cloning Primer Design Tool (Takara Bio USA) and Q5 High-Fidelity DNA polymerase (New England Biolabs) according to the manufacturer's instructions. These PCR fragments were then cloned into the drug selectable XLone-GFP (Addgene #96930), XLone-Puro eGFP (Addgene #140027), and PB-UbC-GCaMP6f-polyA-PGK-Neo (Addgene #160049) plasmid backbones, respectively, using the In-Fusion® HD Cloning Kit (Takara Bio USA, Inc.), according to the manufacturer's protocol. Each newly cloned mARG plasmid cassette now possesses its own unique drug resistant gene, XLone-

mARG1-Bsd-mCherry (Blasticidin selectable, mCherry reporter), XLone-mARG2-puro-GFP (Puromycin selectable, GFP reporter), and PB-UBC-mARG3-neo (Geneticin selectable) (Addgene #s 173798, 173792, and 173793, respectively), hence the ds subscript on our $mARG_{ds}$ cassettes (**Fig. 3.1 a**).

3.2.3 Development of drug selectable mARG HEK293T clonal lines

After plasmid cloning, these 3 new plasmids were transfected into HEK293T cells via lipofection with TransIT-LT1 Transfection Reagent (Mirus Bio) at a 2.5:1 molar ratio with the EF1a-hyPBase transposase plasmid, according to manufacturer's instructions. At this point, the HEK293T cells were cultured in DMEM supplemented with Tetracycline system-approved FBS to prevent premature expression of the GV producing plasmids. Cells were then single cell cloned by sparsely passaging onto a 10 cm petri dish. Clones were manually picked and expanded. Clonal lines were analyzed using fluorescent microscopy/flow cytometry for mCherry and GFP expression after 72-hour treatment with 5 ug/mL doxycycline, 5 mM sodium butyrate, 200 ug/mL Geneticin (G418), 10 ug/mL blasticidin (Bsd), and 1 ug/mL puromycin (Puro).

3.2.4 Flow Cytometry

After 72-hour treatment with 5 ug/mL doxycycline, sodium butyrate, and drug selection media, cells were resuspended using the resuspension media described above. Negative controls did not receive doxycycline treatment. After centrifugation, cell pellets were resuspended in 800 uL of PBS + 0.5% BSA and pipetted into a cytometer flow tube. Flow for mCherry and GFP expression were performed using a BD Accuri C6 Plus flow

cytometer (BD), using the PerPC-A and FITC-A channels, respectively. Raw data was then processed using the Flowjo software (**Fig. 3.1 b**).

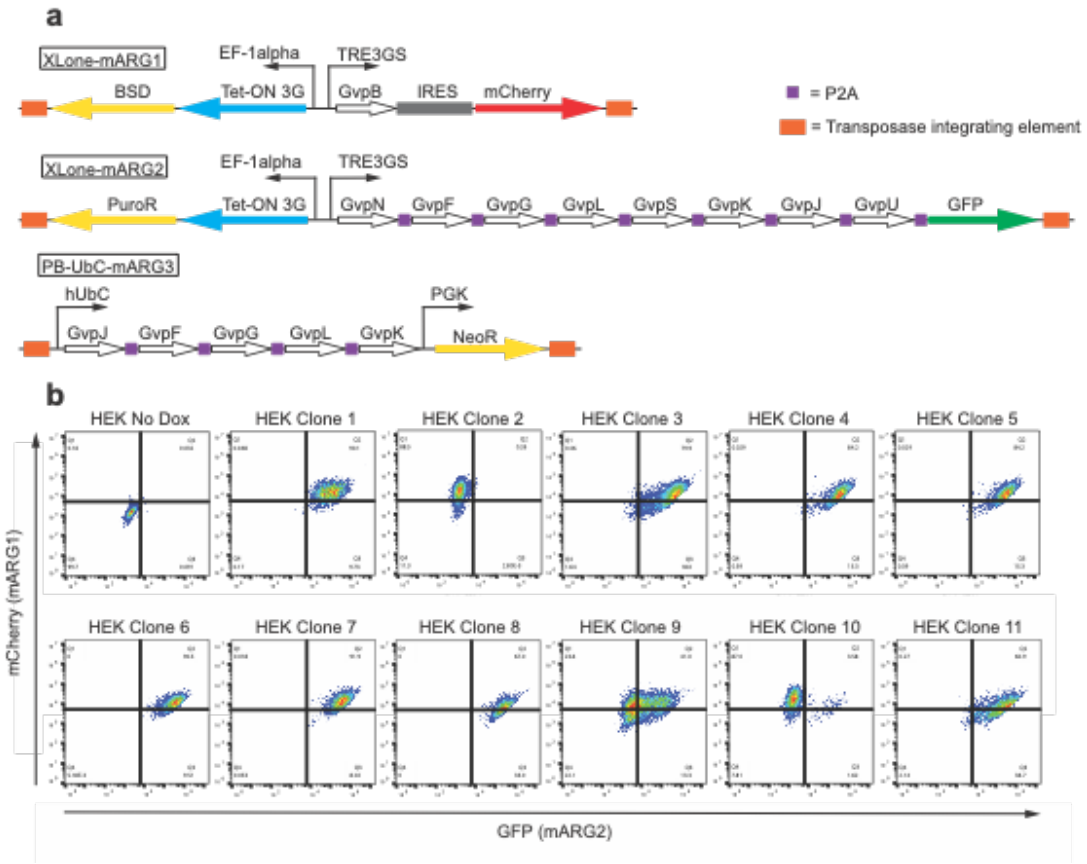

Fig. 3.1. Design of mARG$_{ds}$ HEK293T clones. a. Schematic of the transposase integrating mARG$_{ds}$ construct designs. From left to right, the XLone-mARG1 cassette possesses the Blasticidin resistant gene and the Tet-On 3G system downstream of the constitutive EF-1α promoter, and the mARG GvpB gene and mCherry downstream of the Dox inducible TRE3GS promoter. The XLone-mARG2 cassette possesses the Puromycin resistant gene and the Tet-On 3G system downstream of the constitutive EF-1α promoter, and the mARG GvpF, GvpG, GvpL, GvpS, GvpK, GvpJ, GvpU genes (separated by P2A) and GFP downstream of the Dox inducible TRE3GS promoter. Finally, PB-UbC-mARG3 cassette possesses the mARG GvpF, GvpG, GvpL, and GvpK genes downstream of the constitutive hUbC promoter and Geneticin resistant gene downstream of the constitutive PGK promoter. **b.** Flow cytometry of mARG$_{ds}$ HEK clonal lines against GFP (XLone-mARG2) and mCherry (XLone-mARG1).

3.2.5 Ultrasound Imaging and Data Analysis

On the day of experiments, cells were trypsinized, counted using a hemocytometer, and suspended in liquid, low-gelling temperature agarose (1%, ThermoFisher) at a concentration of approximately 20 million cells/mL. This agarose-cell suspension was loaded into sample holders comprised of a thin-walled plastic tube attached to a 1 mL syringe, which could then be tethered to a 3D printed syringe holder. This created a circular cross-section of cells that was easy to focus the ultrasound transducers on and localize any gas vesicle collapse during experiments. These cell samples were lowered into a 37°C heated water bath filled with degassed, deionized water. A single-element focused ultrasound transducer operating at 1.05 MHz (H-101, SonicConcepts) was fitted with a coupling cone backfilled with degassed, deionized water and focused such that the tip of the coupling cone (the focal spot of the ultrasound transducer) was aligned with the cell sample holder. This transducer sent short 10-cycle bursts of focused ultrasound with pressures ranging from 2-4 MPa peak-negative pressure. These pressures are sufficiently high to guarantee gas vesicle collapse in the cells. Lower pressures may be used as described in previous literature [89]. Orthogonal to the cell sample holder was an L22-8v CMUT linear array transducer (Kolo Medical) used to capture images of the cells and any gas vesicle collapse. This multiplexing transducer operated at its center frequency of 15.625 MHz and operated at ~300 frames per second. RF data from the linear array transducer was collected using a Vantage 256 ultrasound imaging system (Verasonics) and reconstructed later as B-mode images for analysis. The linear-array transducer and single-element transducer were synchronized such that the single-element transducer transmitted starting on specific frames numbers so that it was easy to later identify when the gas vesicle

collapse occurred. 25 pre-collapse frames and 100 post-collapse frames were captured per 10-cycle burst sine wave event (**Fig. 3.2**).

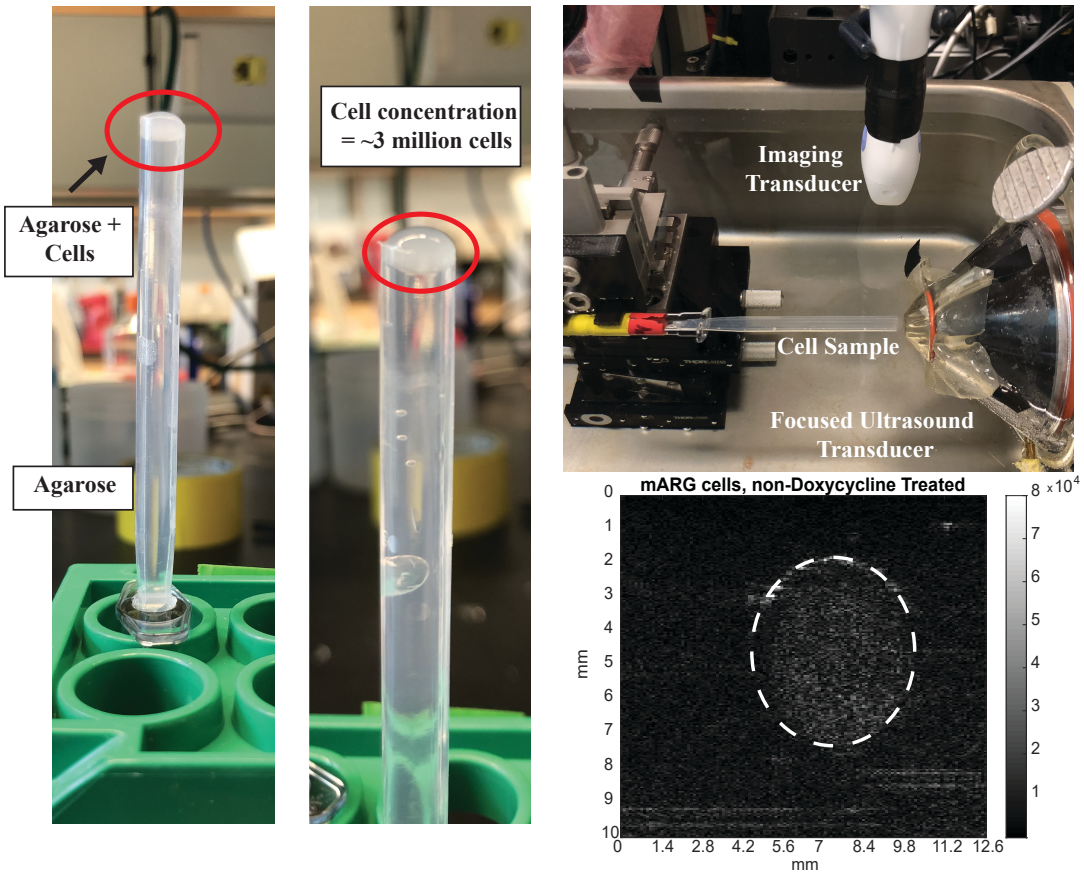

Figure 3.2. Experimental set-up for ultrasound imaging of mARG$_{ds}$-expressing cells. HEK293T cells containing the mARG$_{ds}$ sequence were suspended in 1% agarose gel at a concentration of 20 million cells/mL (~3 million cells/sample) and loaded into a plastic sample holder back-filled with 1% agarose gel (left). Once the agarose gel solidified, the sample was placed in a water bath positioned in front of a focused single element transducer (H101, SonicConcepts) which would send short, high intensity ultrasound pulses to collapse gas vesicles within the cells. Orthogonal to this set-up is an ultrasound imaging transducer (L22-8v) synchronized with the single element transducer and continuously capturing images of the gas vesicles in order to detect when gas vesicles collapse (top right). B-mode ultrasound images of cells appeared as a speckled circular structure as seen in the dashed white circle (bottom right). Differential images of this region were captured to measure gas vesicle collapse.

Gas vesicle collapse was quantified by calculating the signal to noise ratio of the cells compared to the background noise surrounding the sample in B-mode ultrasound images. Differential B-mode images were created by subtracting post-collapse ultrasound frames from previous frames. A custom MATLAB script (MathWorks) was created that calculated the signal within the circular confines of the agarose sample holder and compared it to the noise of the surrounding environment in the water bath. A circular region of interest (ROI) was drawn over the sample holder and the signal was calculated by summing and averaging all of the pixel intensities within that circular ROI. For the noise, a circular ROI was created adjacent to the sample holder and the averaged sum of that region's pixel intensities constituted the noise value. The formula used to calculate the signal to noise ratio (SNR) is:

$$SNR\ (dB) = 20 * log\ (\frac{P_{signal}}{P_{noise}}) \tag{3.1}$$

where

$$P_{Signal} = \frac{1}{MN} \sum_{i=1}^{M} \sum_{j=1}^{N} A_{Signal}^{2}\ (i,j) \tag{3.2}$$

and

$$P_{noise} = \frac{1}{MN} \sum_{i=1}^{M} \sum_{j=1}^{N} A_{noise}^{2}\ (i,j) \tag{3.3}$$

These SNR values were used to determine sufficient ultrasound contrast produced by the collapsing gas vesicles compared to negative controls. Box plots and statistical analysis were conducted in R Studio. One-way ANOVA and Tukey's t-test were used to determine statistical significance in variance between cell groups.

3.2.6 Phase Contrast and Fluorescence Imaging

Optical images were captured using Zeiss Laser Scanning Microscopes (700 and 900 Confocal, Zeiss) in the Optical Microscope Core in the Georgia Institute of Technology. HEK293T $mARG_{ds}$ cells were cultured on glass-bottomed petri dishes and treated with doxycycline for at least 24 hours before imaging occurred. To capture images of the gas vesicles, the microscope was configured to capture phase contrast images at 40x magnification. Fluorescent images were captured using 488 nm and 555 nm lasers to excite GFP and mCherry, respectively.

3.3 Results

3.3.1 Drug selectable mARG design ($mARG_{ds}$)

We set out to induce gas vesicle expression in human cells in a manner similar to the work of the Shapiro group [41], but with two key distinctions. First, while Shapiro's group utilized cell lines that constitutively expressed the Tet-On 3G system, we make the mARG gene constructs generalizable and implementable in any mammalian cell line. This will enable doxycycline-inducible gas vesicle expression in any host mammalian cells rather than requiring engineered cell lines. For the second modification, we noted in our first attempt to replicate Shapiro's work that gas vesicle formation was very low in our HEK293T clonal lines as no ultrasound signal was generated [41]. To address this issue, streamline the workflow, and increase the efficiency upon which we develop robust mARG-expressing clonal HEK lines, we made each of the three mARG cassettes drug selectable against its own unique antibiotic (**Fig. 3.1 a**).

3.3.2 Development of mARG$_{ds}$ HEK293T clonal lines

We transposase integrated the new mARG$_{ds}$ plasmids into wild type HEK293T cells. We gradually increased the G418, BSD, and Puro culture concentrations to a concentration of 200 µg/mL, 20 µg/mL, and 2 µg/mL, respectively. This mARG$_{ds}$ HEK293T population was then single cell plated and 11 clonal lines were picked and expanded. These 11 clonal lines were first treated with 5 µg/mL Dox and 5 mM sodium butyrate (to prevent epigenetic silencing) for 72 hours in the presence of the 3-antibiotic cocktail and assessed for GFP and mCherry expression via flow cytometry (PB-UbC-mARG3 cassette does not possess a reporter fluorophore). Based on this, five clones (**Fig. 3.1 b**) yielded the highest double positivity and were the focus of further characterization. These clones were expanded in 6-well plates until 90-100% confluent and integrated into ultrasound experiments after doxycycline and sodium butyrate treatment for 72 hours (**Fig 3.3 a**).

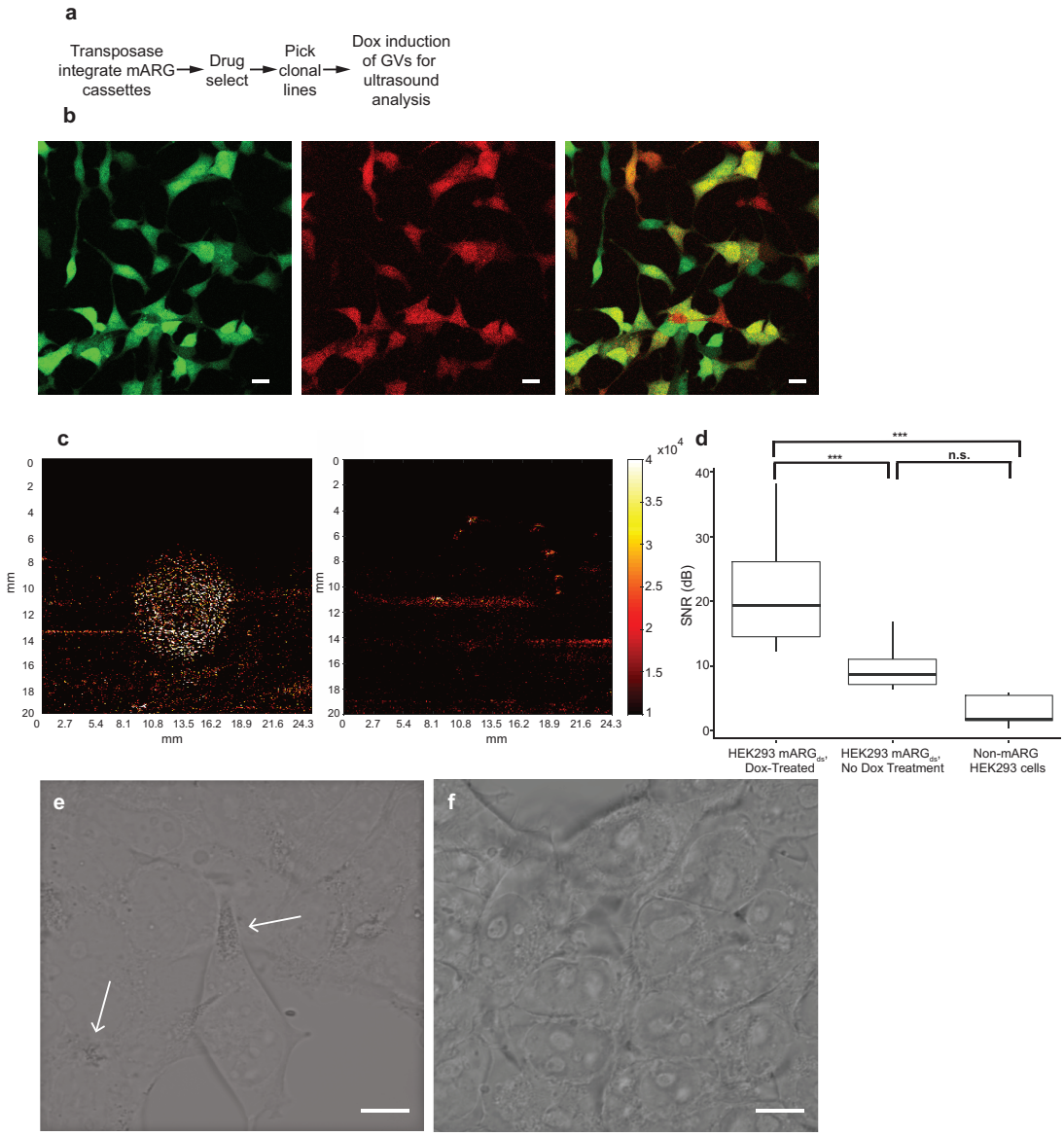

Figure 3.3. Single cell mARG$_{ds}$ HEK293T cells express gas vesicles and produce ultrasound contrast. a. Process flow for generating gas vesicle-producing single-cell clone HEK293T cell lines. **b.** Clone 6 HEK293T mARG$_{ds}$ gene expression validated by fluorescence microscopy. Scale bar = 10 µm. **c.** Ultrasound contrast is produced by doxycycline-treated HEK293T mARG$_{ds}$ single cell clones after 3 days of treatment (left panel) whereas cells not treated with doxycycline produce no ultrasound contrast (right panel). **d.** Signal to noise ratio of ultrasound imaging is significantly stronger in doxycycline-treated cells compared to non-doxycycline treated cells and non-mARG$_{ds}$ cells, indicative of gas vesicle production (n = 6). **e.** Phase contrast image of HEK293T mARG$_{ds}$ cells after three days of doxycycline treatment with small puncta spread throughout the cell (white arrows), indicative of gas vesicle presence. **f.** Phase contrast image of HEK293T mARG$_{ds}$ cells undergoing no doxycycline treatment. Scale bar = 10 µm.

Using fluorescence microscopy, we noted that clone 6 produced a high percentage of double positive fluorescent cells (**Fig. 3.3 b**). This clonal line also yielded strong ultrasound contrast in the B mode imaging based on measuring the SNR of the cell sample compared to the background noise and control groups, which included clone 6 cells cultured without doxycycline and sodium butyrate and unmodified HEK293T cell lines (**Figs. 3.3 c, d**). The average SNR from doxycycline-treated cells was 21.75 dB (125% greater than non-doxycycline treated $mARG_{ds}$ HEK293T cells) with peak values reaching 38.2 dB. Additionally, clusters of gas vesicles were observed in the doxycycline treated cells under phase contrast microscopy, whereas none were observed in the non-doxycycline treated $mARG_{ds}$ cells (**Figs. 3.3 e, f**). These results are very promising as now gas vesicle expression can likely be induced using doxycycline in numerous other mammalian cell lines, regardless of whether the cells themselves possess the Tet-On 3G system.

3.3.3 Development of $mARG_{ds}$ HEK293T mixed population cell lines

Next, we decided to determine if our drug selectable strategy alone was sufficient to generate a robust enough $mARG_{ds}$ mixed cell population that wouldn't require single cell cloning, thus further streamlining the workflow (**Fig. 3.4 a**). We took our drug selected $mARG_{ds}$ mixed population that we harvested before single cell cloning above and treated them with 5 μg/mL doxycycline and 5 mM sodium butyrate for 72 hours to induce gas vesicle expression. We found that only this single drug selection step was necessary to obtain a mixed population of cells with sufficient quantities of gas vesicle-producing cells to provide ultrasound contrast. Cells were optically validated for the expression of the

$mARG_{ds}$ genes after just 24 hours of doxycycline treatment (**Fig. 3.4 b**). When ultrasonically imaged after 72 hours of treatment, the doxycycline treated cells exhibited significantly stronger ultrasound contrast than non-doxycycline treated $mARG_{ds}$ cells as evidenced by SNR calculations (**Fig. 3.4 c, d**). The average SNR of the doxycycline-treated cells was 18.5 dB, 80% greater than the SNR of non-doxycycline treated cells and 500% stronger than the wild type HEK293T cells. Additionally, gas vesicle expression was optically observed using phase contrast imaging after 24 hours of doxycycline treatment (**Fig. 3.4 e**). Interestingly, the ultrasound contrast of non-doxycycline treated $mARG_{ds}$ mixed population cells was higher than that of non-$mARG_{ds}$ wild type HEK293T cells, and trace gas vesicles were observed in optical images of the $mARG_{ds}$ cells that were not treated with doxycycline (**Fig. 3.4 f**). Potential explanations as to why gas vesicles were present in these cells could be caused by leaky expression of the Gvps even when cultured in Tet-approved media. Regardless, this trace GV expression still resulted in a significantly lower SNR than that from the doxycycline-treated $mARG_{ds}$ cells. Based on these results, our drug selectable strategy is indeed sufficient to generate a mixed population cell line that can robustly express $mARG_{ds}$, eliminating the need for FACS or single cell cloning.

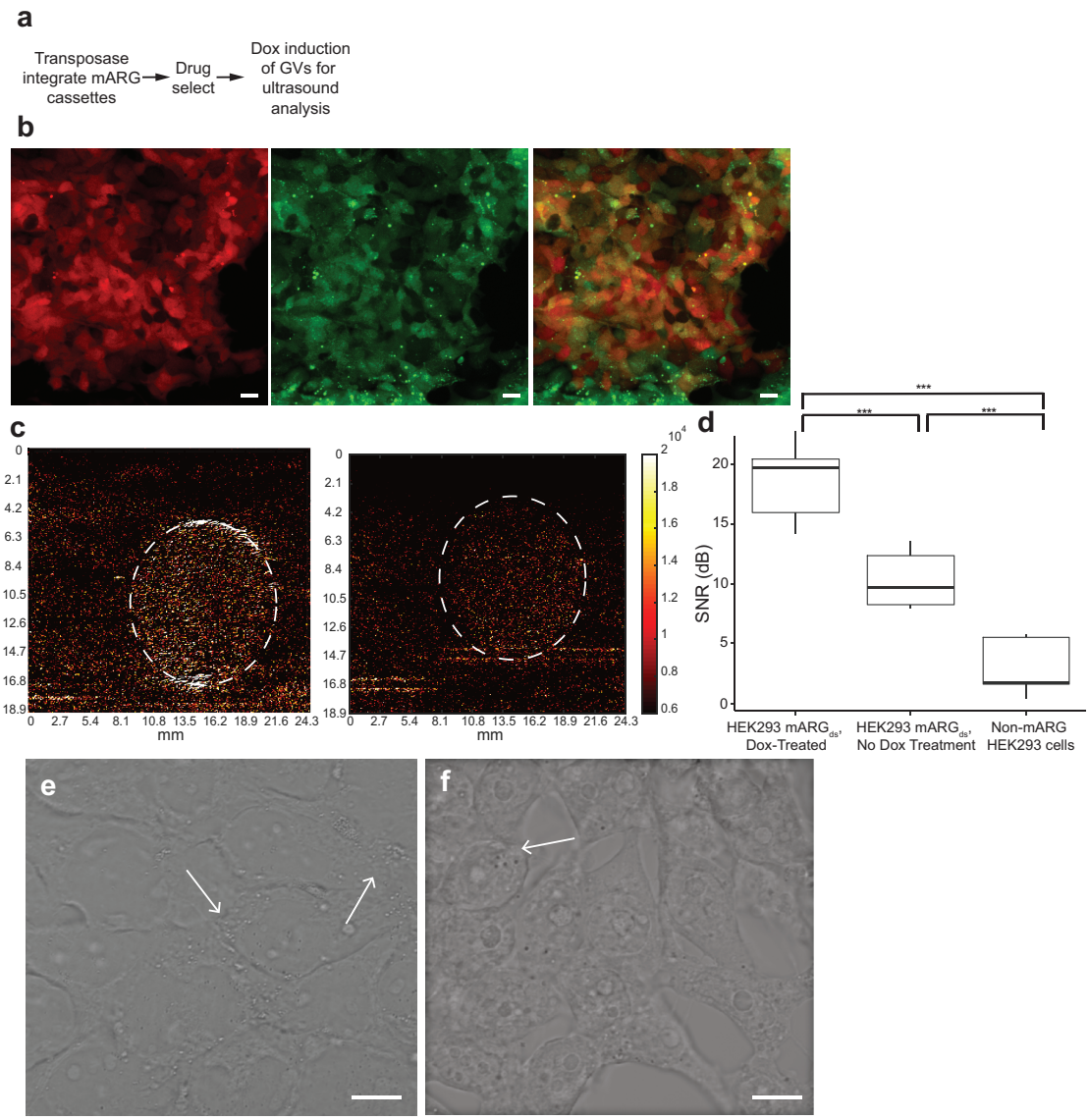

Figure 3.4. Mixed population HEK293T mARG$_{ds}$ cells produce sufficient ultrasound contrast after several days of antibiotic selection and doxycycline treatment. a. Process flow for generating gas vesicle-producing mixed population HEK293T cells. **b.** antibiotic selected and doxycycline-treated HEK293T mARG$_{ds}$ mixed population cells properly integrated the mARG$_{ds}$ genes. Scale bar = 10 µm. **c.** Doxycycline-treated HEK293T mARG$_{ds}$ mixed population cells produce stronger ultrasound contrast (left panel) compared to non-doxycycline treated mARG$_{ds}$ mixed population cells. **d.** mARG$_{ds}$ mixed population HEK293T cells exhibit a stronger signal to noise (SNR) ratio after 3 days of doxycycline treatment compared to non-doxycycline treated mARG$_{ds}$ cells and non-mARG cells (n = 7). **e.** Phase contrast image of HEK293T mARG$_{ds}$ cells after 24 hours of doxycycline treatment with small puncta spread throughout the cell (white arrows), indicative of gas vesicle presence. **f.** Phase contrast image of HEK293T mARG$_{ds}$ cells undergoing no doxycycline treatment. Small puncta are still present (white arrows), though in much smaller quantities than doxycycline-treated cells. Scale bar = 10 µm.

3.4 Discussion

Here we demonstrate expression of drug-selectable mARGs, labeled $mARG_{ds}$, within HEK293T cells. Our strategy incorporates the Tet-On 3G system, enabling doxycycline-inducible expression of the $mARG_{ds}$ into any wild type mammalian cell line. As the mARG design stands from the Shapiro group, drug-inducible mARG integration into mammalian cells is relegated to cell lines that already have the Tet-On 3G system integrated into their genome. Our strategy broadens its application potential without the need to genetically integrate the Tet-ON 3G system prior. Additionally, our $mARG_{ds}$ construct design incorporates unique drug resistant genes downstream of each of the three mARG cassettes. By culturing these cells in the antibiotic cocktail, it enables us to purify cells that have successfully integrated all 3 $mARG_{ds}$ cassettes, forgoing the need for FACS or single cell cloning.

The $mARG_{ds}$ system builds upon the work established by Mikhail Shapiro's group which created the original mARG gene constructs [41]. Their findings demonstrated successful integration of gas vesicle protein genes derived from bacterial strains into mammalian cells, specifically HEK293T and Chinese hamster ovary cells (CHO-K1). They also created mammalian cell lines with doxycycline-inducible gas vesicle expression by using transformed cell lines, specifically HEK293 Tet-On 3G cells, which are engineered to express the tetracycline-regulated transactivator Tet-On 3G. However, generating these cells had notably low throughput, requiring the use of FACS and single-cell cloning to identify triple-positive fluorescent cells and determine which of those generated gas vesicles after doxycycline treatment. To improve throughput without relying on various cell separating techniques, we made each of the three mARG plasmids drug

selectable against a unique antibiotic. Additionally, we directly integrated the Tet-On 3G promoter into the mARG construct, meaning doxycycline-induced gas vesicle expression could be achieved in wild type cells. We elected to integrate these $mARG_{ds}$ plasmids in HEK293T cells as HEK293T cells are frequently used in cell engineering applications.

Due to the delicate nature of how each Gvp must be expressed in a narrow stoichiometric ratio for them to self-assemble together to correctly form the GVs, the efficiency at which you can generate a mARG clonal lines that robustly expresses many GVs is extremely low. Based on Farhadi et al., 6/30 HEK clonal lines generated greater than 1 GV per cell, and as reported, 1 of these 30 clonal lines generated about 45 GVs per cell [16]. Every nuanced attempt at further increasing the efficiency by which researchers can generate these cells that have integrated all 3 mARG constructs is essential for furthering the application of mARGs.

3.5 Conclusions

We developed a new series of mammalian acoustic reporter genes plasmids that are drug selectable to improve the success rate of gas vesicle expression in mammalian cell lines. These $mARG_{ds}$ plasmids also have the Tet-On system integrated in the plasmid backbone, which means doxycycline-inducible gas vesicle expression can be implemented in wild type (not constitutively expressing Tet-On) cells. In this study, we integrated our $mARG_{ds}$ design in wild type HEK293T cells and prevented gene silencing of all 3 cassettes by continually culturing them in the presence of the drug cocktail. The $mARG_{ds}$ genes streamlined the workflow for developing $mARG_{ds}$ clonal HEK293T lines by eliminating the need for FACS mediated purification of cell populations that had successfully

integrated all 3 cassettes, as evidenced by ultrasonic and optical imaging. Finally, we demonstrate that our $mARG_{ds}$ construct strategy does not require the establishment of mARG clonal lines, and a drug selected mixed population of cells is sufficient for ultrasound contrast generation. The findings detailed in this manuscript indicate that doxycycline-inducible gas vesicle expression can be broadly applied to a variety of mammalian cell lines, rendering these acoustic reporter genes useful for various applications such as cell transplantation and tissue grafting.

Chapter 4

PERFLUOROCARBON NANODROPLET DYNAMICS AFFECED BY LIPID SHELL COMPOSITION

This chapter is in large part a reformatted version of the manuscript entitled "Perfluorocarbon nanodroplet size, acoustic vaporization, and inertial cavitation affected by lipid shell composition *in vitro*" published by Welch, P. J., Li, D. S., Forest, C. R., Pozzo, L. D., and Shi, C. in *Journal for the Acoustical Society of America (JASA)*.

4.1 Perfluorocarbon nanodroplets for ultrasound imaging

4.1.1 Abstract

Perfluorocarbon nanodroplets (PFCnDs) are ultrasound contrast agents that phase-transition from liquid nanodroplets to gas microbubbles when activated by laser irradiation or insonated with an ultrasound pulse. The dynamics of PFCnDs can vary drastically depending on the nanodroplet composition, including the lipid shell properties. In this paper, we investigate the effect of varying the ratio of PEGylated to non-PEGylated phospholipids in the outer shell of PFCnDs on the acoustic nanodroplet vaporization (liquid to gas phase transition) and inertial cavitation (rapid collapse of the vaporized nanodroplets) dynamics *in vitro* when insonated with focused ultrasound. Nanodroplets with a high concentration of PEGylated lipids had larger diameters and exhibited greater variance in size distribution compared to nanodroplets with lower proportions of PEGylated lipids in the lipid shell. PFCnDs with a lipid shell composed of 50:50 non-PEGylated to PEGylated lipids yielded the highest B-mode image intensity and duration, as well as the greatest pressure difference between acoustic droplet vaporization onset and

inertial cavitation onset. We demonstrate that slight changes in lipid shell composition of PFCnDs can significantly impact droplet phase transitioning and inertial cavitation dynamics. These findings can help guide researchers to fabricate PFCnDs with optimized compositions for their specific applications.

4.1.2 Introduction

Lipid-shelled microbubbles have been used as FDA approved ultrasound contrast agents for several decades [90-92]. These gaseous structures ranging in size from 1-5 μm in diameter can be injected into the bloodstream and provide contrast for imaging the blood and tissue environment within the body. Furthermore, these microbubbles scatter ultrasound nonlinearly, which enables improved resolution and high contrast images with less tissue background signal [93]. The use of microbubbles has enabled super-resolution ultrasound imaging of microvasculature in deep tissue structures, including the brain, muscles, and kidney [25-28]. Microbubbles can also be utilized for ultrasound-mediated drug delivery to blood clots and endothelial cells [32,33]. However, there are several drawbacks to microbubble contrast agents. Their size limits them to the bloodstream and they cannot extravasate into tissue via inter-endothelial gaps in blood vessels [35]. Microbubbles are also unstable, only lasting minutes in the body before dissolution [37]. In response to these issues, perfluorocarbon nanodroplets (PFCnDs) have been developed composed of similar materials, a lipid shell and perfluorocarbon core, but the nanodroplet core is liquid at room temperature, either because the perfluorocarbon core has a high bulk vaporization temperature, or because the nanodroplets are in a superheated state [49,50]. After exposure to an ultrasound pulse with sufficient energy, these nanodroplets phase transition into gas

microbubbles and can be ultrasonically imaged using nonlinear imaging techniques for improved contrast in the liquid or tissue environment [51-53]. Depending on environmental conditions and nanodroplet composition, such as the choice of perfluorocarbon used and temperature of the nanodroplet suspension, the PFCnDs can recondense back to a liquid state and undergo the expansion-recondensation cycle for repeated imaging purposes, or can remain as gas microbubbles and be eliminated from the body within minutes to hours [60,94,95]. Due to their small size (<300 nm) they can extravasate into the leaky vasculature of tumors, which have large inter-endothelial gaps ranging from 380 nm – 2 μm [55,96,97]. PFCnDs also exhibit significantly better stability in circulation; compared to microbubbles whose lifespan is minutes long, PFCnDs with perfluoropentane (PFP) or perfluorohexane (PFH) cores remain stable in their liquid state for hours to days *in vitro* and *in vivo* [84,98-100]. PFCnDs can be utilized for targeted drug delivery and are superior for selective tissue ablation as they facilitate targeted, deep tissue heating without prefocal thermal delivery and damage to skin that occurs when using microbubbles [55,56,101,102]. Furthermore, due to their nanoscale size, functionalized PFCnDs can enter specific cell types via endocytosis for localized cell and tissue ablation; microbubbles are neither small nor stable enough for such applications [86].

The process of PFCnDs transitioning from liquid nanodroplets to gaseous microbubbles from an ultrasound pulse is termed acoustic droplet vaporization (ADV). The pressure at which the nanodroplets undergo ADV can vary significantly based on several nanodroplet properties: nanodroplet diameter, core composition, and shell composition [103-105]. These nanodroplet properties also affect inertial cavitation (IC) of PFCnDs, which is unstable bubble collapse with a broadband noise signature [106]. So long as the core bulk

boiling point of PFCnDs is lower than the temperature of its surrounding environment, ADV and IC of PFCnDs are serially linked to one another, with ADV occurring first to form gas microbubbles before IC occurs in those microbubbles, although ADV and IC pressure thresholds can overlap [107,108]. Preventing IC from occurring while using PFCnDs and microbubbles as ultrasound contrast agents is particularly crucial for *in vivo* imaging due to its potential to cause significant damage to surrounding tissues; therefore, having a large pressure difference between ADV onset and IC onset is of importance to medical imaging researchers.

Previous studies have demonstrated that nanodroplet size, stability, and image contrast are heavily reliant on their lipid shell composition. Mountford et al. (2015) studied PFCnDs composed of phospholipid shells with acyl lengths ranging from C14 to C24 and noted that the energy required to induce phase transitioning linearly trended with increasing acyl length chain [109]. Yarmoska et al. (2019) showed that increasing the ratio of PEGylated to non-PEGylated lipids in photoacoustic PFCnDs yielded smaller nanodroplets with smaller standard deviations and stronger photoacoustic signals compared to PFCnDs with higher ratios of non-PEGylated to PEGylated lipids [104]. Chattaraj et al. (2016) noted that different combinations of saturated and unsaturated phospholipids in combination with cholesterol affected the B-mode acoustic intensity of perfluorohexane-core PFCnDs, possibly due to the clustering and phases of the lipid shells [110]. From these papers, slight changes in lipid shell composition, like the carbon chain lengths or the ratio of different phospholipids and surfactants, can significantly impact size distribution and ultrasound image contrast. However, there is limited research on how the lipid shell impacts

ultrasonically induced phase-transitioning of PFCnDs and whether the shell composition influences the inertial cavitation threshold.

In this work, we investigated the role of varying lipid shell composition of PFCnDs on nanodroplet size, ADV and IC onset, and the ultrasound intensity and duration of phase-transitioned PFCnDs by varying the ratio of PEGylated and non-PEGylated lipids, which are commonly used for fabricating lipid-shelled ultrasound contrast agents. These nanodroplets had cores composed of either PFP, PFH, or a combination of the two perfluorocarbons. These perfluorocarbons were selected to encourage recondensation of the phase-transitioned nanodroplets; using perfluorocarbons with lower boiling points like perfluorobutane (PFB, boiling point = -2°C) would result in microbubbles unable to recondense in the water bath heated to 37°C. PFCnDs fabricated via spontaneous nucleation were suspended in agarose hydrogels and insonated using a focused ultrasound transducer. A linear array transducer, synchronized to the focused ultrasound transducer, captured B-mode images and radiofrequency (RF) data of the insonated PFCnDs, which were used to study the vaporization and cavitation dynamics of the nanodroplets, respectively.

4.2 Materials and Methods

4.2.1 Nanodroplet fabrication and size exclusion techniques

Nanodroplets were fabricated using a spontaneous nucleation method as previously described by Li et al. (**Fig. 4.1 a**) [84]. This fabrication method was used as it can consistently create small (< 250 nm diameter), uniform PFCnDs with no need for specialized equipment nor harmful chemicals like chloroform. Lipid stock solutions were

created with varying molar ratios of 1,2-dipalmitoyl-sn-glycero-3-phosphocholine (DPPC) and N-(carbonyl-methoxypolyethylyeneglycol 2000)-1,2-distearoyl-sn-glycero-3-phosphoethanolamine (DSPE-PEG_{2000}) (NOF America Corporation) dissolved in 190 proof ethanol. These lipid stocks were composed of 90:10 DPPC:DSPE-PEG_{2000}, 50:50 DPPC:DSPE-PEG_{2000}, or 10:90 DPPC:DSPE-PEG_{2000} (**Fig 4.1 b**). The final concentration of lipids in these solutions was 2 μM. One milliliter of each stock solution was added to a microcentrifuge tube and perfluorocarbons, either perfluoropentane (PFP; FluoroMed L.P.), perfluorohexane (PFH; FluoroMed L.P.), or a combination of the two, were added to the lipid solutions until the solution was saturated with perfluorocarbon, as characterized by a noticeable pellet of undissolved perfluorocarbon collected at the bottom of the microcentrifuge tube. The ratios of PFP:PFH used in these experiments were as follows: 100:0, 90:10, 70:30, 50:50, and 0:100. We ultimately want to create nanodroplets that will phase transition under diagnostically safe acoustic pressures (mechanical index (MI) below 1.9) while also being capable of recondensing back into a liquid state, so the nanodroplets fabricated tended to have a higher ratio of PFP to PFH, and 30:70 and 10:90 PFP:PFH nanodroplets were not included in this study [111]. A 2% solution of DiI (a lipophilic fluorescent tracer; MilliporeSigma) dissolved in ethanol was added to the lipid/perfluorocarbon solution. DiI was used in all experiments as these PFCnDs with this composition will later be used in cell and tissue imaging studies. The microcentrifuge tube was vortex mixed and sonicated until the solution was cloudy. At this point, the solution was left for 20 min for additional undissolved perfluorocarbon to fall out of solution. 50 μL of this lipid/PFC/DiI solution were added to 100 μL of lipid stock solution in microcentrifuge tubes. Then, 850 μL of a 7:2:1 water:propylene glycol:glycerol

(MilliporeSigma) solution was added to the diluted lipid/PFC solutions. The rapid addition of this hydrophilic miscible solution caused the dissolved lipids and PFC to spontaneously nucleate into very small droplets with the lipid encapsulating the PFC 'core' to form a stable dispersion in a process called spontaneous emulsification. From here, all samples were centrifuged for 80 min at 6000 rcf, the supernatant was removed, and the pellet of nanodroplets was resuspended in phosphate buffered saline (PBS; Corning).

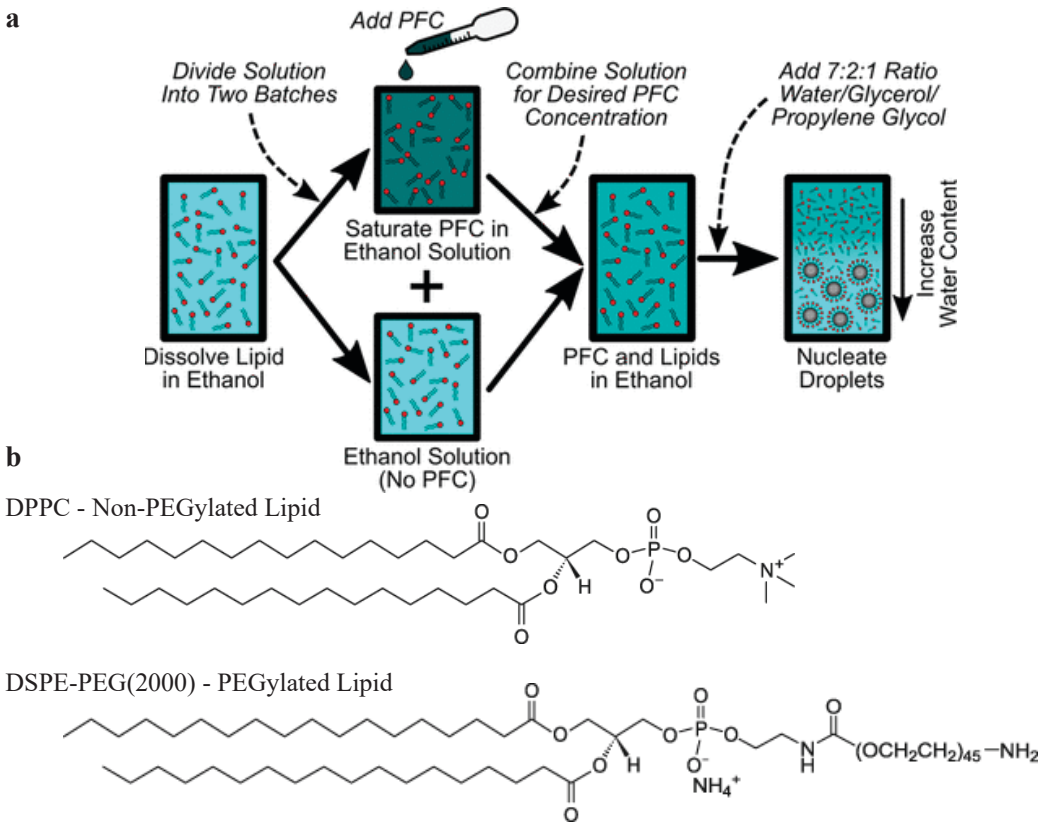

Figure 4.1: Spontaneous nucleation method of fabricating perfluorocarbon nanodroplets. **a.** Lipids are first dissolved in ethanol, then divided into two batches. Perfluorocarbons (PFC) are slowly added to the first batch of lipids + ethanol until the solution is saturated with PFC, indicated by the formation of a pellet of undissolved PFC at the bottom of the vessel. The second batch of lipids + ethanol remains unchanged. The two solutions are added together in a ratio conducive for desired PFC concentration. In the final step, a 7:2:1 water:propylene glycol:glycerol solution is added to the lipids + ethanol + PFC solution. The rapid addition of a hydrophilic solution to a hydrophobic solution causes spontaneous nucleation to occur, where the lipids in the suspension rapidly seize into small droplets, encapsulating PFC during this process. **b.** Schematic of the non-PEGylated and PEGylated lipids used in this work. Figure 4.1a adapted from Ref. 84.

To test the optimal filtration technique, we created several batches of nanodroplets made from the same lipid shell stock through the spontaneous nucleation method. These solutions were then either passed through a 450 nm mesh filter, centrifugated, or left undisturbed. The size and concentration of these nanodroplet solutions were measured the

same day as the ultrasound experiments, which was typically ~24 hr after fabrication. These were the four conditions we tested:

Control – no changes to nanodroplet solution after resuspending in PBS.

Size-Exclusion Centrifugation – the nanodroplet solution was spun down at 300 rcf for 5 minutes to allow the large nanodroplets settle to the bottom of the tubes. The supernatant was recovered, and this process was repeated three times.

Gravity Filtration – a 450 nm mesh filter (Corning) was attached to a syringe. The nanodroplet solution was loaded into the syringe and allowed to pass through the filter via gravity.

Pressure Filtration – a 450 nm mesh filter was attached to a syringe, and after the nanodroplet solution was loaded, the syringe plunger was depressed slowly until the entire nanodroplet solution passed through the filter.

On the day of experiments (~24 hr post-fabrication), the concentration and size of the nanodroplets were measured using a NanoSight300 (Malvern Panalytical). The concentration for each PFCnD stock was noted and used to create appropriate dilution factors such that the same quantity of each type of PFCnDs was suspended in agarose gels. PFCnD solutions were stored at 4^{o}C until use.

4.2.2 Ultrasound imaging and calibration

All experiments took place in a water bath heated to 37^{o}C. Nanodroplets were suspended in a 1% agarose gel (MilliporeSigma) to a final concentration of $1x10^{8}$ nanodroplets/mL ($4.2x10^{-5}$ %v/v) and loaded into thin-walled plastic containers. A focused single-element transducer (H-101, Sonic Concepts Inc.) operating at its third harmonic

frequency of 3.5 MHz (determined by performing a parametric frequency sweep between 3 and 4 MHz) was aligned with the nanodroplet gel sample. The single-element transducer was connected to a function generator (Agilent E4422B) and amplified with an RF power amplifier (325 LA, E&I Ltd.). A coupling cone was placed on the single-element transducer to align the focus of the transducer to the nanodroplet sample. This single-element transducer set-up was used to initiate droplet vaporization in the nanodroplet sample. Orthogonal to the nanodroplet sample was a linear array transducer (L7-4v, Philips) operating at its center frequency of 5 MHz and transmitting plane waves at a frame rate of 3500 Hz, which captured B-mode images of the vaporized nanodroplets above the focal spot of the focused ultrasound transducer (**Fig. 4.2 a**). Data was acquired using a Research Ultrasound system (Vantage 256, Verasonics, Inc.) running a custom MATLAB script that synchronized the focused ultrasound pulse with the captured B-mode image. Thirty pre-activation B-mode image frames were collected as background signal, then the single-element transducer was triggered by the Vantage 256 to emit a 20-cycle burst sine wave at a specified pressure output to initiate ADV in the nanodroplet-loaded agarose gel, followed by 400 post-ADV B-mode frames. A 20-cycle burst was selected to keep the transmission duty cycle well below 10%. The 20-cycle burst was also selected to simultaneously phase-transition a high proportion of PFCnDs while preventing inertial cavitation, as longer bursts (20+ cycles) have greater chances of phase-transitioning more nanodroplets at lower insonation pressures while also risking inertial cavitation at lower pressures [108,112-114]. This activation and imaging sequence was repeated 20 times per pressure output, starting at the lowest pressure (2 MPa) output and gradually ramping the pressure amplitude from 2 to 9.5 MPa peak negative pressure (MI = 1 - 5). Data was stored

as both raw RF data (for IC detection) and B-mode image frames (for ADV analysis). The single-element transducer pressure output was calibrated prior to experiments using an HGL-0200 capsule hydrophone (ONDA Corp.), with RF data collected in LabVIEW 2019 (National Instruments) and analyzed in MATLAB 2020a (MathWorks). Voltage to pressure calibration of the single-element transducer was performed with the coupling cone and a thin (~1 mm) layer of 1% agarose gel in front of the transducer to simulate experimental conditions and account for any attenuation caused by the coupling cone and gel set-up.

4.2.3 Acoustic droplet vaporization characterization

Acoustic droplet vaporization (ADV) was quantified by measuring the mean echo power of the focal spot within the imaging window, as described by Fabiilli et al. and used in later applications [115]. The mean echo power (MEP) is calculated by summing the squared amplitude of all pixel intensities within an imaging window, then normalized by the window area as follows:

$$\boldsymbol{MEP(m)} = \frac{\mathbf{1}}{\boldsymbol{MN}} \sum_{\boldsymbol{i=1}}^{\boldsymbol{M}} \sum_{\boldsymbol{j=1}}^{\boldsymbol{N}} \boldsymbol{A_{i,j}^2} \quad \textbf{(1)}$$

where m is the frame number with dimensions M, N and A is the amplitude at pixel i, j. The MEP of ultrasound frames just after insonation (**Fig. 4.2 c**) will be significantly higher than frames preceding the activation event (**Fig. 4.2 b**) if the activating ultrasound sequence was powerful enough to induce ADV. The MEP would also significantly decrease post-insonation after a short period if PFCnDs either recondensed or dissolved into the surrounding scaffold (**Fig. 4.2 d**). We calculated the average MEP of 20 post-activation frames, ignoring the two frames immediately after the activating ultrasound sequence to

prevent signal from the focused ultrasound transducer from interfering with our calculations.

The MEP calculations were used to analyze the duration and intensity of vaporized nanodroplets. MEP duration was characterized as the number of post-activation frames where the MEP was elevated above a threshold value, $20\times MEP_{Avg,\ Pre\text{-}Activation}$, where $MEP_{Avg,\ Pre\text{-}Activation}$ is the average MEP value of the 30 pre-activation frames before the vaporization pulse is triggered. This threshold was determined by measuring the average and standard deviation of the pre-activation frames and selecting a multiplier that would ensure the MEP signal measured in the post-activation frames was caused by phase transitioning PFCnDs and not background noise. Usually, the MEP of B-mode images of ADV was several orders of magnitude higher than frames containing no ADV, so increasing or decreasing the multiplier for the threshold value slightly (e.g., ± 5) does not significantly affect the measurement. MEP intensity comparisons between different groups of PFCnDs were made by determining the maximum MEP induced by the activation pulse per activation and imaging sequence.

4.2.4 Inertial cavitation characterization

Inertial cavitation was determined by analyzing the RF data received by the imaging transducer immediately after the phase-transitioning ultrasound pulse. The RF data collected by the four elements of the linear array transducer located directly above the focal spot of the single-element transducer was analyzed by taking the fast Fourier transform and analyzing the signal amplitude between 4 and 6 MHz. This frequency window was selected because it did not contain any of the 2^{nd} harmonic signal coming from

the nanodroplets caused by the single-element transducer (~7 MHz) and could be used as a region to characterize the noise floor. Since inertial cavitation is typically measured by broadband acoustic emission, we could use this frequency region to gauge if there was an elevated noise floor after the activation ultrasound pulse. Transducer elements were specifically selected to be located above the focus spot of the activation pulse, as determined by analyzing the B-mode image data. The signal from the lowest activation pulse pressure was used as the noise floor baseline measurement. A threshold was empirically selected in a similar manner as used in Fabiilli et al. in order to distinguish an IC event from background noise caused by the insonating focused ultrasound transducer [115]. The threshold for IC detection was set as

$$\boldsymbol{NF_{\text{sample}} > NF_{\text{base}} + 3 * \delta_{NF_{\text{base}}}}, \quad \textbf{(2)}$$

where NF_{sample} is the noise floor of the sample of interest (**Fig. 4.2 e, red line**), NF_{base} is the noise floor of the PFCnD sample at the lowest insonation pressure (2 MPa peak negative pressure) and $\delta_{NF_{\text{base}}}$ is the standard deviation of the noise floor at the lowest insonation pressure (**Fig. 4.2 e, black line**). The threshold for IC detection is quite low so that the IC analysis is very sensitive to any potential IC events in the nanodroplet samples.

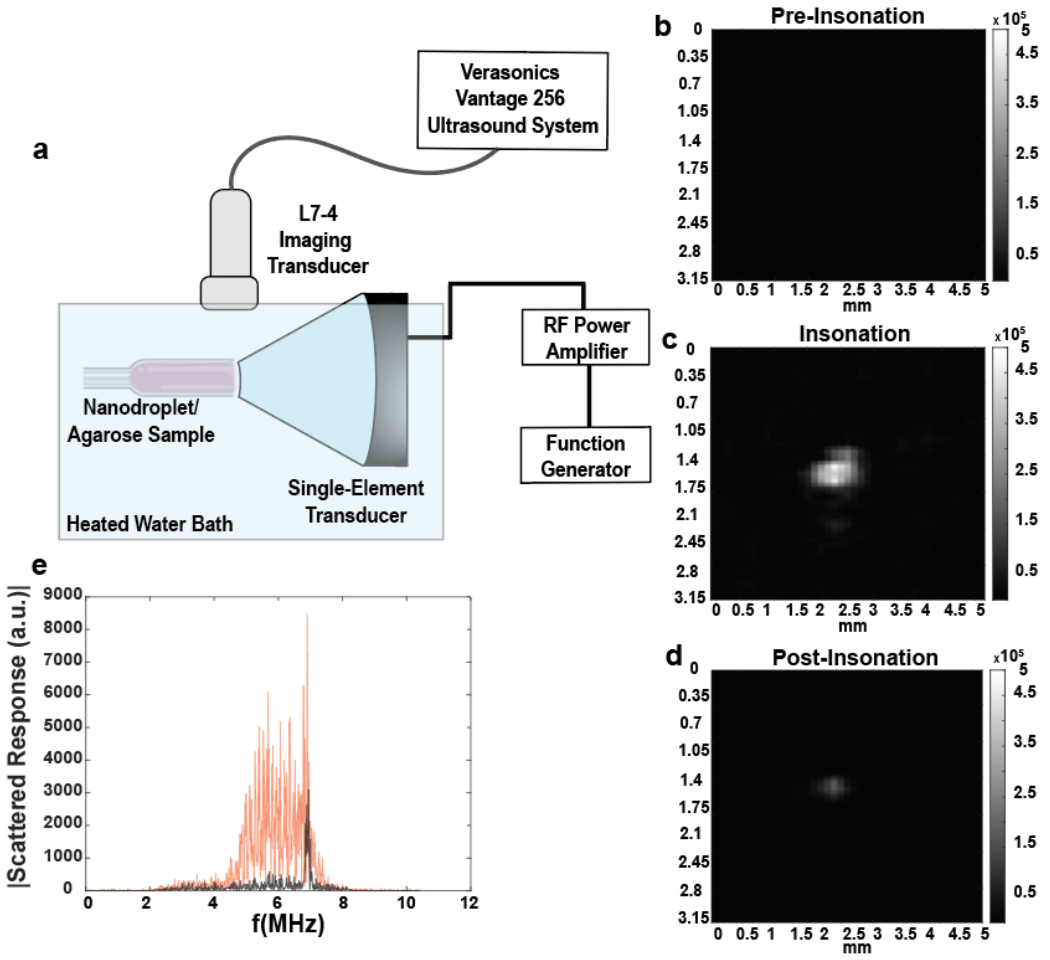

Figure 4.2: Methods used for B-mode image and RF data collection for acoustic droplet vaporization and inertial cavitation characterization. a. Overview of experimental set-up. **b., c., d.**, Representative B-mode images of perfluorocarbon nanodroplets phase-transitioning and recondensation/dissolution before, during, and after insonation, respectively. Nanodroplets used in these images are 50:50 lipid shelled, 50:50 PFP:PFH nanodroplets. **e.** Fourier transform of insonated PFCnDs at 2 MPa peak negative activation pressure (black line – no acoustic droplet vaporization nor inertial cavitation) and at 9 MPa peak negative activation pressure (red line – evidence of inertial cavitation).

4.2.5 Statistical analysis

ADV and IC data were plotted using MATLAB, and sigmoidal best-fit curves were fitted to the scatterplot data. The custom equation for the sigmoidal curve is $y = a + \frac{b-a}{1+(\frac{x}{c})^d}$, where x is the pressure value and y is either the cavitation probability or acoustic droplet

vaporization intensity, a and b are the maximum and minimum y-values, respectively, c is the x -value at the y -midpoint, and d is the slope at c [115]. These sigmoidal curves were used to determine the onset of ADV and IC. ADV onset was characterized by the appearance of ultrasound contrast immediately after the insonating pulse by the focused ultrasound transducer, caused by the phase transitioning of the PFCnDs. This appearance of ultrasound contrast correlates well with the x-value at the y-midpoint of the sigmoidal curve. IC onset is defined as the 50% crossing of the sigmoid fit on the cavitation curve [84]. Box plots and statistical analysis were conducted in R Studio. One-way ANOVA and Tukey's t-test were used to determine statistical significance in variances between different nanodroplet compositions.

4.3 Results and Discussion

4.3.1 Nanodroplet filtration

Nanodroplet composition impacts the size distribution of the resulting nanodroplets, which can significantly influence ADV and IC thresholds [116]. If there are large nanodroplets present in the nanodroplet suspension, ADV can be observed at relatively low pressures as nanodroplets with larger diameters require lower pressures to vaporize than those with smaller diameters due to superharmonic focusing [103,117,118]. To eliminate particularly large nanodroplets, centrifugation is commonly used to separate large, coalesced nanodroplets from the rest of the sample [119]. However, this size-exclusion technique has not been extensively compared to other separation methods such as mesh filtration. We sought to optimize a simple but effective nanodroplet filtration method to create nanodroplet solutions of uniform, monodisperse nanodroplets by passing our

nanodroplet suspensions through a 450 nm mesh filter. We selected 450 nm mesh filters for our filtration studies knowing that mesh filters are not perfectly monodisperse, and if we used filters with an average pore size closer to our initial average nanodroplet diameter (~220 nm) we would risk excluding a much higher proportion of nanodroplets and thus significantly reduce the quantity of nanodroplets in our solutions [120]. The control sample of nanodroplets, which did not undergo any size-exclusion separation technique, had the largest mean diameter and standard deviation in diameter distribution amongst the samples (**Fig. 4.3 a, c**). The gravity filtered and pressure filtered nanodroplets yielded the smallest average diameter without significantly reducing the concentration of the sample (**Fig. 4.3 b, c**). In order to eliminate the risk of including large (>450 nm) nanodroplets in our study, all nanodroplet samples were pressure filtered before used for ultrasound imaging in subsequent experiments.

Nanodroplets passed through a 450 nm mesh filter had significantly smaller diameters than non-filtered and centrifugated nanodroplets. At surface level these findings seem obvious, but in reality the results are somewhat surprising because it has been hypothesized that pushing lipid shelled PFCnDs through a mesh filter can cause some nanodroplets to break open and coalesce with nearby droplets [121]. This theory is still possible, though perhaps the large nanodroplets formed via coalescing are less stable than the smaller ones and either evaporate or coalesce and sediment within the 24 hr period between fabricating the PFCnDs and measuring their size and concentration. The more likely reason that mesh filtered PFCnDs tend to have smaller average diameters is because any nanodroplets greater than the mesh pore size (in this case, 450 nm) are excluded from size measurements and do not contribute to the diameter calculations by the NanoSight

300. The mesh filtered nanodroplets may have a slightly larger standard deviation compared to the centrifugated and control nanodroplets either because some nanodroplets are fractured by the filter and the lipid shell fragments form very small (< 100 nm) liposomes containing no perfluorocarbons, or some of the nanodroplets have excess lipid shell that are shed as they pass through the filter and form liposomes [122].

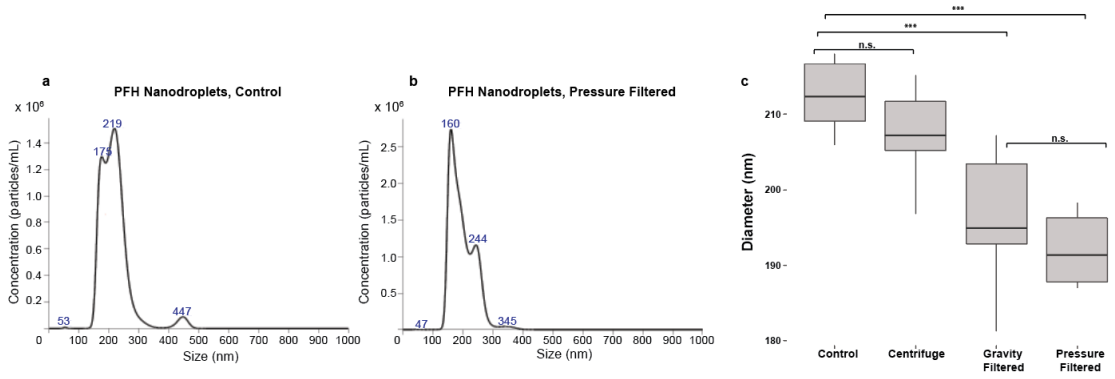

Figure 4.3: Size exclusion techniques on perfluorocarbon nanodroplet diameters. **a.** Size distribution of PFCnDs with a perfluorohexane core with no size separation technique applied. Average diameter of these droplets was 217.9 ± 52.2 nm, 10^{10} nanodroplets/mL. **b.** Size distribution of PFCnDs with a perfluorohexane core after passage through a syringe fitted with a 450 nm mesh filter. Average diameter of these droplets 197.5 ± 41.1 nm, 10^{10} nanodroplets/mL. **c.** PFCnDs passed through a 450 nm filter yielded nanodroplets with the smallest diameters, compared to centrifugation techniques and unmodified (control) nanodroplet samples. n = 6.

Next, we investigated how the lipid shell composition impacts nanodroplet size distribution. PFCnDs with a PFH core were passed through a 450 nm mesh filter attached to a 1 mL syringe with the plunger gently applied to eliminate larger nanodroplets. Based on three different batches of PFCnDs, nanodroplets with a 10:90 ratio of DPPC:DSPE-PEG_{2000} were significantly larger than 50:50 and 90:10 lipid shelled nanodroplets (**Fig 4.4 a**). There was no significant difference in size between the 50:50 and 90:10 lipid shelled

PFCnDs. No significant difference in nanodroplet diameter is observed when PFCnDs are grouped by core composition (**Fig 4.4 b**), indicating that the lipid shell, rather than core composition, influences nanodroplet size distributions.

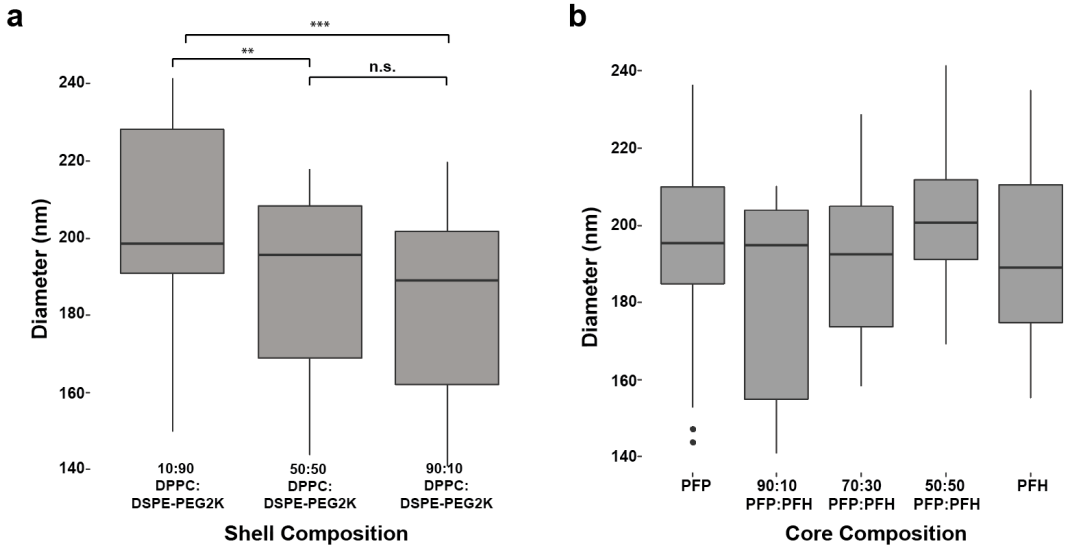

Figure 4.4: Perfluorocarbon nanodroplet size distribution vs. lipid shell composition. a. 10:90 lipid shelled PFCnDs had notably larger nanodroplets across all experiments and core compositions (n = 27). **b.** Grouping nanodroplets with different lipid shell compositions together based on perfluorocarbon core, no significant difference in diameter was observed amongst PFCnDs with different core compositions, indicating changes in PFCnD sizes are linked to shell composition. (n = 9).

4.3.2 Acoustic droplet vaporization intensity vs. shell composition

Ultrasound B-mode image intensity caused by the phase transitioning of the PFCnDs is critical for medical imaging applications, as PFCnDs that produce a stronger acoustic signal are easier to locate *in vivo*. The intensity of the resulting image contrast produced after ADV was quantified by calculating the MEP in the focal region (**Fig. 4.5**

a). Once the insonating pressure from the single-element transducer reached a certain threshold, a noticeable bubble cloud would appear in the transducer's focal region. As the transducer increased above this pressure, the bubble cloud intensity increased, indicating a greater proportion of nanodroplets were phase-transitioned in the focal region and yielding a higher MEP. This trend continued until the insonating pressure reached 7-7.5 MPa peak negative pressure (PNP) (MI = 3.75-4), at which point the maximum number of PFCnDs were phase-transitioned during each insonating pulse. Analyzed across three experimental periods with separate batches of nanodroplets, the 50:50 lipid shelled PFCnDs exhibited significantly stronger ADV intensities than the 10:90 and 90:10 lipid shelled nanodroplets (**Fig. 4.5 b**). The 90:10 and 10:90 non-PEGylated:PEGylated PFCnDs had comparable MEP values.

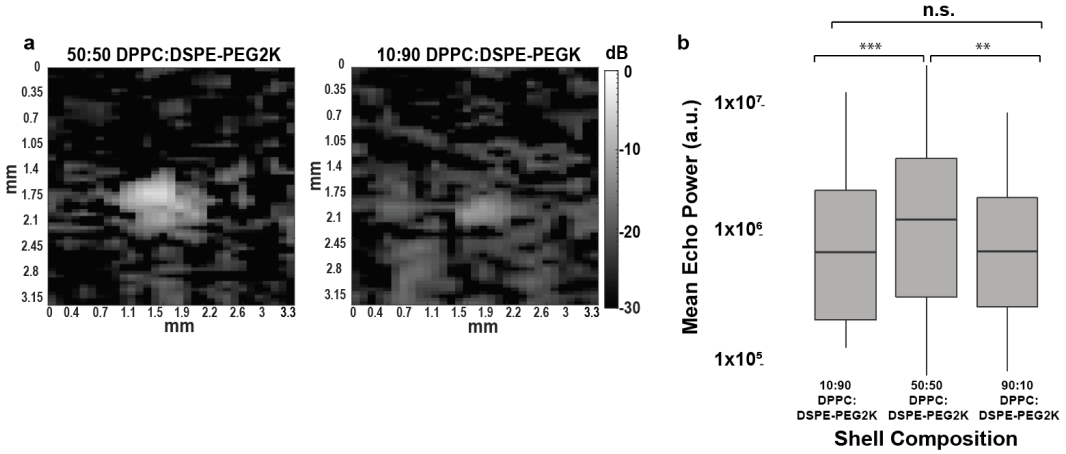

Figure 4.5: Comparison of lipid shell PFCnD B-mode image intensity. a. B-mode images of 50:50 lipid shell and 10:90 lipid shell PFCnDs after insonation at the same peak negative pressure (9 MPa). **b.** PFCnDs with a 50:50 lipid shell consistently exhibited greater ultrasound contrast across all core compositions and nanodroplet batches.

These insonating pressures exceed the recommended pressures used in medical ultrasound and are required in this study due to the agarose hydrogel environment whose matrix suppresses some nanodroplet expansion (as opposed to an all-liquid environment more commonly used in nanodroplet studies). The ADV threshold can be easily modified by changing the core composition to contain lower boiling point perfluorocarbons such as PFB and increasing the number of cycles per insonating pulse.

The cause for increased B-mode intensity in nanodroplets with a 50:50 lipid shell ratio of non-PEGylated:PEGylated lipids could be caused by several factors. It is possible that these 50:50 nanodroplets have improved vaporization efficiency than other nanodroplet compositions, so a larger proportion of nanodroplets expand with each insonating pulse. The cause of this improved vaporization efficiency may be due to the packing structure and distribution of the two phospholipids in the nanodroplet shell. In one study of multi-component phospholipid micelles by Viitala et al. (2019) the authors noted that increasing the ratio of DSPE-PEG2000 in the DPPC:DSPE-PEG2000 liposomes from ~10% DSPE-PEG2000 to 50% DSPE-PEG2000 caused a shape change from bicelles to slightly elongated micelles [123]. DPPC:DSPE-PEG2000 lipid shelled nanodroplets have small domains of only DPPC or DSPE-PEG2000, creating a solid-liquid ordered phase coexistence, as detailed in Chattaraj et al. (2016) [110]. The authors also noted that increasing the PEG concentration in these droplets from 3% mol to 20% mol caused a significant increase in acoustic signal, likely because PEGylated lipids are typically included in lipid-shelled nanodroplets for increased steric stabilization and perhaps because this lipid shell organization, with distinct regions of DPPC and DSPE-PEG2000, causes nanodroplets to phase-transition well without inertial cavitation nor dissolution into the surrounding

medium. Our results agree with Chattaraj et al. in that increasing the ratio of PEGylated lipids from 10% mol to 50% mol yielded a significantly stronger acoustic response post-ultrasound insonation. However, the addition of too much PEGylated lipid could create steric hindrance issues and/or create too stiff of lipid shells for efficient nanodroplet expansion, hence why our 10:90 DPPC:DSPE-PEG2000 nanodroplets had lower acoustic signal overall.

Another potential cause of stronger acoustic intensity is that the 50:50 lipid shelled nanodroplets yield larger gaseous microbubbles after insonation compared to the other two compositions. PFCnDs will typically yield microbubbles that are 3-5 times larger in diameter than their liquid, condensed form, with smaller nanodroplets forming proportionally smaller microbubbles due to increased Laplace pressure [85]. The interfacial tension differences between the lipid shell and perfluorocarbon core may impact the Laplace pressure and shell stiffness, which could affect ADV conversion efficiency and the responsiveness of the resulting bubbles for the lipid shelled PFCnDs. Thus, the 50:50 lipid shelled nanodroplets may stably expand to a larger microbubble diameter than the other compositions, or a greater proportion of the 50:50 lipid shelled nanodroplets expand with each insonating ultrasound pulse, providing greater ultrasound contrast. Confirmation of these theories would require an experimental set-up similar to that in Seda et al. (2015) in which PFCnDs were placed above a microscope objective and the resulting bubble clouds post-insonation were optically observed [124]. Further research on the ideal ratio of PEGylated to non-PEGylated lipids in perfluorocarbon nanodroplets must be conducted to determine the ideal shell ratio, but among the nanodroplet compositions used in this study,

50:50 lipid shelled PFCnDs would be the ideal ultrasound contrast agent to use in imaging applications where stark image contrast is required.

Although using nanodroplets with a higher PEGylated lipid ratio may yield improved ultrasound contrast, one area of concern is potential bioeffects caused by lipid shell composition. PEG is a common additive to a variety of nanomaterials used to increase *in vivo* stability [125,126]. Studies investigating the use of PFCnDs *in vivo* have used a variety of PEG ratios in lipid shells, even up to 90% PEGylated lipids, with no reported ill effect [104,127,128]. While using PFCnDs with various PEG ratios appears to be safe for one-time, short-term experiments, long-term and repeated administration of PFCnDs, especially those with higher PEG ratios, has not been thoroughly investigated and could potentially lead to nanodroplet build-up within certain organs, increased clearance from the circulatory system, and cytotoxicity. Researchers studying PEGylated liposomes for drug delivery have noted that repeated injections of PEGylated liposomes at certain concentrations leads to accelerated blood clearance after the first injection due to anti-PEG IgM-mediated activation [129-131]. Additionally, high PEG ratios can prevent nanoparticle uptake into cells, which may be an issue if the desired use of these PFCnDs is to use them for targeted intracellular uptake [132,133]. Researchers should consider these potential effects that may result *in vivo* when creating PFCnDs and design the lipid shell composition appropriately based on the desired application. Researchers should also use caution if utilizing these PFCnDs for long durations or repeated injections as there may be unknown cytotoxic effects or increased immune activation that result from repeated use.

4.3.3 Acoustic droplet vaporization duration vs. shell composition

The duration in which vaporized PFCnDs remained in their gaseous state was calculated by measuring the number of frames in which the MEP in ultrasound frames post-ADV was elevated above the threshold value $20\times MEP_{Avg,\ Pre\text{-}Activation}$. PFCnDs composed of a 10:90 DPPC:DSPE-PEG_{2000} lipid shell had the briefest duration in the gaseous state across all nanodroplet batches and core compositions (**Fig. 4.6 a**). There was no significant difference in ADV duration between the 50:50 and 90:10 lipid shelled PFCnDs. Post-insonation peaks in MEP were observed in the same nanodroplet samples after multiple insonation events, even in nanodroplets with boiling points below the environment temperature, suggesting nanodroplet recondensation (**Fig. 4.6 b**).

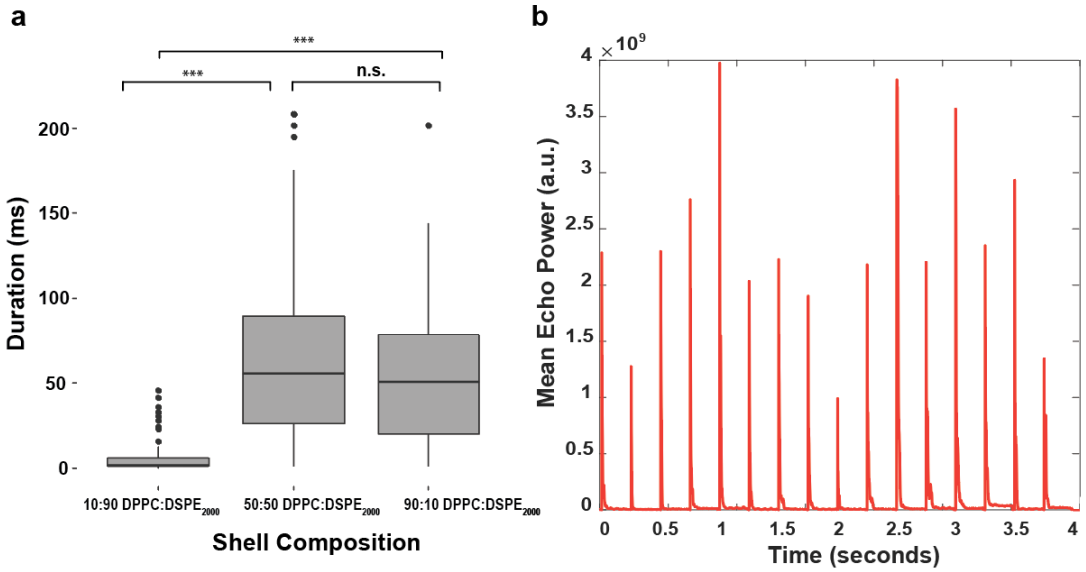

Figure 4.6: Representative duration data from one dataset depicting the differences in Mean Echo Power (MEP) across all nanodroplet types. a. 10:90 lipid shell nanodroplets exist as gaseous microbubbles for significantly shorter periods compared to both 90:10 and 50:50 lipid shell nanodroplets across all core compositions. **b.** MEP vs. time in PFP nanodroplets with a 50:50 non-PEGylated:PEGylated lipid shell, insonated at max operating pressure (9.5 MPa).

The cause of disappearing ultrasound signal after phase transitioning can be attributed to several factors. The perfluorocarbon core composition can significantly impact whether nanodroplets can recondense or dissolve into the surrounding environment. Nanodroplet recondensation has been observed in nanodroplets composed of both PFP and PFH cores [60,61,87,94,95], so it is possible that many of the nanodroplets within the PFCnD samples tested in these experiments are recondensing to a liquid state after insonation, as observed in **Figure 4.6 b**. The sustained signal intensity across all subsequent insonating pulses, even at very high pressures, supports this claim. Furthermore, the agarose matrix in which the PFCnDs are suspended can encourage recondensation rather than fragmentation, whereas in flow tube phantoms, there tends to be a loss in ultrasound signal as the liquid nanodroplet suspension is repeatedly subjected to high intensity ultrasound pulses [134]. Differences in interfacial properties of the lipid shelled PFCnDs could significantly impact the recondensation of the vaporized bubbles, with the 10:90 lipid shelled nanodroplets exhibiting the greatest interfacial forces and the 50:50 lipid shelled nanodroplets possessing weaker interfacial forces. The high proportion of PEGylated lipids in the 10:90 PFCnDs could also be the cause of rapidly disappearing acoustic signal as the PEG creates stiffer encapsulating shells, encouraging fracturing and/or rapid recondensation of the nanodroplets. Lastly, some PFCnDs, especially those composed of a core with a lower vaporization temperature threshold, may fragment post-phase transitioning due to being in an environment above the vaporization point of the core and possessing an unstable lipid shell, despite their suspension in agarose gel [135,136].

4.3.4 Pressure differential between acoustic droplet vaporization onset and inertial cavitation onset

We also investigated the onset of ADV and IC in all PFCnD samples. IC was characterized by a significant increase in the noise floor directly after insonation by the single-element transducer compared to the noise floor of the lowest insonation pressure used (2 MPa). From here, the pressure difference between ADV onset (insonation pressure at which nanodroplets begin to phase transition) and IC onset (characterized as 50% cavitation probability) was calculated across all samples. PFCnDs with a 50:50 lipid shell ratio had the largest pressure difference between when ADV was noticeable and when IC surpassed the vaporization threshold compared to 10:90 and 90:10 lipid shelled nanodroplets, as exhibited by the representative plots in **Figure 4.7** (**Fig. 4.7 a, b, c**). This trend was observed across all nanodroplet samples of various sizes and core composition, and the pressure differential was considerably larger in nanodroplets with smaller diameters (150-180 nm vs. 200-250 nm, **Fig. 4.7 d**).

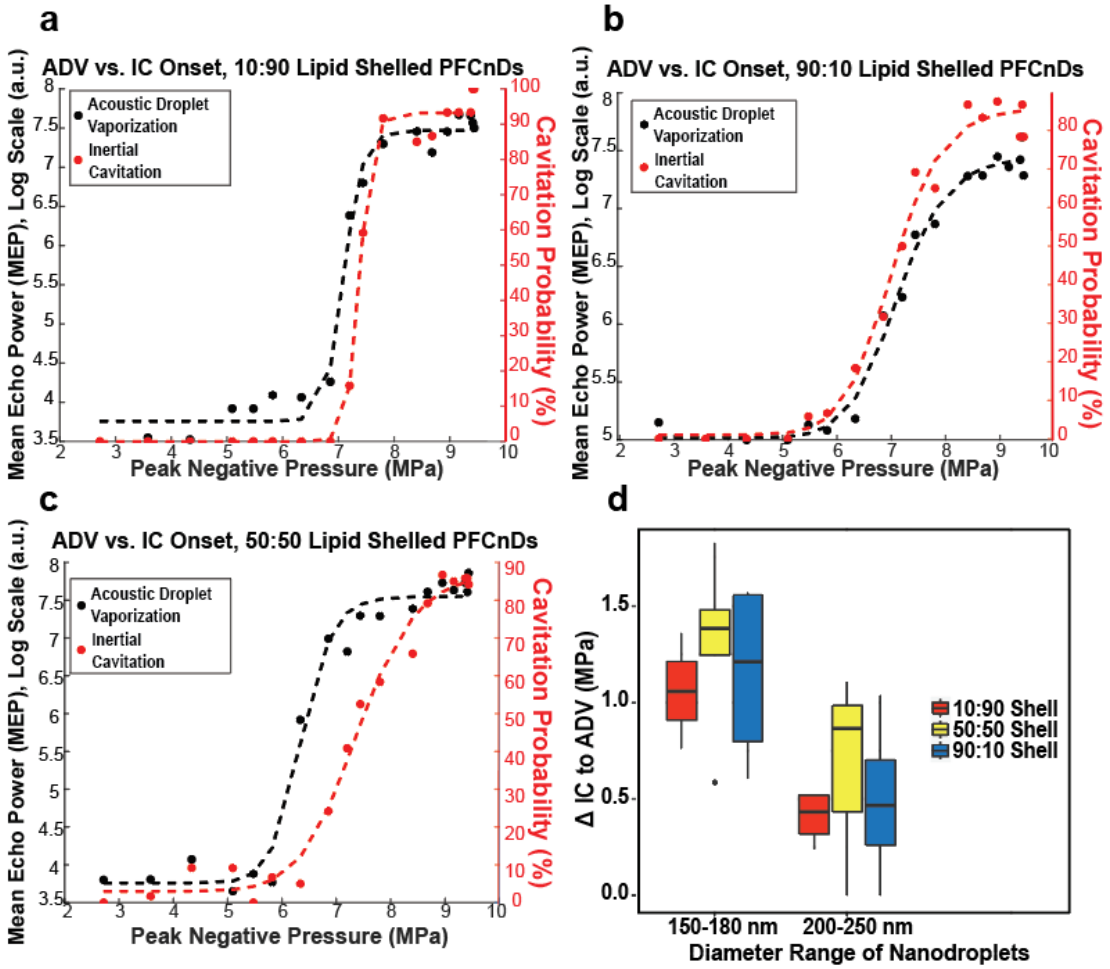

Figure 4.7: ADV and IC onset of PFCnDs is influenced by their lipid shell composition. a., b., c., Onset of ADV and IC for 10:90, 50:50, and 90:10 lipid shell PFCnDs with a 50:50 PFP:PFH perfluorocarbon core, respectively. These data are representative of all data sets collected. **d.** The differential between ADV onset and IC onset of various lipid shell compositions of all PFC cores. This pressure differential is influenced by both shell composition and nanodroplet sizes.

The differential between ADV and IC onset is an important metric for both imaging and therapeutic applications. For ultrasonic imaging of these contrast agents *in vivo*, IC can be detrimental to surrounding cells and tissues; inducing ADV without triggering IC, therefore, is critical. Creating PFCnDs with the lowest possible ADV threshold is crucial in diagnostic imaging to enable phase transitioning without using insonating pressures

above the Food and Drug Administration's MI threshold for *in vivo* applications. Contrary to this, damaging tissues and cells via IC can be the goal of using ultrasonically triggerable PFCnDs, so nanodroplets with a lower IC threshold are ideal, and the pressure difference between ADV onset and IC onset is negligible. Based on these considerations, 50:50 lipid shelled PFCnDs would be ideal contrast agents for theranostic applications; these droplets exhibited the greatest ADV to IC onset pressure differential and highest contrast to noise, and could thus facilitate both ultrasound imaging (ADV) and ultrasound-induced drug released or localized tissue ablation (IC). However, the perfluorocarbon cores used in this paper yielded PFCnDs with ADV thresholds above the FDA's MI limit. Changing the perfluorocarbon core to include perfluorocarbons with lower vaporization temperatures (e.g., perfluorobutane) can bring the ADV threshold to biologically safe pressures.

It is important to consider that the window between ADV and IC is quite narrow, even for the 50:50 lipid shelled PFCnDs. This narrow pressure differential has been observed in other works and has implications for utilizing PFCnDs safely for *in vivo* applications. [108]. Our findings demonstrate that the ADV to IC pressure differential is larger for PFCnDs with smaller diameters, but one problem with small nanodroplets (diameters < 200 nm) is that they require very high insonation pressures exceeding MI limits compared to larger nanodroplets. Researchers have developed ways to lower and control both ADV and IC thresholds by using unique transducer configurations or ultrasound standing waves, but future work should investigate whether these techniques can be used to create a greater ADV to IC differential, whether these techniques can be used to insonate and phase transition nanodroplets with sub-200 nm diameters, and whether these techniques are applicable *in vivo* [137,138].

It is important to note that all experiments in this paper were conducted in tissue-mimicking phantoms within a temperature-controlled water bath. We opted to conduct experiments in this well-controlled environment, rather than *in vivo*, so that any differences in acoustic behavior were attributed to the PFCnDs instead of slight changes to the experimental set-up (e.g., differences between animals, changes in tissue stiffness, etc.). Future work should include testing these PFCnDs with different lipid shell compositions *in vivo* or in environments that better represent *in vivo* conditions, such as excised tissue, to validate that these differences in nanodroplet behavior are still exhibited *in vivo*. Additionally, as mentioned in Section IIIB, special care should be taken if using these PFCnDs for long-term studies with repeated injections in order to understand potential bioeffects caused by the presence of these nanodroplets *in vivo*.

4.4 Conclusion

We investigated the influences of the lipid shell composition on the size distribution, ultrasound characteristics, and vaporization dynamics of perfluorocarbon nanodroplets. Our results suggest that passing nanodroplets through a mesh filter yields nanodroplet suspensions with smaller average diameters by excluding large (450+ nm diameter) nanodroplets. Furthermore, lipid shell PFCnDs with a high proportion of PEG-ylated lipids have larger diameters, though the size distribution of nanodroplets may be more dependent on fabrication method than lipid shell composition. PFCnDs with a 50:50 DPPC:DSPE-PEG_{2000} lipid shell composition created the strongest ultrasound contrast, had the longest duration in the phase-transitioned state, and had the greatest pressure difference between ADV onset and IC onset among all nanodroplet samples used in this study. Based

on these results, the 50:50 lipid shelled PFCnDs are ideal candidates for theranostic applications and ultrasound imaging in general due to their monodispersity, high contrast to noise ratio, and large ADV to IC pressure differential. 90:10 and 10:90 lipid shelled PFCnDs are both excellent candidates for tissue ablation and localized drug delivery. Altering the perfluorocarbon core can influence the duration in which the PFCnD remains gaseous as well as the vaporization threshold of the nanodroplets. The findings in this work can help guide researchers to fabricate PFCnDs with the desired ultrasonic properties for a variety of applications.

Chapter 5

NANODROPLET INJECTION INTO CELLS USING PATCH CLAMP FOR SUBSEQUENT ULTRASOUND IMAGING

5.1 Introduction

Perfluorocarbon nanodroplets (PFCnDs) are a condensed form of microbubbles with a liquid perfluorocarbon core, rather than a gas core, surrounded by lipids, proteins, surfactants, or polymers, and range in size from 100-500 nm in diameter. Because of their liquid interior and smaller size, PFCnDs have improved *in vivo* stability compared to gas microbubbles, lasting hours to days *in vivo* or *in vivo*-mimicking conditions and are small enough to enter spaces that microbubbles cannot [55,61,99,139]. Active areas of research involving PFCnDs include targeted chemotherapeutic drug delivery to tumors [55]. Tumors excrete substantial angiogenic factors that encourage rapid development of immature blood vessels with large endothelial gaps, and PFCnDs are well positioned to extravasate through these large pores in the blood vessels and reside in tumor tissue. Tumors have poor clearance from lymphatic dysfunction as well, so the PFCnDs can remain in the tissue for over 24 hours post-injection [127,140]. Upon ultrasound insonation, the nanodroplets can undergo inertial cavitation to release the drug contained within its core. PFCnDs are also a useful agent for histotripsy applications and are safer than microbubbles due to a reduced chance of off-target cavitation in the tissue.

Besides various tissue therapies, PFCnDs have been used for super-resolution ultrasound imaging applications. PFCnDs behave in an acoustically analogous manner to the fluorophores used in photoactivated localization microscopy (PALM) and stochastic optical reconstruction microscopy (STORM), two super-resolution optical imaging

techniques [57,58]. In PALM and STORM, sparse subsets of fluorophores are stochastically excited to fluoresce. These fluorophores are imaged and allowed to photobleach to eliminate their signal. The process is repeated, then the precise locations of each fluorophore are super-resolved by locating the peak of each point spread function created by the fluorophore. Finally, these fluorophore locations are projected onto one plane to form a pointillism reconstructed image of the structure of interest. PFCnDs are capable of stochastic activation through short pulses of focused ultrasound and can recondense back to liquid nanodroplets from gas microbubbles under certain conditions, similar to the way that the fluorophores in PALM/STORM photobleach. Already, PFCnDs have been used to achieve micrometer-scale image resolution in tissue, and one theoretical analysis has proposed that PFCnDs could be used to achieve sub-micron resolution if a transducer with sufficiently high frequency was used (> 18 MHz) in conjunction with ultrafast ultrasound localization microscopy (uULM) [59-61]. Gas microbubbles have been used with ULM to reconstruct blood vessel structures in a mouse brain by tracking the changing microbubble positions within vessels to form the super-resolved images [25]. However, because gas microbubbles do not exhibit the phase change behavior of PFCnDs, in addition to their size and stability limitations, gas microbubbles can only be used to form super-resolution images of body structures with fluid movement; gas microbubbles cannot be used for super-resolution imaging of cells or tissue.

Because of their smaller size, improved stability, and super-resolution capabilities, PFCnDs are uniquely positioned to be used for intracellular imaging. However, their use as intracellular ultrasound contrast agents is extremely limited. Instead, gas vesicles and gas nanobubbles, which are like microbubbles except with nanometer-scale diameters

rather than micrometer-scale diameters, are two ultrasound contrast agents that are being actively used for intracellular ultrasound imaging [41,44,141,142]. Gas vesicles can be grown in mammalian cells by stably transfecting the cells with mammalian acoustic reporter genes (mARGs) as described in Chapter 3 of this thesis. These gas vesicles provide a noticeable ultrasound contrast caused by ultrasound-induced gas vesicle collapse. The cells can regenerate gas vesicles after several days, enabling repeatable, long-term ultrasound imaging. However, gas vesicles do not produce particularly strong ultrasound contrast and require significant concentrations of gas vesicles (and thus cells) to be present to produce any sort of image contrast [41]. Gas nanobubbles can have functionalized shells such that, when they extravasate through leaky vasculature into surrounding tumors, can be directly uptaken by cells for ultrasound imaging or drug delivery applications. However, gas nanobubbles suffer from similar limitations as gas microbubbles in terms of *in vivo* stability.

At the time of writing, there is very limited documented work of cell imaging using PFCnDs localized within cells. One problem is that it is challenging to get PFCnDs into most cell types. The one study of note that investigated PFCnDs for ultrasound imaging of cells used macrophages, which tend to engulf any foreign objects they come across [143]. For most other cells, the surfaces of the PFCnDs must be modified to contain a ligand or other molecule that encourages cell-specific uptake. However, with this technique, cell uptake appears to be limited and localized to only one or two regions of each cell (**Fig. 5.1**) [86]. If PFCnDs were to be used for more than cell localization, such as to image the morphology of a cell using super-resolution imaging techniques like ULM, the nanodroplets would need to span throughout the entire cell.

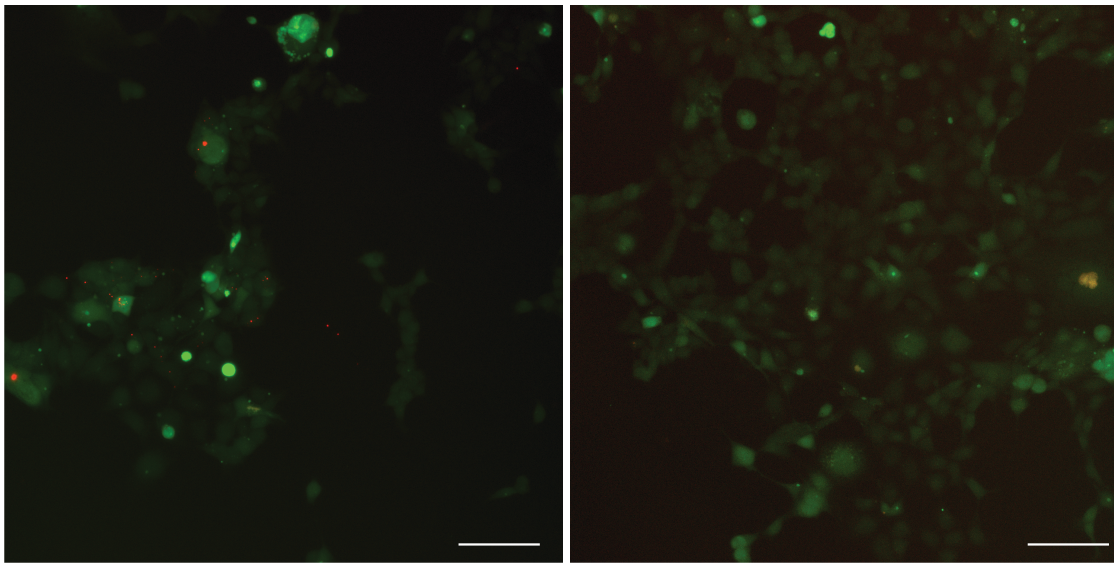

Figure 5.1. Polydopamine-treated perfluorocarbon nanodroplet uptake by HEK293T cells. Polydopamine-coated perfluorocarbon nanodroplets are sparsely uptaken into cells as evidenced by red puncta in cells stained with CellTracker Green (left) and no cellular uptake is seen using nanodroplets without polydopamine coating (right). Scale bar = 100 μm.

To enable delivery of PFCnDs into specific cells that encourages nanodroplet spreading throughout the entire cell body, a single-cell delivery mechanism must be used. The technique we propose to use for single cell nanodroplet injection is patch clamp, a precision neuroscience technique that is often used to deliver small molecules into cells for fluorescent labeling and subsequent imaging. However, patch clamp is rarely used to deliver objects larger than 40 nm in size [144]. As a result, it was first important to demonstrate the feasibility of patch clamp microinjection of PFCnDs. Furthermore, it was crucial to determine whether cells could be microinjected with PFCnDs via patch clamp in a manner where the cells could later be ultrasonically imaged.

Here, we explore the metrics of successful patch clamp microinjection of perfluorocarbon nanodroplets into HEK293T cells for subsequent single-cell ultrasound localization. Fluorescently tagged nanodroplets were prepared in a sterile environment and suspended in patch pipette internal solution. A pressure control system enabled injection of perfluorocarbon nanodroplets into HEK293T cells that were cultured on glass and PDMS coverslips. We recorded the gigaseal and break-in success rate of each patch attempt as well as the positive pressure applied to the tip of the micropipette required to drive nanodroplets into the cell. We also noted the distribution of nanodroplets once inside of the cell, which is useful to dictate whether this technique can be used for super-resolution imaging of the cell using ultrasound localization microscopy. We also describe methods for seamlessly transitioning nanodroplet-injected HEK293T cells from the patch clamp rig to an ultrasound imaging system for subsequent ultrasound localization. We share some results of localized HEK293T cells on the coverslip after patch clamp injection with PFCnDs. This work is the first of its kind to demonstrate nanodroplet injection via patch clamp into cultured HEK293T cells and ultrasound localization of those specific cells, paving the way for future studies involving single-cell imaging *in vitro* and *in vivo* over multi-day time periods, with the potential for super-resolution cellular imaging applications.

5.2 Materials and Methods

5.2.1 HEK293T Cell Culture on Glass Coverslips

For initial patch clamp experiments to examine feasibility and patch clamp parameters necessary for nanodroplet injection, HEK293T cells were seeded on sterilized

glass coverslips coated in poly-D-lysine. Glass coverslips were sterilized by soaking in 70% ethanol for 1 hour. Coverslips were rinsed 2x with PBS and allowed to air dry for 10 minutes in a biological safety cabinet. Then, the coverslips were coated in poly-D-lysine diluted in PBS in a 1:10 v/v ratio for at least 1 hour. The poly-D-lysine solution was aspirated and the coverslips were allowed to air dry in the biological safety cabinet before seeding with cells. HEK293T cells (ThermoFisher) between passages 4-25 grown in T-25 flasks were trypsinized (ThermoFisher), resuspended in DMEM supplemented with 10% FBS (ThermoFisher) and 1% penicillin/streptomycin before seeding on the sterilized coverslips at a density of 5,000-10,000 cells per coverslip.

5.2.2 PDMS coverslip preparation

For ultrasound imaging experiments, cells had to be grown on PDMS coverslips, a soft polymer, rather than glass to avoid acoustic shadowing and substantial noise in the resulting images. Sylgard 184 silicone elastomer kit (Dow Inc.) was mixed thoroughly in a 10:1 w/w ratio of base to curing agent and degassed in a vacuum chamber until no visible bubbles remained. Then, 2 g of the solution was poured into a 100 mm x 15 mm petri dish, spread evenly across the surface, and cured in a 45^{o}C oven for 1 hr. A 4.5 mm biopsy punch cut the PDMS into small, thin disks that were sterilized by soaking each side of the disks in 70% ethanol for 30 minutes. Afterward, the ethanol was aspirated and the PDMS coverslips were rinsed with sterile deionized water, then exposed to UV light for 1 hr.

Prior to culturing HEK293T cells on the PDMS coverslips, a 1 mm biopsy punch was used to form a small hole in each coverslip, which served as an alignment marker for subsequent ultrasound imaging and helped position the focal point of the single-element

transducer (the transducer responsible for inducing PFCnD phase transitioning to gaseous microbubbles). Then, the coverslips were soaked in 20% poly-D-lysine diluted with PBS and incubated in a 37°C cell culture incubator for a minimum of 1 hr and up to 24 hr. After incubating, the poly-D-lysine was aspirated and the coverslips were allowed to air dry in a biological safety cabinet for several minutes.

5.2.3 HEK293T Cell Culture onto PDMS Coverslips

HEK293T cells (ThermoFisher) between passages 4-25 were first grown in T-25 tissue culture flasks until 70-100% confluent. These adherent cells were cultured in DMEM supplemented with 10% FBS and 1% penicillin/streptomycin. The cells were trypsinized and suspended in DMEM before seeding on the PDMS coverslips at a density of 5,000-10,000 cells per coverslip. Cells were allowed to acclimate to the coverslips for at least 24 hours before beginning patch clamp experiments.

5.2.4 Perfluorocarbon nanodroplet fabrication via spontaneous nucleation

All nanodroplet fabrication experiments were conducted in a biological safety cabinet and made using sterile materials. Perfluorocarbon nanodroplets were created using a spontaneous nucleation method as described in Li et al. and Welch et al [83,84]. Briefly, 1,2-dipalmitoyl-sn-glycero-3-phosphocholine (DPPC) and N-(carbonyl-methoxypolyethylyeneglycol 2000)-1,2-distearoyl-sn-glycero-3-phosphoethanolamine (DSPE-PEG_{2000}) (NOF America Corporation) were dissolved in 190 proof ethanol in a 1:1 molar ratio (1:1 DPPC:DSPE-PEG_{2000}). The final concentration of lipids in these solutions was 2 μM. An aliquot of this lipid stock solution was added to a 1.5 mL microfuge tube

along with 50 µL of 2% DiI lipophilic tracer dye dissolved in ethanol, 45 µL of perfluoropentane (PFP) and 5 µL of perfluorohexane (PFH). The solution was vortex mixed for 10 seconds, then set out at room temperature for 15 minutes to allow excess perfluorocarbon to settle out of solution. 200 µL of this lipid/perfluorocarbon/DiI solution was mixed with 400 µL of lipid stock. Then, 3.4 µL of 7:2:1 water:propylene glycol:glycerol was added to the lipid solution. The sudden addition of this hydrophilic solution to the hydrophobic lipids caused the lipids to rapidly form micelles, encapsulating some perfluorocarbons in the process, in a reaction called spontaneous nucleation. These nanodroplets were centrifuged at 4500 rcf for 100 min, the supernatant discarded, resuspended in DI water, and the process was repeated three times. Prior to the last centrifugation, the nanodroplets were passed through a 450 nm mesh filter to eliminate any large droplets that formed during the nucleation process, then the nanodroplets were resuspended in patch clamp internal solution composed of (in mM): 100 K-gluconate, 30 KCl, 10 HEPES, 2 MgSO4, 0.5 EGTA, 3 ATP.

5.2.5 Nanodroplet Injection via Patch Clamp

Patch clamp nanodroplet injection experiments took place on a Scientifica patch clamp rig paired with an upright microscope with a 63x water immersion DIC objective, a DiI-spectrum filter cube, 3-axis micromanipulator connected to a pressure control box for positioning the patch pipette and controlling the pressure applied to the pipette, and a custom-built coverslip holder with perfusion inlet/outlet (**Fig. 5.2 a**). The pressure applied to the patch pipette was controlled using a LabVIEW program, where the pressure could be modulated in 5 mBar increments between -500 to +500 mBar. Borosilicate glass

capillaries with filaments, measuring 10 cm in length and 1 mm in diameter, were pulled in a P-1000 micropipette puller (Sutter Instruments) to produce 5 cm-long patch pipettes with an approximately 1 μm tip diameter and yielding 4-7 MΩ resistance. Coverslips covered with HEK293T cells were placed under the patch clamp rig microscope objective with constant perfusion of extracellular solution. Extracellular solution was composed of (in mM): 125 NaCl, 3 KCl, 10 HEPES, 5 glucose, 1 $MgCl_2$, 1.5 $CaCl_2$. The microscope objective of the patch clamp rig was focused in the z-direction such that HEK293T cells were on the focal plane of the microscope objective. Once a cell was selected for PFCnD injection, the microscope objective was moved several mm above the coverslip so that the patch pipette could be positioned between the microscope objective and the coverslip without damaging the patch pipette or the coverslip. Once the patch pipette tip was in focus under the microscope, 10-20 mBar positive pressure was applied to observe whether PFCnDs were expelled from the patch pipette. This helped to ensure that the patch pipette was not clogged and that nanodroplets were close to the tip of the pipette such that, once the patch pipette tip was connected to the cell via gigaseal and break-in, PFCnDs could be immediately injected into the cell. 5-10 mBar positive pressure was continuously applied as the patch pipette was lowered to the surface of the coverslip. Once the pipette tip touched the surface of the cell membrane, indicated by a +1 MΩ resistance at the pipette tip and by visual observation of cell dimpling, the positive pressure was switched off and a -5 mBar pressure was applied to create gentle suction between the pipette tip and the cell membrane until the resistance between the patch pipette and the cell membrane exceeded 1 GΩ, known as a gigaseal. Once a gigaseal was achieved, brief but strong suction was applied to the patch pipette tip to achieve break-in, or rupturing of the cell membrane such that the

internal pipette solution could interact with the intracellular components. If successful break-in was achieved, 1-second bursts of positive pressure were applied to the patch pipette, starting at 15 mBar, increasing in 5 mBar increments until noticeable fluid movement from the patch pipette into the cell occurred (**Fig. 5.2 b**). The objective was switched to a DiI filter cube to notice whether nanodroplets entered and spread throughout the cell. Images were captured before and after nanodroplet injection (**Fig. 5.2 c**). The pressure and duration required to drive PFCnDs into the cell were also noted. These patch experiments were video recorded using screen capture software (OBS Studio) for later analysis.

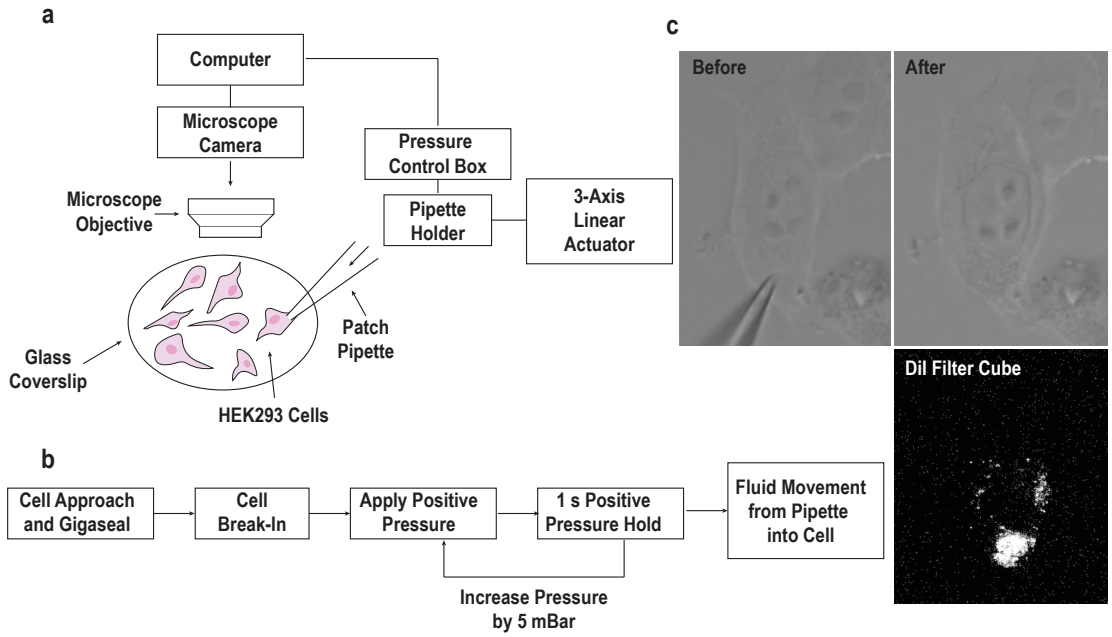

Figure 5.2: **Methods to achieve patch clamp nanodroplet injection into HEK293T cells on glass coverslips. a.** A block diagram of the equipment connected to the Scientifica patch clamp rig that facilitated perfluorocarbon nanodroplet microinjection, including a pressure control box and 3-axis linear actuator. **b.** Workflow diagram of each step during the patch clamp and microinjection process. **c.** Illustrative DIC images of a cell before and after nanodroplet microinjection and a fluorescent image of the cell containing PFCnDs, demonstrating successful transfer of PFCnDs from the patch pipette into the cell.

5.2.6 Cell preparation for ultrasound imaging

After cells on PDMS coverslips were microinjected with PFCnDs using patch clamp, the cells were fixed in 4% paraformaldehyde on a shaker plate at room temperature for 10 minutes, then rinsed in PBS before storing at 4^{o}C. These cells fixed on PDMS coverslips were optically imaged using a laser scanning microscope (LSM 900, Zeiss). The presence of cells injected with PFCnDs was confirmed via fluorescence microscopy and the morphology of the cell was captured using a brightfield + fluorescence image. Location of each cell near the coverslip alignment marker was noted to make cell localization during ultrasound imaging easier.

To ensure that paraformaldehyde fixation did not alter PFCnD phase change behavior under ultrasound insonation, PFCnDs were prepared as described in *5.2.4*, centrifuged at 4500 rcf for 100 minutes, and the resulting PFCnD pellet was resuspended in 4% paraformaldehyde for 30 minutes. Afterward, the PFCnDs were centrifuged again at 4500 rcf for 100 minutes, the supernatant was decanted and the PFCnDs were resuspended in PBS. These paraformaldehyde-treated PFCnDs were suspended in a 1% agarose gel at a concentration of 10^7 nanodroplets/mL, then loaded into a thin walled plastic sample holder. This sample was ultrasonically imaged as described in *5.2.7* (below) to verify that paraformaldehyde-treated PFCnDs still phase transitioned under ultrasound insonation to produce ultrasound contrast in B-mode images.

5.2.7 Ultrasound Imaging Set-Up

All ultrasound imaging experiments took place in a water bath heated to 37ºC. PDMS coverslips containing fixed and PFCnD-injected HEK293T cells were suspended in a 1% agarose gel (MilliporeSigma) and loaded into thin-walled plastic containers. A focused single-element transducer (H-101, Sonic Concepts Inc., Bothell, WA, USA) with a water-filled coupling cone attached, which helped to align the focus of the transducer to the coverslip, operated at 1.05 MHz. The single-element transducer was connected to a function generator (Agilent E4422B) and amplified with an RF power amplifier (325 LA, E&I Ltd.). This single-element transducer set-up was used to initiate nanodroplet vaporization in the cell on the PDMS coverslip. Orthogonal to the PDMS coverslip was a linear array transducer (L22-8v CMUT, Philips) operating at its center frequency of 15.625 MHz and transmitting plane waves at a frame rate of 330 Hz, which captured B-mode images of the vaporized nanodroplets at the focal spot of the focused ultrasound transducer. Data was acquired using a Research Ultrasound system (Vantage 256, Verasonics, Inc.) running a custom MATLAB script that synchronized the focused ultrasound pulse with the captured B-mode image. 10 pre-activation B-mode image frames were collected as background signal, then the single-element transducer was triggered by the Vantage 256 to emit a 20-cycle burst sine wave at a specified pressure output to initiate ADV in the nanodroplet-loaded cell, followed by 25 post-ADV B-mode frames. A 20-cycle burst was selected to keep the transmission duty cycle well below 10%. Data was stored as B-mode image frames for ADV analysis.

5.2.8 Data Analysis

Images were analyzed of the nanodroplet-injected cells to measure nanodroplet spread and distribution in the cell using a MATLAB script. DIC and fluorescence images of nanodroplet-injected HEK293T cells were captured on the patch clamp rig camera using ImageJ software. These images were uploaded into the MATLAB script and an outline of the cell was drawn around the cell of interest on the DIC image to create a mask. The mask of the cell was compared to the fluorescence image with the nanodroplets inside of the cell. These images were compared to roughly quantify the distribution of the nanodroplets throughout the cell by calculating the percentage of the cell area that the nanodroplets took up as well as the farthest recorded PFCnD from the injection site.

5.3 Results

5.3.1 Pressure and duration parameters for perfluorocarbon nanodroplet injection into HEK293T cells

In our first set of experiments, HEK293T cells cultured on glass coverslips were patch clamped and PFCnD injection was attempted. A total of 66 HEK293T cells were patched on glass coverslips for PFCnD injection validation. The gigaseal, break-in, and PFCnD injection success cases are listed in **Table 5.1**. 63 of these cells resulted in a successful gigaseal (pipette tip resistance > 1 GΩ) and 55 of these cells yielded a successful break-in (rupture of the cell membrane). 29 of the 66 attempted cells yielded successful PFCnD injection.

Table 5.1 Patch clamp attempts and successes at different stages of the patch clamp process. Out of 66 patch attempts, 63 gigaseals were achieved, 55 resulted in break-ins, and 29 yielded successful nanodroplet injection.

	Total patch attempts	Successful gigaseal	Successful break-in	Successful PFCnD injection
# cells	66	63	55	29
% of total attempts	100%	95.5%	87.3%	46.0%

Over 80% of the successfully injected HEK293T cells required pressures less than 100 mBar to drive the PFCnDs from the patch pipette into the cell (**Fig. 5.3 a, b**). However, occasionally a 100+ mBar pressure was required to drive nanodroplets into the cell. These higher pressures are necessary during instances when part of the cell membrane or intracellular components like organelles clogged the pipette tip. These clogs prevented PFCnDs from entering the cell unless substantial pressure was applied to drive both the nanodroplets and some of the cell debris back into the cell.

We also investigated the required duration for pressure to be held such that nanodroplets were inserted into the cell. Over half (15, 52%) of the cells only required 1 second of positive pressure to be applied in order to drive nanodroplets into the cell (**Fig. 5.3 c**). Essentially, there was some sort of minimum required pressure to overcome the pipette clog, and once that pressure was reached, the clog was removed and PFCnD flow from the pipette into the cell was rapid. The wide range of pressures used to insert nanodroplets into cells (15-165 mBar) indicates that there is significant heterogeneity between cells and the environment at the pipette tip after cell break-in. Future studies should be conducted to narrow this pressure window so it is more predictable for

researchers to know which pressures they should use when trying to drive PFCnDs, or other larger nanoparticles, into cells via patch clamp. Researchers should also note that exceeding pressures of 100 mBar increases the risk of cell rupture, as the pressure applied to the tip is too high and if the entire clog at the pipette tip is rapidly cleared, the flow out of the pipette at that pressure can be too immense and will cause cell damage.

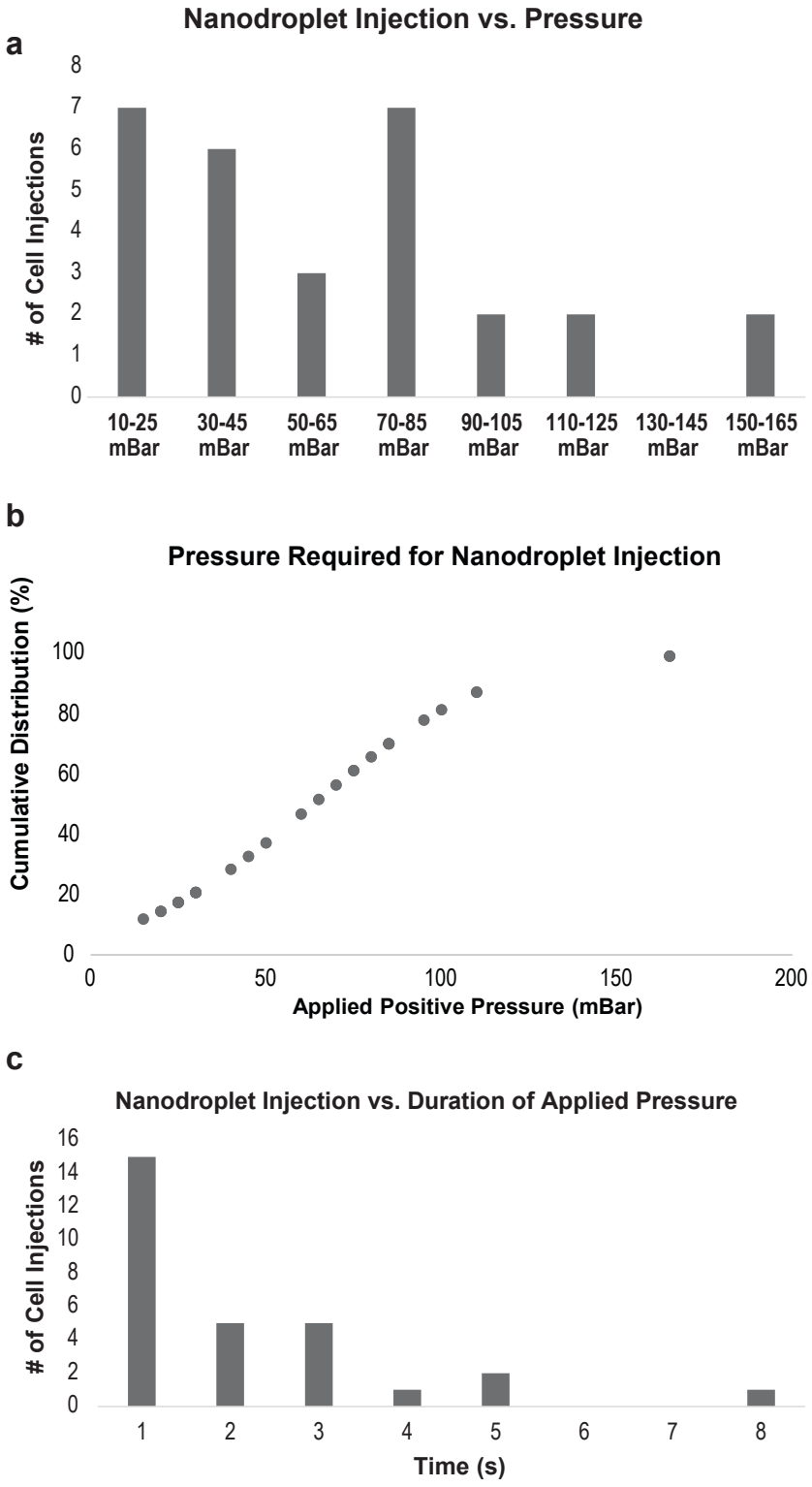

Figure 5.3. **Pressure and duration parameters yielding successful PFCnD injection via patch clamp into HEK293T cells. a.** Pressure vs. nanodroplet injection. **b.** Cumulative distribution function of pressure required to achieve nanodroplet injection. **c.** Duration vs. nanodroplet injection into HEK293T cells.

Out of the 55 successful cell break-ins, nanodroplets were injected in about 53% of those cells. There are several reasons why the success rate is not higher. Clogs at the pipette tip were the main issue resulting in no nanodroplet entry (35% of unsuccessful PFCnD injections). While the clogs were occasionally the result of excessive cell debris stuck at the pipette tip, the clogs were also caused by large nanodroplets at the tip preventing any other nanodroplets from entering the cell, even at pressures as high as 200 mBar. Clogging occurred more often when the PFCnD solution was filtered more than 12 hours prior to experiments. This is likely because nanodroplets slowly grow larger, even at refrigerated temperatures, due to Ostwald ripening, or gradual expansion of larger PFCnDs caused by molecular diffusion [145]. To keep the PFCnDs as small and monodisperse as possible, it is crucial to filter the nanodroplets within several hours of starting the patch clamp experiment and keeping the internal pipette solution on ice before inserting into the patch pipette. Another cause of nanodroplet injection failure was due to too high of pressures being used to inject the PFCnDs, resulting in rupturing of the cell from too great of a volume entering the cell too rapidly (15% of failed injections). This typically occurred at pressures exceeding 100 mBar. Future researchers can save time and prevent this from occurring by ending a nanodroplet injection attempt if the pressure they are testing exceeds 100 mBar. Another culprit of unsuccessful PFCnD injection was due to a lost gigaseal, which can occur if the cell membrane reseals on itself or if a large organelle is blocking entrance to the cell (27% of failed injections). This occurrence is an unfortunate side effect during patch clamping, and while gentle bursts of positive pressure can sometimes re-open the cell membrane, the pressure application does not always work. The last cause of nanodroplet injection failure is that no nanodroplets were present at the tip during injection.

The PFCnDs had a tendency to travel up the pipette away from the tip, likely due to capillary action, so to prevent this from happening it was important to constantly apply positive pressure (+10 mBar) while descending the pipette and only pausing the pressure when reaching the cell membrane. It was also important to visually inspect that a steady stream of nanodroplets was exiting the patch pipette tip even under gentle pressures (+10 mBar), otherwise the concentration of PFCnDs at the pipette tip was not sufficient (**Fig. 5.4 a**). This flow helped ensure that no clogs caused by the nanodroplets occurred and that nanodroplets were present at the pipette tip once the cell was broken into, thus enabling successful injection of the nanodroplets into the cell (**Fig. 5.4 b, c, d**).

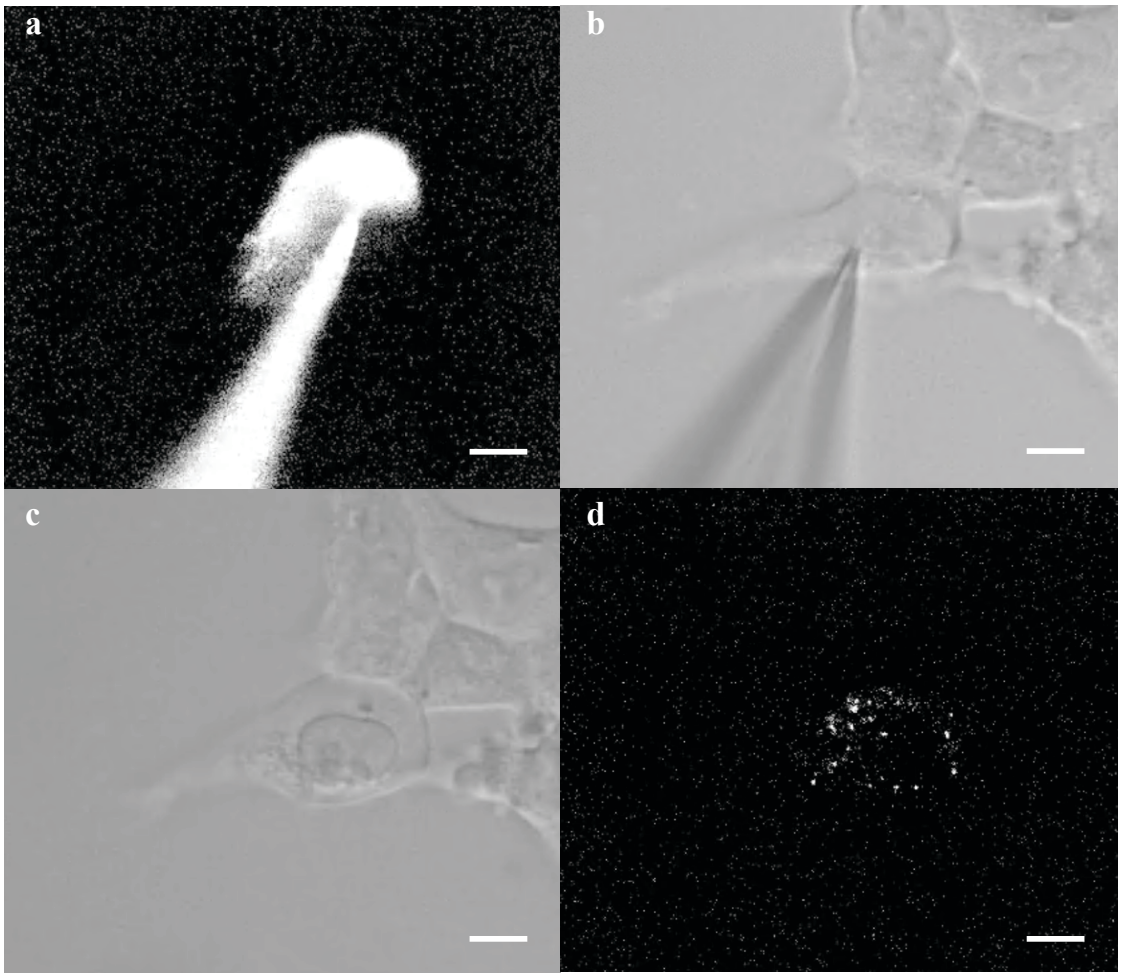

Figure 5.4. Patch clamp nanodroplet injection procedures. a. Ensure steady stream of nanodroplet flow out of pipette before/during patch pipette descent to cell. **b.** Cell during patch clamp injection. **c.** Cell after patch clamp injection. **d.** Fluorescent nanodroplets inserted into the cell. Scale bar = 5 μm.

5.3.2 Nanodroplet spread throughout HEK293T cells

A small cluster of nanodroplets at the injection site could be sufficient to locate the cell, but for future super-resolution applications of this imaging technique, where researchers may want to image the cell morphology itself, PFCnD spread throughout the entire cell morphology is critical. Therefore, we wanted to understand how the PFCnDs spread throughout the cell after injection. We developed a MATLAB script that created a

mask over the patched cell and calculated the % area that the nanodroplets took up as well as the nanodroplet spread from both ends of the cell (**Fig. 5.5 a-d**).

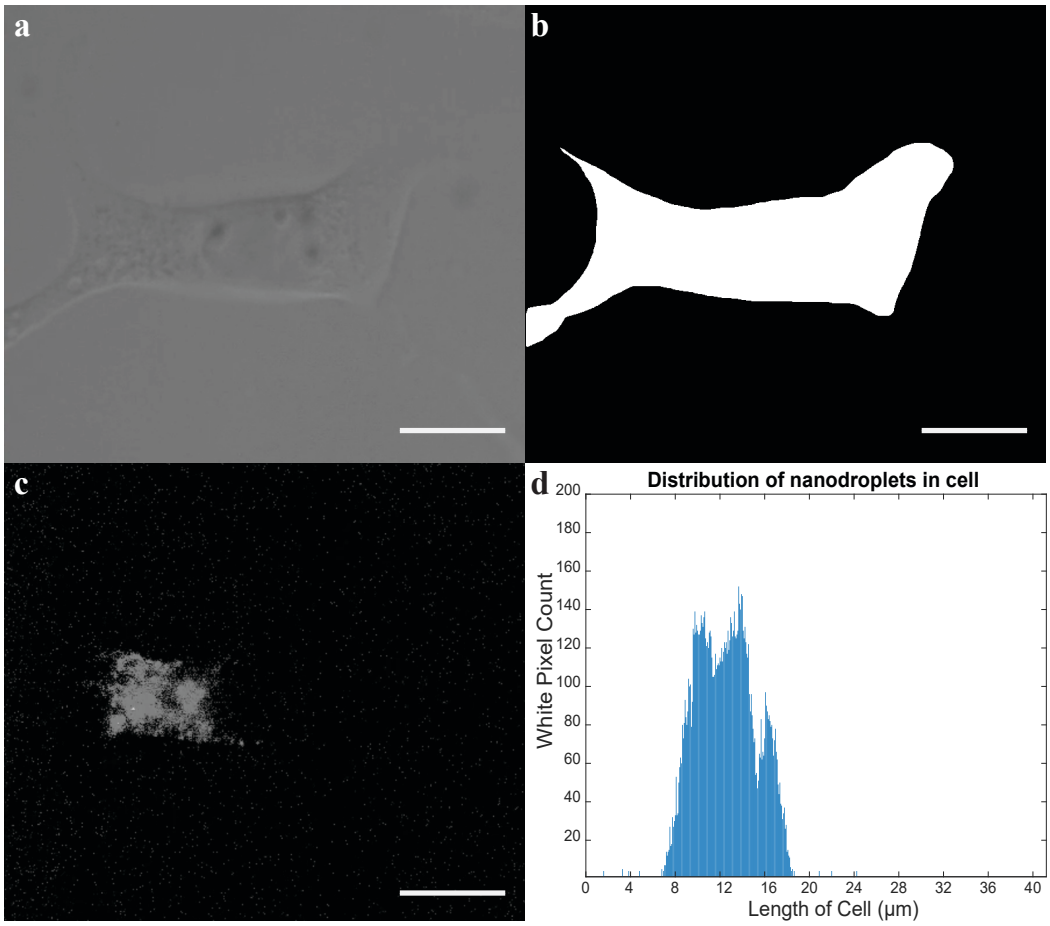

Fig. 5.5. Distribution of perfluorocarbon nanodroplets post-patch clamp microinjection. a. DIC image of a patch clamp microinjected HEK293T cell on a glass coverslip. **b.** Mask over the cell to denote the cell boundaries and area. **c.** Fluorescent image of the cell indicating position of the PFCnDs. **d.** Bar graph demonstrating distribution of PFCnDs throughout the length of the cell. Scale bar = 10 µm.

Quantifying spread, we noticed that the majority of cells had PFCnD spread throughout less than 50% of the cell (**Fig. 5.5 c, d**), with only one instance of nanodroplet spread exceeding 75% (**Table 5.2**). This is indicative that, although sufficient quantities of

PFCnDs enter cells to enable cell localization with ultrasound, the nanodroplets do not spread to all distal structures of the cell. Thus, improvements must be made to the injection technique to ensure that the nanodroplets do spread to all portions of the cell if this technique was to be used for cell morphology imaging. It is possible that PFCnDs would spread more evenly throughout the cell if cells were returned to a cell culture incubator after injection to encourage diffusive spread of the PFCnDs throughout the cell over time. However, because patch clamp rigs are not a sterile environment, and because of the presence of PFCnDs within the cell, we noticed cell infection several hours after injection. Preparing the PFCnDs with sterile reagents in a biological safety cabinet did increase cell survival time, but cell infection still occurred within 24 hr. Extra precautions must be taken should this technique be repeated with the desire for long-term cell viability post-PFCnD injection via patch clamp.

Table 5.2. Incidence of perfluorocarbon nanodroplets spread throughout HEK293T cells as a function of the farthest measured nanodroplet from injection origin.

PFCnD % Spread	Count
< 25%	12
25-50%	12
50-75%	9
>75%	1

We also examined whether there was a correlation between PFCnD spread throughout the cell and the pressure used to drive PFCnD movement from the patch pipette into the cell. We noted no correlation between the two metrics.

5.3.3 Ultrasound imaging of intracellular PFCnDs

Modifications to the experimental procedures were necessary to enable nanodroplet-injected cell transfer to occur seamlessly from the patch clamp rig to the ultrasound imaging set-up. For one, glass coverslips are not conducive to ultrasound imaging experiments due to the high acoustic impedance mismatch between the glass and aqueous environment of the ultrasound imaging set-up (c_{glass} = 5600 m/s and ρ_{glass} = 2200 kg/m^2 compared to c_{water} = 1500 m/s and ρ_{water} = 997 kg/m^2). This impedance mismatch, as described in Chapter 2, will cause most of the incident waves to be reflected at this boundary, preventing ultrasound imaging of the cells on the glass coverslip. Therefore, an alternative coverslip material must be used that is better suited for ultrasound imaging experiments. Once we felt confident in our capabilities to inject PFCnDs into HEK293T cells with our patch clamp parameters and protocol, we began growing the HEK293T cells on PDMS coverslips. PDMS is a soft and flexible polymer with impedance values more conducive to acoustic imaging (c_{PDMS} = 1076.5 m/s, ρ_{pdms} = 920 kg/m^2 compared to c_{water} = 1500 m/s and ρ_{water} = 997 kg/m^2) [146]. However, PDMS is extremely hydrophobic and requires surface treatment to grow cells on it successfully. We achieved this by first sterilizing the PDMS coverslips by soaking them in 70% ethanol for 30 minutes, flipping the coverslips halfway through so that all surfaces were sterilized. Once the ethanol was aspirated and the coverslips rinsed with PBS, the coverslips underwent UV exposure. This

helps to make the PDMS surface more hydrophilic [147]. The final step to make these PDMS coverslips conducive for cell adhesion and proliferation was to soak the coverslips in a 20% poly-d-lysine solution, diluted with PBS, for at least 1 hour at 37°C. At this point, the poly-d-lysine can be aspirated and HEK293T cells immediately cultured onto the coverslips for patch clamp experiments. HEK293T cells cultured on PDMS coverslips tended to have a more rounded appearance than those cultured on borosilicate glass coverslips (**Fig. 5.6 a**, **b**). This is likely because the PDMS surface is still more hydrophobic than borosilicate glass, even after all surface treatments and modifications, and thus the cells are less capable of spreading fully on the surface. However, these cells were still adherent to the coverslips, and we were able to patch clamp and microinject nanodroplets into these cells with relative ease.

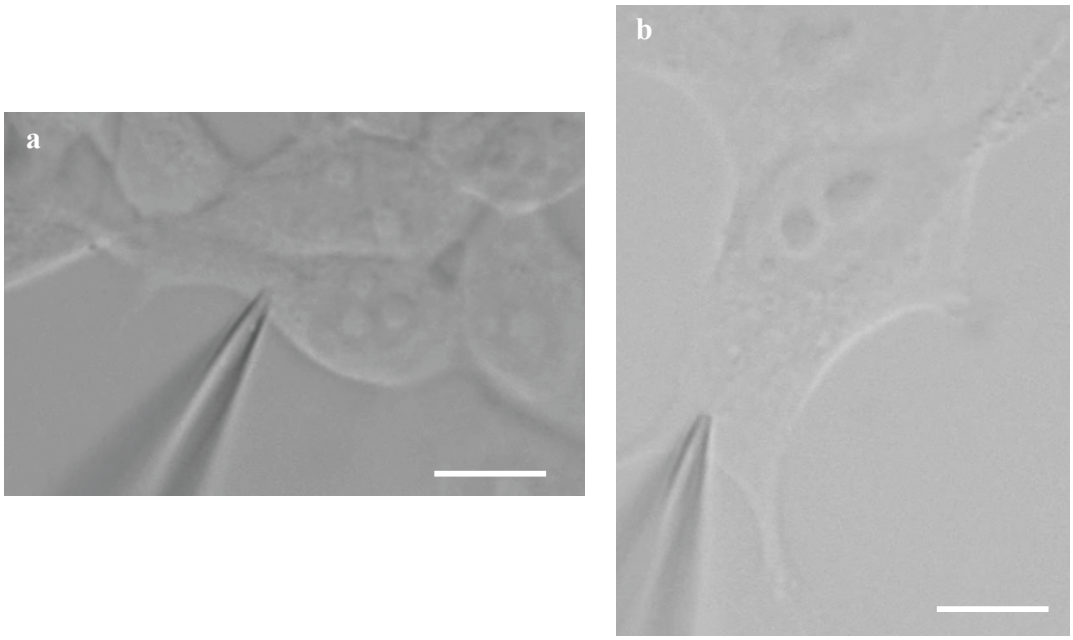

Figure 5.6. HEK293T cell morphology grown on PDMS coverslips versus glass coverslips. HEK293T cells grown on PDMS coverslips **(a)** exhibit a rounder morphology than HEK293T cells grown on glass coverslips **(b).** Scale bar = 10 μm.

Using PDMS as a coverslip material, rather than glass, has the added benefit that modifications can be made to the shape and features of the coverslip for improved ultrasound imaging accuracy. Specifically, we realized that it would be difficult to locate precisely where we patched each cell since the cell is not giving off acoustic contrast until the nanodroplets inside of it are phase transitioned to gas microbubbles using a focused ultrasound pulse. To fix this issue, we added an alignment marker on each coverslip in the form of a 1 mm hole created by a biopsy punch (**Fig. 5.7 a**). The hole appears as a faint circular inclusion on the coverslip while ultrasound imaging, so patching the cells near the perimeter of this alignment marker ensured that our focused ultrasound transducer was aligned to the cell we had injected with nanodroplets (**Fig. 5.7 b, c**).

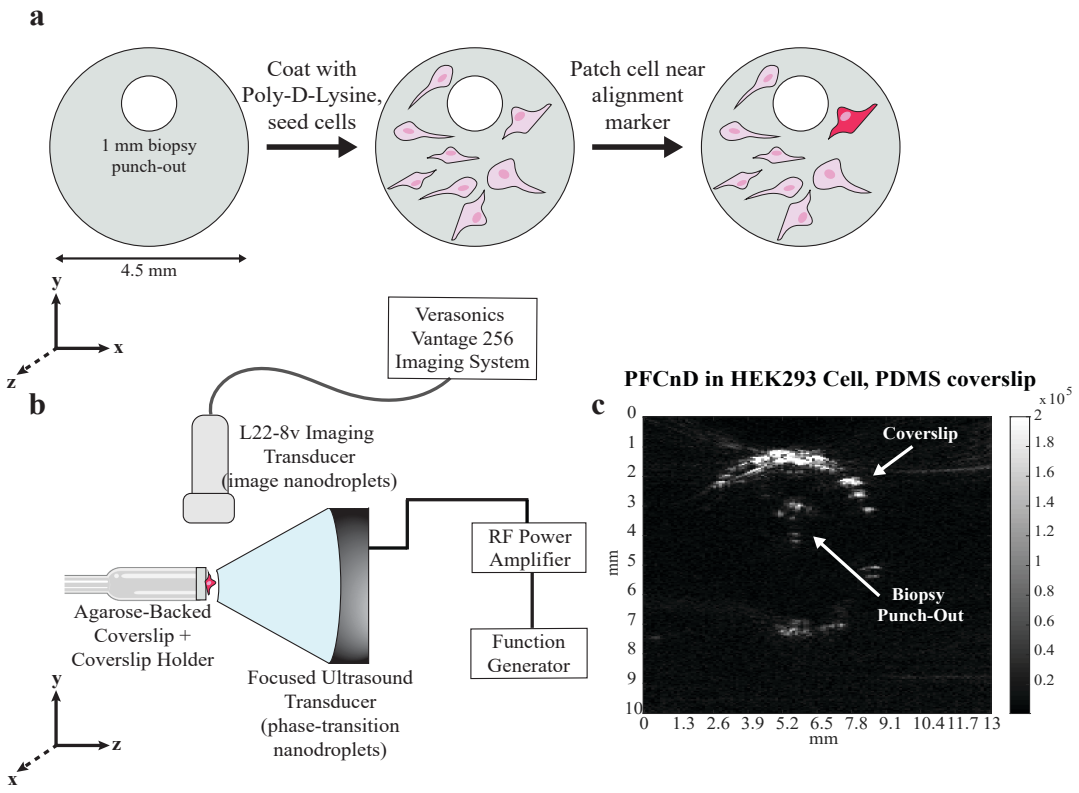

Figure 5.7. Methods for single cell localization of nanodroplet-injected HEK293T cells on PDMS coverslips. a. Diagram of process flow for creating PDMS coverslips seeded with HEK293T cells. **b.** Ultrasound imaging set-up for localizing the cell containing PFCnDs after patch-clamp microinjection. The PDMS coverslip containing the cell is coated with agarose and placed on an agarose-backed sample holder, aligned with a focused ultrasound transducer to induce phase-transitioning of the PFCnDs within the cell. A linear array transducer (L22-8v) is placed orthogonal to the set up and directly above the PFCnD-containing cell to capture B-mode images of the phase-transitioning PFCnDs. These images are collected and stored with a Verasonics Vantage programmable imaging system. **c.** B-mode image of the PDMS coverslip, which clearly shows the biopsy punch-out being used as an alignment marker to ensure the focal point of the focused ultrasound transducer is placed in line with the location of the PFCnD-containing cell.

After injecting PFCnDs into cells cultured on these PDMS coverslips and suspending the coverslip in an agarose gel for submersion in a water bath for ultrasound imaging, we learned that the cell morphology immediately changed upon addition of the

agarose gel. Furthermore, there was an increased risk of the cells sloughing off the coverslips during this procedure. To overcome this obstacle, we began fixing the cells to the PDMS coverslip using a 4% paraformaldehyde solution diluted in PBS. This helped maintain the cell morphology and keep the cell in place on the PDMS coverslip, even after being suspending in the agarose gel (**Fig. 5.8 a**), without affecting the spread of PFCnDs inside the cell (**Fig. 5.8 b, c**) nor impacting the PFCnD acoustic properties (**Fig. 5.9**).

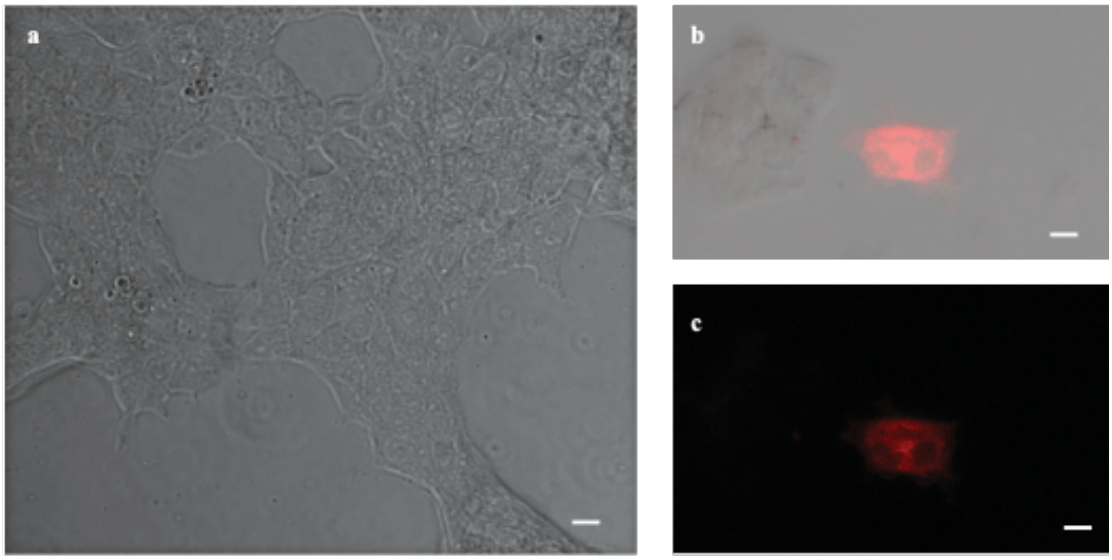

Figure 5.8. Fixed HEK293T cells on PDMS coverslips after patch clamp microinjection of perfluorocarbon nanodroplets. a. HEK293T cells fixed on PDMS coverslip with agarose gel overlay does not impact cell morphology. **b.** brightfield + fluorescence and **c.** fluorescence only images of HEK293T cell post-patch clamp microinjection of PFCnDs. Scale bar = 5 µm.

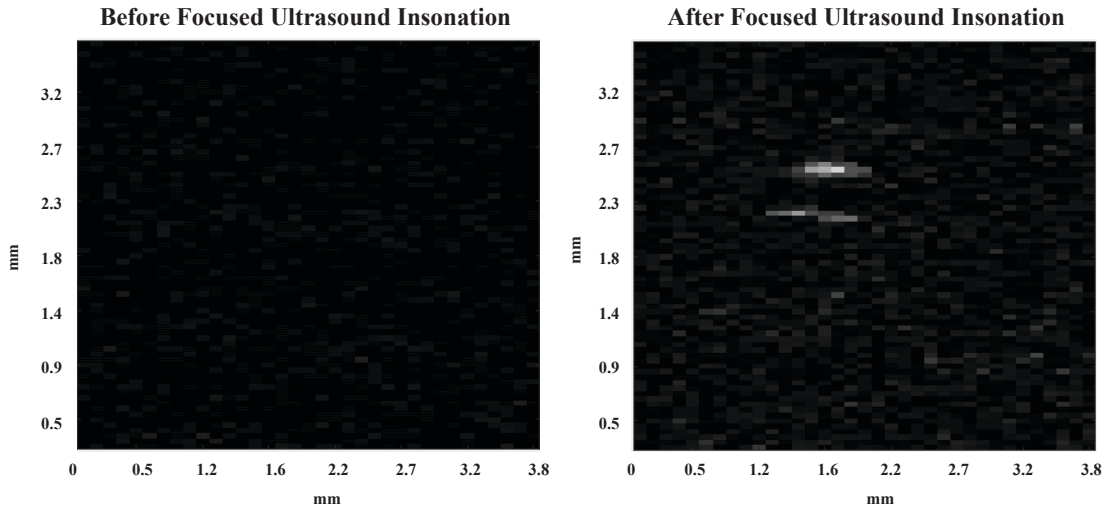

Figure 5.9. Phase transitioning of perfluorocarbon nanodroplets after fixation in 4% paraformaldehyde. PFCnDs are suspended in a 1% agarose gel at a concentration of 10^7 nanodroplets/mL. PFCnDs still exhibit phase-transitioning properties after paraformaldehyde fixation when insonated with the focused ultrasound transducer at 3 MPa peak negative pressure.

Once these modifications were made, we were able to ultrasonically image HEK293T cells injected via patch clamp with PFCnDs. First, we optically validated that the coverslip contained a HEK293T cell with PFCnDs inside, and we noted the location of that cell with reference to the alignment marker (**Fig. 5.10 a**). The coverslip was then loaded into the sample holder, covered in 1% agarose gel, and placed in the water bath for ultrasound imaging. We constantly recorded images with the linear array transducer to ensure that we were properly aligned with the sample and single-element focused ultrasound transducer, and that the alignment marker was visible and in alignment. Using the single-element transducer at its optimized operating frequency of 1.05 MHz and transmitting 6.5 MPa of peak negative pressure, we noticed repeated appearance and disappearance of a bright spot within the region of the patched HEK293T cell containing PFCnDs. This signal was indicative of the PFCnDs phase transitioning to gas microbubbles under ultrasound

insonation from the focused ultrasound transducer. Nanodroplet activity was noted every time the focused ultrasound transducer was triggered to transmit its signal (**Fig. 5.10 b**). This occurrence is the first demonstration of ultrasound imaging of a single cell using PFCnDs as an ultrasound contrast agent, and the first example of ultrasound imaging of cells after patch clamp microinjection of PFCnDs into the cell. The proof of concept of this technique has significant implications for researchers seeking to study cell activity and cell location in deep tissue structures, and even has potential for super-resolution of single cell morphology using microinjection of PFCnDs into cells. However, substantial work must be done to increase the throughput of ultrasound images of cells by streamlining the procedure of generating these nanodroplet-injected cells, properly aligning them for ultrasound imaging, and validating sufficient nanodroplet injection and spread within the cell. Furthermore, more work must be done on the image reconstruction technique used to analyze this cell imaging data if single-cell super-resolution ultrasound imaging were to ever be realized.

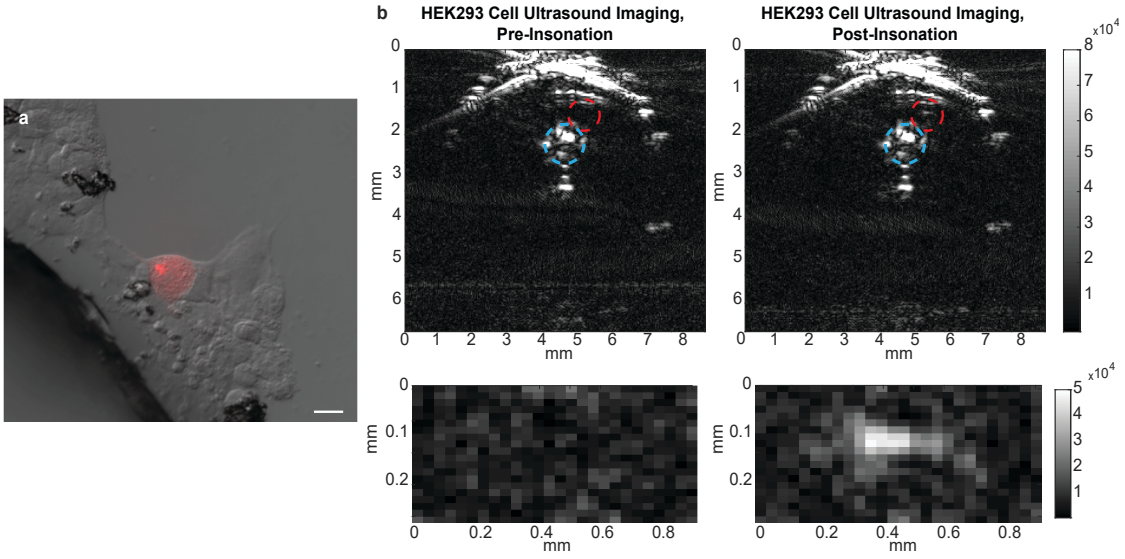

Figure 5.10. **Patch clamp microinjected HEK293T cell fixed on a PDMS coverslip produces ultrasound contrast. a.** Fixed HEK293T cell on a PDMS coverslip with DiI-tagged PFCnDs inside. **b.** Ultrasound images pre-insonation (left) and post-insonation (right) demonstrating PFCnDs phase-transitioning to gas microbubbles in the fixed HEK293T cell located on the coverslip, with zoomed in images to highlight the ultrasound contrast. Focal region is indicated in red dashed circle and alignment marker is in blue dashed circle. Scale bar = 20 μm.

5.4 Discussion

Single-cell imaging using PFCnDs inserted into cells via patch clamp microinjection can be a useful technique for ultrasound imaging and has many potential applications. For example, cells can be injected with these nanodroplets *in vivo* and studied within the subject. A subset of cells can be microinjected via patch clamp and then placed into an *in vivo* environment to study their migration within the subject. Another potential application is super-resolution imaging using techniques like ultrasound localization microscopy or other acoustic STORM/PALM analogs. As mentioned previously, PFCnDs can stochastically expand and recondense in sparse subsets in an acoustically analogous manner to the fluorophores in PALM and STORM, meaning PFCnDs could be imaged in this manner to achieve super-resolution imaging of cells and tissue structures. Already,

several research groups have produced work on super-resolution imaging within tissues using PFCnDs, and super-resolution ultrasound imaging is a growing interest of many research groups.

These research findings are the first to demonstrate perfluorocarbon nanodroplet injection into living mammalian cells using patch clamp. The combination of these two techniques creates potential research avenues for cellular imaging of neurons after patch clamp microinjection of these ultrasound contrast agents. As one example, neuroscience researchers are trying to uncover what happens to various cells within the brain over short and long-term time spans, including in disease models such as Alzheimer's disease or Parkinson's disease. The current imaging techniques for *in vivo* cell activity is fluorescence microscopy by tagging certain cells with a fluorescent marker and studying the growth and movement of that cell in brain tissue through a thinned skull of a mouse, rat, or other animal model. This technique has unveiled unique recruitment of microglia in Alzheimer's mouse models within the cortex [148]. However, because of inherent light penetration limitations in tissue, only the most superficial layer of brain cells can be imaged and requires substantial surgery (skull thinning, replacement of skull with glass slide) to image. Moving away from optics and towards ultrasound for cellular imaging could be the key to achieve single-cell, deep tissue imaging if used in conjunction with patch clamp microinjection to reach those deep cells and inject the necessary contrast agent.

However, there are some challenges associated with this technique that must be addressed to expand the use cases, particularly for *in vivo* applications. For one, as noted in *5.3.2*, the nanodroplets do not spread uniformly and evenly throughout the cell after injection. While this is not a problem for cell localization, it can be an issue if this technique

is to be used for cell morphology reconstruction using ultrasound localization microscopy or other super-resolution imaging techniques as some nanodroplets may not be present at the distal structures of the cell, preventing an accurate representation of the cell morphology. Additionally, the cell can become unhealthy after being injected with these nanodroplets. Some cell health experiments were conducted as part of this study. If the nanodroplets are not fabricated in a sterile environment (i.e., a biological safety cabinet) cell degradation will occur immediately after injection. After creating new, sterile solutions and fabricating all of the PFCnDs in a biological safety cabinet, we noted that cells were stable for about 12 hours. Afterward, notable cell infection and cell death was reported. This infection could be caused by the non-sterile patch clamp environment, but also could be due to stress on the cell caused by foreign materials being inserted into it or caused by a poor interaction of an ingredient used to fabricate the PFCnDs with the cell. We noted that cells, after microinjected with a GFP plasmid only, were able to survive post-patch clamp microinjection for 3 days and continue undergoing cell division (**Fig. 5.11**). Therefore, while the patch clamp environment's lack of sterility may contribute to the cell infection after PFCnD microinjection, the PFCnDs are likely the main reason why cells appear unhealthy 12+ hours after the procedure. Further studies must be conducted to determine how to increase cell survival periods after PFCnD injection.

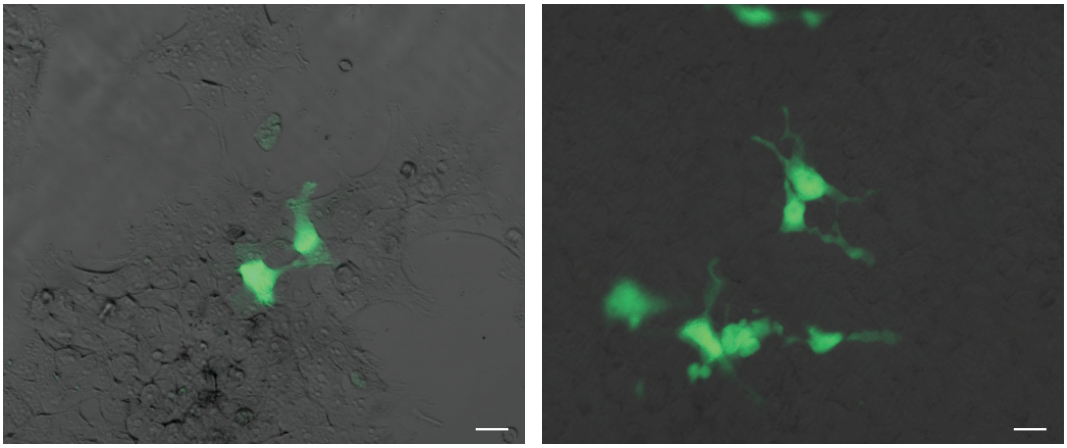

Figure 5.11. Cell viability after patch clamp microinjection. HEK293T cells patch clamp microinjected with GFP plasmid after 12 hours (left) and after 3 days (right). Cells appear healthy and capable of generating daughter cells that contain and express the GFP plasmid. No signs of infection were noticed after 3 days post-patch clamp. Scale bar = 20 μm.

Another potential issue with this technique is the stability of nanodroplets *in vivo* and the pressures required to induce phase transitioning of the PFCnDs from droplets into gas microbubbles. As mentioned previously in this work, the PFCnDs could enlarge and cause clogs at the pipette tip. This PFCnD swelling is likely the cause of Ostwald ripening, hence why it is crucial to filter the PFCnDs before insertion into cells. However, if this Ostwald ripening was to occur inside the cells themselves, it could lead to the formation of large nanodroplets, eventually forming microdroplets and potentially causing harm within the cell. For example, if a perfluorocarbon with a lower boiling point is used (e.g., perfluorobutane, bp = -1.7^{o}C), the larger droplet formed via Ostwald ripening is more likely to spontaneously expand into a gas microbubble than PFCnDs containing a perfluorocarbon with a higher boiling point. If this were to occur within a cell, the rapid expansion of such a large droplet could cause permanent damage to the cell. With regard

to pressures required to induce phase transitioning, we tried to use higher boiling point perfluorocarbons to improve stability within the cell at physiological temperatures (e.g., perfluoropentane, bp = 29ºC and perfluorohexane, bp = 56ºC). However, using these perfluorocarbons meant that we needed to use pressures and frequencies that exceeded the MI limit of 1.9, indicating that these experiments would not be safe to perform *in vivo*. Changes can be made to the nanodroplet composition to prevent this from happening as much as possible, like using lower boiling point perfluorocarbons or working with slightly larger nanodroplets (300 nm diameters rather than 200 nm), but this causes issues regarding Ostwald ripening and stability at biological temperatures. The above problems are not unique to only this application of perfluorocarbon nanodroplets. One of the likely culprits as to why perfluorocarbon nanodroplets are not FDA approved, despite being around for over 20 years, is the high pressures required to induce phase transitioning. Ideally, new materials or phase-transitioning nanodroplet fabrications will be created that overcome some of these limitations and thus we would be able to see these PFCnDs used in the future.

5.5 Conclusions

This work made crucial strides towards single cell localization and imaging using intracellular perfluorocarbon nanodroplets. We demonstrate repeatable PFCnD injection into HEK293T cells using patch clamp and describe recommendations based on pressure and duration settings that can be applied to successfully achieve nanodroplet injection while providing troubleshooting tips to improve reliability of this technique. Furthermore, we outline a protocol for seamless transition of injected HEK293T cells from the patch clamp rig to an ultrasound imaging set-up by switching to PDMS coverslips with a 1 mm

alignment marker, fixing the cells on the PDMS coverslip to prevent morphology changes and potential cell loss. We end the chapter with the demonstration of cell localization using ultrasound imaging by identifying a bright spot appearing periodically post-ultrasound insonation near a coverslip alignment marker.

Chapter 6

CONCLUSIONS AND FUTURE DIRECTIONS

6.1 Review of Findings

Collectively, the work described herein expands the use of ultrasound contrast agents towards intracellular imaging applications. Chapter 2 provided background information on the physics of ultrasound contrast agents, in particular gas microbubbles and perfluorocarbon nanodroplets, but also focusing on the newer gas vesicles and genetic expression of these gas vesicles in mammalian cell lines. Chapter 2 also reviews patch clamp and its use as a small molecule delivery mechanism during electrophysiology experiments. Chapter 3 describes our work towards simplifying mARG integration in mammalian cell lines by making the mARG sequence drug selectable ($mARG_{ds}$). We demonstrate that HEK293T cells can produce gas vesicles at sufficient levels to generate ultrasound contrast through doxycycline-induced $mARG_{ds}$ expression and antibiotic treatment to eliminate any cells that failed to integrate the $mARG_{ds}$ construct. This eliminates the need to use FACS or single cell cloning, reducing the cost, time, and effort required to generate gas vesicle-producing mammalian cells.

Chapters 4 and 5 explore an alternative contrast agent useful for single cell ultrasound imaging by focusing on the perfluorocarbon nanodroplet ultrasound contrast agent. In Chapter 4, we explore the lipid shell parameter space of PFCnDs by varying the amounts of PEGylated and non-PEGylated lipids in the PFCnD lipid shell. First, these nanodroplets were fabricated using a spontaneous nucleation technique and underwent different methods of size-exclusion separation to eliminate large droplets, which could skew the nanodroplet dynamics if significant quantities of larger nanodroplets (>300 nm

diameters) were present. Next, we determined that PFCnDs with an equal molar ratio of non-PEGylated and PEGylated lipids in the shell appeared to produce the strongest B-mode ultrasound contrast, smallest nanodroplets, and had the largest pressure differential between ADV onset and IC onset amongst all nanodroplet types tested. These results demonstrate that the 50:50 non-PEGylated:PEGylated PFCnDs possess the ideal shell composition if the desired use case is for biomedical imaging, especially for *in vivo* imaging, due to its bright signal and reduced risk of inertial cavitation. Nanodroplets with this lipid shell composition were used in Chapter 5, where we utilized patch clamp for single cell injection of PFCnDs into HEK293T cells. We first worked with HEK293T cells cultured on glass coverslips and studied the pressure and time parameters needed to drive PFCnDs from the patch pipette into the cell. We identified key causes of patch clamp injection failure, even after successful cell break-in. We also describe in this chapter a protocol for direct transfer of PFCnD-injected HEK293T cells from the patch clamp rig to an ultrasound imaging set-up by switching to PDMS coverslips, fixing the cells to the coverslip to prevent changes to the cell morphology and to prevent the cells from migrating off of the coverslip once embedded in a gel phantom, and use of alignment markers for aid in positioning the sample aligned to the focal point of the single element transducer, which is used to phase transition the liquid PFCnDs into gas microbubbles for ultrasound imaging. We conclude Chapter 5 by demonstrating single-cell localization via repeated ultrasound insonation of the PFCnDs contained within a cell on a PDMS coverslip.

6.2 Implications and Future Directions

6.2.1 Gas vesicle expression in pluripotent stem cells

The next direction of our research with gas vesicle expression in cell lines is towards implementing $mARG_{ds}$ expression in pluripotent stem cells for imaging during stem cell therapies. At the moment, various forms of stem cells are being investigated in clinical trials for treatment of numerous diseases, including blindness caused by macular degeneration, cartilage and bone regeneration to improve back pain, and spinal cord repair [149]. While it is promising that there are so many Phase I and Phase II clinical trials of various stem cell therapies, many of these trials fail and to this date the only approved stem cell treatment is hematopoietic stem cell transplant. One issue is the risk of these transplanted stem cells forming tumors *in vivo* [150]. Another issue lies in the host's immune response to these stem cells [151,152]. Lastly, there are issues with monitoring where the transplanted cells migrate to and how they proliferate. Researchers can use fluorescent markers to study cells at superficial tissue levels, but it is challenging to monitor transplanted cells in deep tissue regions. Gas vesicle expression in stem cells using mARGs could overcome this obstacle and enable researchers to visualize and track cell behavior and migratory patterns over long periods of time with noninvasive ultrasound imaging.

Unfortunately, significant challenges remain in achieving successful gas vesicle expression after stably transfecting iPSCs with $mARG_{ds}$. Already, we have attempted to generate gas vesicle-expressing iPSCs using both the first generation and second generation of mARGs. While we have demonstrated some amount of $mARG_{ds}$ expression by optically confirming GFP expression in transfected iPSCs, these cells failed to produce

any ultrasound contrast, and gas vesicles were not observable under phase contrast microscopy even after several days of doxycycline treatment. This may be indicative of the fact that, while the gas vesicle proteins are being generated by the cell, they are not properly assembling into gas vesicles. Further research must be conducted to improve the ease in which mammalian cells, especially iPSCs, integrate and express mARGs in order for this research pathway to continue. While recent work by Mikhail Shapiro's research group has demonstrated progress since the first generation of mARGs from 2019, and our research has improved mARG integration by creating drug selectable mARGs, more work must be done to make this technique more broadly applicable [41].

6.2.2 Super-resolution ultrasound imaging of single cells

Super-resolution ultrasound imaging is an exciting field that requires the use of gas-filled contrast agents. Since the development of PALM and STORM imaging, two non-linear optical imaging technique that improved the resolution of fluorescently labeled microscope images by two orders of magnitude (100's of nm to single nm resolution), ultrasound researchers have been working to develop an acoustic analog to this technique. The closest researchers have gotten to this goal is ultrasound localization microscopy (ULM), which tracks microbubble movement in blood vessels. With ULM, researchers have been able to reconstruct microvasculature in a mouse brain with μm-scale resolution (100-fold improvement). However, since microbubbles are primarily restricted to vasculature, work must be done to achieve super-resolution imaging using other ultrasound contrast agents. Some research has been done using perfluorocarbon nanodroplets to achieve precise localization of these PFCnDs contained within tissue phantoms, and

micron-scale resolution has been achieved with various image processing techniques of these PFCnDs. Furthermore, a theoretical paper described the feasibility of sub-micron ultrasound image resolution using an 18 MHz transducer and PFCnDs [59]. However, no work has been done to localize PFCnDs to cells for ultrasound imaging applications. If PFCnDs are added to cells, which up until recently was typically achieved through surface treatment of the PFCnDs to encourage cell uptake, the PFCnDs are then insonated to cause inertial cavitation, thus destruction of the PFCnD itself for the release of a payload within the nanodroplet. To our knowledge, no work has been done towards ultrasonic single cell localization or cellular imaging with micron-scale resolution using PFCnDs. Additionally, no experimental work has physically realized sub-micron scale resolution in ultrasound images using PFCnDs or any other ultrasound contrast agent.

Because there is such a gap in the field, we are excitedly exploring the potential of using PFCnDs for super-resolution imaging of cells. This work describes necessary first steps towards isolating PFCnDs into single, targeted cells using patch clamp and other steps required to achieve ultrasound imaging of these cells *in vitro*. Eventually, we would like to expand this research towards both *in vivo* imaging of single cells and towards super-resolution of single cells, *in vitro* and *in vivo*, to reconstruct a cell's morphology using ultrasound imaging only. Substantial work must still be done to elucidate the necessary image reconstruction steps for achieving this super-resolution as well as proper nanodroplet injection and distribution conditions within the cell. Furthermore, for *in vivo* applications, the safety and stability of intracellular PFCnDs must be further investigated. To explore long term PFCnD safety in cells, future experiments include cell viability trials, which will require nanodroplet microinjection into cultured cells on coverslips and subsequent

suspension in Matrigel or another matrix scaffold for sustained cell and tissue culture. Along with the PFCnDs, a GFP plasmid will be added to the microinjector internal solution. Once cells are injected with PFCnDs and GFP plasmid, they will be removed from the coverslip using trypsin, suspended in Matrigel, and transferred to an ultrasound imaging sample holder. After exposure to repeated focused ultrasound pulses at pressures sufficient to induce PFCnD droplet vaporization, the Matrigel cell suspension will be placed in cell culture media and transferred to a cell culture incubator for at least three hours. After this period, the Matrigel cell suspension will be optically imaged using fluorescence microscopy to check for the presence of GFP-expressing cells that also contain the DiI-tagged PFCnDs. If these cells are present, this will be indicative that cells could withstand the ultrasound imaging conditions necessary for cell localization and super-resolution imaging, as demonstrated by successful GFP plasmid expression. If these cells are not present, experimental conditions must be altered to guarantee cell health after ultrasound imaging, which may include changes to PFCnD composition, insonating pressures used, and the duration of ultrasound exposure. If cell viability and super-resolution image reconstruction experiments are successful, the use of ultrasound and contrast agents for single cell super-resolution imaging could become a reality.

6.2.3 Ultrasound contrast agents for brain imaging and therapies

Ultrasound imaging of gas vesicles and PFCnDs contained within neural cells of an animal model could help researchers answer many of the greatest questions that puzzle neuroscientists to this day. With PFCnDs, if they can be injected into single neurons using *in vivo* patch clamp, it is feasible that the morphology and location of the cell could be studied *in situ* over multiple days or weeks, thus answering questions regarding learning, neuroplasticity, new synapse formation, or migration of certain cell types like microglia within the deep brain. Some optical studies have conducted multi-week investigations of how microglia travel throughout the surface of the brain within an aging, Alzheimer's model mouse [148]. However, because of tissue penetration limits of light, these studies can only be conducted on the most superficial layers of the brain. Ultrasound's capability to penetrate deeper into tissue is an immense strength in this case, and being able to capture micron or sub-micron resolution images of cell structures in deep tissue would create huge strides in the neuroscience field.

One of the biggest limitations to any sort of brain imaging using ultrasound techniques is the presence of the skull. The skull substantially scatters ultrasound, and higher amplitude acoustic waves can cause local heating and potential damage to the bone and nearby tissue. Even if an acoustic wave of sufficient amplitude penetrates through the skull, it cannot reflect off objects of interest within the brain tissue and pass back through the skull for the transducer to receive without substantial loss and permutation to the incident wave, making it nearly impossible to reconstruct an ultrasound image. Additional work on acoustic metamaterials could enable minimally invasive or non-invasive deep tissue brain imaging by eliminating the need to thin or remove the skull before imaging.

We have conducted work on acoustic metamaterials that could enable through-skull imaging by using a tunable circuit to match the density and bulk modulus of the skull such that ultrasound can travel past the skull and penetrate into tissue without loss (**Fig. 6.1**). By creating a non-Hermitian complementary metamaterial (NHCMM) with the negative density and bulk modulus of the skull, we simulated that acoustic waves could penetrate through the skull with minimal loss [153]. More recently, we published a paper focused on a tunable NHCMM that, if designed to match the shape and thickness of the skull, can enable bidirectional ultrasound transmission through the non-uniform skull section; without matching the skull shape, the acoustic metamaterial does not work (**Fig. 6.2**) [154]. Coupling these acoustic metamaterials with either gas vesicles or perfluorocarbon nanodroplets could enable long-term, *in vivo* imaging of cells in deep brain regions.

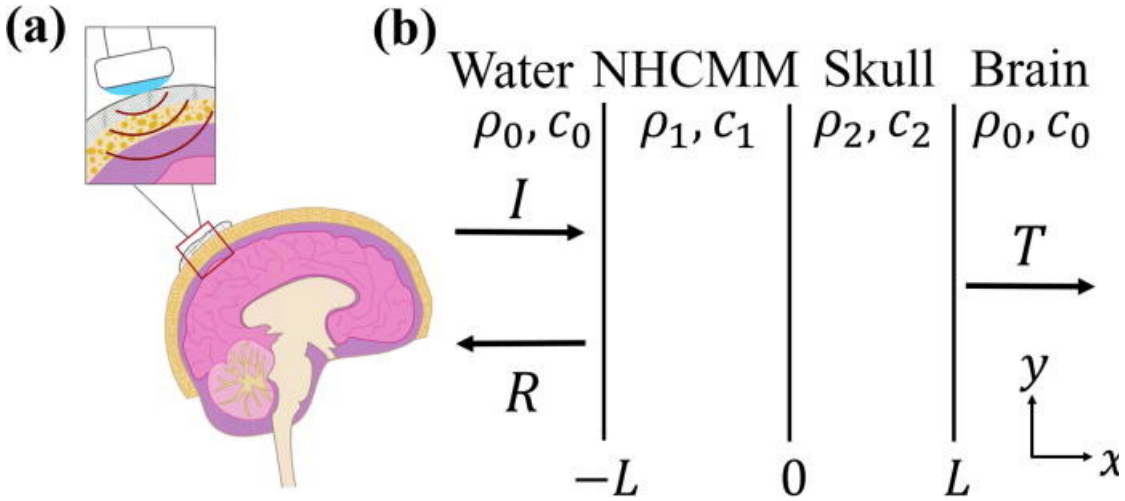

Figure 6.1: Non-Hermitian complementary metamaterial (NHCMM) for noninvasive ultrasonic brain imaging. a. Schematics of the NHCMM when applied for ultrasound imaging through an intact skull. **b.** Simplified model of acoustic wave propagation through the combined skull and NHCMM layers. Figure replicated from Ref. 153.

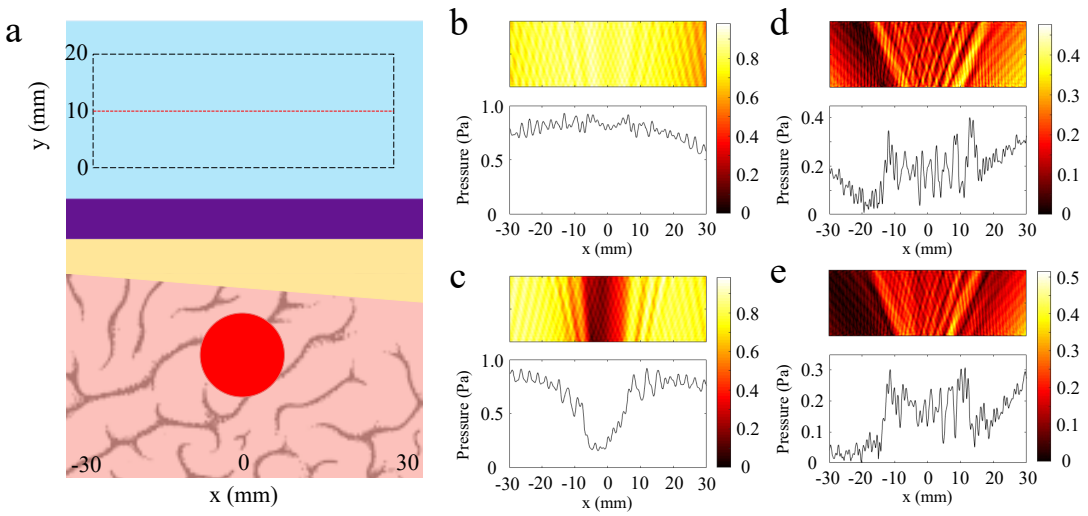

Figure 6.2: NHCMM matching of sloped skull conditions. a. Illustration of the skull sloping model used in full wave simulations. Plane wave incidence from the top of the subfigure. Reflected pressure fields are taken in the black dashed rectangles with the pressure amplitude recorded on the red dashed line. **b.** Scattered pressure field from imaging through a skull with an internal slope of 1.67% compensated by a flat metamaterial. **c.** Scattered pressure field from imaging through a skull with a larger internal slope of 3.33% compensated by a flat metamaterial. **d.** Scattered pressure field from imaging through a skull with a 1.67% slope compensated by a metamaterial with the mirrored skull geometry. **e.** Scattered pressure field from imaging through a skull with a 3.33% slope compensated by a metamaterial with the mirrored skull geometry. The color bars represent pressure amplitudes in Pa. Figure replicated from Ref. 154.

Further work must be conducted to determine the best way to deliver the ultrasound contrast agents to the brain if we were to pursue this research path. Non-invasive methods of delivering drugs past the blood brain barrier (BBB) have exploited microbubbles to temporarily create pores in the BBB for drugs to pass through [155]. This same technique could be used for gas vesicles or PFCnDs to enter brain tissue. For more targeted delivery of contrast agents, cells expressing mARGs could be transplanted into the brain tissue through craniotomy, or single-cell patch clamp could insert PFCnDs into cells within deep brain regions of an animal subject. However, these methods are fairly invasive.

REFERENCES

1 Goldberg, B. B., Gramiak, R. & Freimanis, A. K. Early history of diagnostic ultrasound: the role of American radiologists. *AJR Am J Roentgenol* **160**, 189-194 (1993).

2 Roman, M. J., Naqvi, T. Z., Gardin, J. M., Gerhard-Herman, M., Jaff, M. & Mohler, E. American Society of Echocardiography Report: Clinical application of noninvasive vascular ultrasound in cardiovascular risk stratification: a report from the American Society of Echocardiography and the Society for Vascular Medicine and Biology. *Vascular medicine* **11**, 201-211 (2006).

3 Moon, W. K., Lo, C. M., Chen, R. T., Shen, Y. W., Chang, J. M., Huang, C. S., Chen, J. H., Hsu, W. W. & Chang, R. F. Tumor detection in automated breast ultrasound images using quantitative tissue clustering. *Medical physics* **41**, 042901 (2014).

4 Cameron, M. & Moran, P. Prenatal screening and diagnosis of neural tube defects. *Prenatal Diagnosis: Published in Affiliation With the International Society for Prenatal Diagnosis* **29**, 402-411 (2009).

5 Christensen-Jeffries, K., Couture, O., Dayton, P. A., Eldar, Y. C., Hynynen, K., Kiessling, F., O'Reilly, M., Pinton, G. F., Schmitz, G. & Tang, M.-X. Super-resolution ultrasound imaging. *Ultrasound in medicine & biology* **46**, 865-891 (2020).

6 Ng, A. & Swanevelder, J. Resolution in ultrasound imaging. *Continuing Education in Anaesthesia Critical Care & Pain* **11**, 186-192 (2011).

7 Zhou, Y.-F. High intensity focused ultrasound in clinical tumor ablation. *World journal of clinical oncology* **2**, 8 (2011).

8 Wang, J., Zheng, Z., Chan, J. & Yeow, J. T. Capacitive micromachined ultrasound transducers for intravascular ultrasound imaging. *Microsystems & Nanoengineering* **6**, 73 (2020).

9 Satir, S. & Degertekin, F. L. Phase and amplitude modulation methods for nonlinear ultrasound imaging with CMUTs. *IEEE transactions on ultrasonics, ferroelectrics, and frequency control* **63**, 1086-1092 (2016).

10 Hoskins, P. R., Martin, K. & Thrush, A. *Diagnostic ultrasound: physics and equipment*. (CRC Press, 2019).

11 Szabo, T. L. *Diagnostic ultrasound imaging: inside out*. (Academic press, 2004).

12 Yan, G.-P., Robinson, L. & Hogg, P. Magnetic resonance imaging contrast agents: overview and perspectives. *Radiography* **13**, e5-e19 (2007).

13 Ignee, A., Atkinson, N. S., Schuessler, G. & Dietrich, C. F. Ultrasound contrast agents. *Endoscopic ultrasound* **5**, 355 (2016).

14 Christiansen, C. X-ray contrast media—an overview. *Toxicology* **209**, 185-187 (2005).

15 Lusic, H. & Grinstaff, M. W. X-ray-computed tomography contrast agents. *Chemical reviews* **113**, 1641-1666 (2013).

16 Blomley, M. J., Cooke, J. C., Unger, E. C., Monaghan, M. J. & Cosgrove, D. O. Microbubble contrast agents: a new era in ultrasound. *BMJ* **322**, 1222-1225 (2001).

17 Frinking, P., Segers, T., Luan, Y. & Tranquart, F. Three decades of ultrasound contrast agents: a review of the past, present and future improvements. *Ultrasound in Medicine & Biology* **46**, 892-908 (2020).
18 Piscaglia, F. & Bolondi, L. The safety of Sonovue® in abdominal applications: Retrospective analysis of 23188 investigations. *Ultrasound in medicine & biology* **32**, 1369-1375 (2006).
19 Jakobsen, J. Å., Oyen, R., Thomsen, H. S., Morcos, S. K. & org, M. o. C. M. S. C. o. E. S. o. U. R. h. w. e. Safety of ultrasound contrast agents. *European radiology* **15**, 941-945 (2005).
20 Li, Q., Yang, K., Ji, Y., Liu, H., Fei, X., Zhang, Y., Li, J. & Luo, Y. Safety Analysis of Adverse Events of Ultrasound Contrast Agent Lumason/SonoVue in 49,100 Patients. *Ultrasound in Medicine & Biology* **49**, 454-459 (2023).
21 Wei, K., Mulvagh, S. L., Carson, L., Davidoff, R., Gabriel, R., Grimm, R. A., Wilson, S., Fane, L., Herzog, C. A. & Zoghbi, W. A. The safety of Definity and Optison for ultrasound image enhancement: a retrospective analysis of 78,383 administered contrast doses. *Journal of the American Society of Echocardiography* **21**, 1202-1206 (2008).
22 Izadifar, Z., Babyn, P. & Chapman, D. Ultrasound cavitation/microbubble detection and medical applications. *Journal of Medical and Biological Engineering* **39**, 259-276 (2019).
23 Shen, C.-C., Chou, Y.-H. & Li, P.-C. Pulse inversion techniques in ultrasonic nonlinear imaging. *Journal of Medical Ultrasound* **13**, 3-17 (2005).
24 Pasovic, M., Danilouchkine, M., Faez, T., Van Neer, P. L., Cachard, C., van der Steen, A. F., Basset, O. & de Jong, N. Second harmonic inversion for ultrasound contrast harmonic imaging. *Physics in Medicine & Biology* **56**, 3163 (2011).
25 Errico, C., Pierre, J., Pezet, S., Desailly, Y., Lenkei, Z., Couture, O. & Tanter, M. Ultrafast ultrasound localization microscopy for deep super-resolution vascular imaging. *Nature* **527**, 499-502 (2015).
26 Yu, J., Lavery, L. & Kim, K. Super-resolution ultrasound imaging method for microvasculature in vivo with a high temporal accuracy. *Scientific reports* **8**, 1-11 (2018).
27 Song, P., Trzasko, J. D., Manduca, A., Huang, R., Kadirvel, R., Kallmes, D. F. & Chen, S. Improved super-resolution ultrasound microvessel imaging with spatiotemporal nonlocal means filtering and bipartite graph-based microbubble tracking. *IEEE transactions on ultrasonics, ferroelectrics, and frequency control* **65**, 149-167 (2017).
28 O'Reilly, M. A. & Hynynen, K. A super-resolution ultrasound method for brain vascular mapping. *Medical physics* **40**, 110701 (2013).
29 Ellegala, D. B., Leong-Poi, H., Carpenter, J. E., Klibanov, A. L., Kaul, S., Shaffrey, M. E., Sklenar, J. & Lindner, J. R. Imaging tumor angiogenesis with contrast ultrasound and microbubbles targeted to αvβ3. *Circulation* **108**, 336-341 (2003).
30 Pochon, S., Tardy, I., Bussat, P., Bettinger, T., Brochot, J., von Wronski, M., Passantino, L. & Schneider, M. BR55: a lipopeptide-based VEGFR2-targeted ultrasound contrast agent for molecular imaging of angiogenesis. *Investigative radiology* **45**, 89-95 (2010).

31 Willmann, J. K., Bonomo, L., Testa, A. C., Rinaldi, P., Rindi, G., Valluru, K. S., Petrone, G., Martini, M., Lutz, A. M. & Gambhir, S. S. Ultrasound molecular imaging with BR55 in patients with breast and ovarian lesions: first-in-human results. *Journal of Clinical Oncology* **35**, 2133 (2017).

32 Lentacker, I., De Smedt, S. C. & Sanders, N. N. Drug loaded microbubble design for ultrasound triggered delivery. *Soft Matter* **5**, 2161-2170 (2009).

33 Lensen, D., Gelderblom, E. C., Vriezema, D. M., Marmottant, P., Verdonschot, N., Versluis, M., De Jong, N. & Van Hest, J. C. Biodegradable polymeric microcapsules for selective ultrasound-triggered drug release. *Soft Matter* **7**, 5417-5422 (2011).

34 Edsall, C., Khan, Z. M., Mancia, L., Hall, S., Mustafa, W., Johnsen, E., Klibanov, A. L., Durmaz, Y. Y. & Vlaisavljevich, E. Bubble cloud behavior and ablation capacity for histotripsy generated from intrinsic or artificial cavitation nuclei. *Ultrasound in medicine & biology* **47**, 620-639 (2021).

35 Matsunaga, T. O., Sheeran, P. S., Luois, S., Streeter, J. E., Mullin, L. B., Banerjee, B. & Dayton, P. A. Phase-change nanoparticles using highly volatile perfluorocarbons: toward a platform for extravascular ultrasound imaging. *Theranostics* **2**, 1185 (2012).

36 Hashizume, H., Baluk, P., Morikawa, S., McLean, J. W., Thurston, G., Roberge, S., Jain, R. K. & McDonald, D. M. Openings between defective endothelial cells explain tumor vessel leakiness. *The American journal of pathology* **156**, 1363-1380 (2000).

37 Li, H., Yang, Y., Zhang, M., Yin, L., Tu, J., Guo, X. & Zhang, D. Acoustic characterization and enhanced ultrasound imaging of long-circulating lipid-coated microbubbles. *Journal of Ultrasound in Medicine* **37**, 1243-1256 (2018).

38 Pfeifer, F. Distribution, formation and regulation of gas vesicles. *Nature Reviews Microbiology* **10**, 705-715 (2012).

39 Shapiro, M. G., Goodwill, P. W., Neogy, A., Yin, M., Foster, F. S., Schaffer, D. V. & Conolly, S. M. Biogenic gas nanostructures as ultrasonic molecular reporters. *Nature nanotechnology* **9**, 311-316 (2014).

40 Bourdeau, R. W., Lee-Gosselin, A., Lakshmanan, A., Farhadi, A., Kumar, S. R., Nety, S. P. & Shapiro, M. G. Acoustic reporter genes for noninvasive imaging of microorganisms in mammalian hosts. *Nature* **553**, 86-90 (2018).

41 Farhadi, A., Ho, G. H., Sawyer, D. P., Bourdeau, R. W. & Shapiro, M. G. Ultrasound imaging of gene expression in mammalian cells. *Science* **365**, 1469-1475 (2019).

42 Hurt, R. C., Buss, M. T., Duan, M., Wong, K., You, M. Y., Sawyer, D. P., Swift, M. B., Dutka, P., Barturen-Larrea, P. & Mittelstein, D. R. Genomically mined acoustic reporter genes for real-time in vivo monitoring of tumors and tumor-homing bacteria. *Nature Biotechnology*, 1-13 (2023).

43 Maresca, D., Sawyer, D. P., Renaud, G., Lee-Gosselin, A. & Shapiro, M. G. Nonlinear X-wave ultrasound imaging of acoustic biomolecules. *Physical Review X* **8**, 041002 (2018).

44 Sawyer, D. P., Bar-Zion, A., Farhadi, A., Shivaei, S., Ling, B., Lee-Gosselin, A. & Shapiro, M. G. Ultrasensitive ultrasound imaging of gene expression with signal unmixing. *Nature methods* **18**, 945-952 (2021).

45 Maresca, D., Lakshmanan, A., Lee-Gosselin, A., Melis, J. M., Ni, Y.-L., Bourdeau, R. W., Kochmann, D. M. & Shapiro, M. G. Nonlinear ultrasound imaging of nanoscale acoustic biomolecules. *Applied physics letters* **110**, 073704 (2017).
46 March, J., Rao, G. & Bentley, W. Biotechnological applications of green fluorescent protein. *Applied microbiology and biotechnology* **62**, 303-315 (2003).
47 Chudakov, D. M., Lukyanov, S. & Lukyanov, K. A. Fluorescent proteins as a toolkit for in vivo imaging. *Trends in biotechnology* **23**, 605-613 (2005).
48 Farhadi, A., Sigmund, F., Westmeyer, G. G. & Shapiro, M. G. Genetically encodable materials for non-invasive biological imaging. *Nature materials* **20**, 585-592 (2021).
49 de Gracia Lux, C., Vezeridis, A., Lux, J., Armstrong, A., Sirsi, S., Hoyt, K. & Mattrey, R. Novel method for the formation of monodisperse superheated perfluorocarbon nanodroplets as activatable ultrasound contrast agents. *RSC advances* **7**, 48561-48568 (2017).
50 Kripfgans, O. D., Fowlkes, J. B., Miller, D. L., Eldevik, O. P. & Carson, P. L. Acoustic droplet vaporization for therapeutic and diagnostic applications. *Ultrasound in medicine & biology* **26**, 1177-1189 (2000).
51 Sheeran, P. S., Luois, S., Dayton, P. A. & Matsunaga, T. O. Formulation and acoustic studies of a new phase-shift agent for diagnostic and therapeutic ultrasound. *Langmuir* **27**, 10412-10420 (2011).
52 Liu, J., Shang, T., Wang, F., Cao, Y., Hao, L., Ren, J., Ran, H., Wang, Z., Li, P. & Du, Z. Low-intensity focused ultrasound (LIFU)-induced acoustic droplet vaporization in phase-transition perfluoropentane nanodroplets modified by folate for ultrasound molecular imaging. *International journal of nanomedicine* **12**, 911 (2017).
53 Jing, B., Brown, M. E., Davis, M. E. & Lindsey, B. D. Imaging the activation of low-boiling-point phase-change contrast agents in the presence of tissue motion using ultrafast inter-frame activation ultrasound imaging. *Ultrasound in medicine & biology* **46**, 1474-1489 (2020).
54 Marshalek, J. P., Sheeran, P. S., Ingram, P., Dayton, P. A., Witte, R. S. & Matsunaga, T. O. Intracellular delivery and ultrasonic activation of folate receptor-targeted phase-change contrast agents in breast cancer cells in vitro. *Journal of Controlled Release* **243**, 69-77 (2016).
55 Rapoport, N., Nam, K.-H., Gupta, R., Gao, Z., Mohan, P., Payne, A., Todd, N., Liu, X., Kim, T. & Shea, J. Ultrasound-mediated tumor imaging and nanotherapy using drug loaded, block copolymer stabilized perfluorocarbon nanoemulsions. *Journal of Controlled Release* **153**, 4-15 (2011).
56 Cao, Y., Chen, Y., Yu, T., Guo, Y., Liu, F., Yao, Y., Li, P., Wang, D., Wang, Z. & Chen, Y. Drug release from phase-changeable nanodroplets triggered by low-intensity focused ultrasound. *Theranostics* **8**, 1327 (2018).
57 Rust, M. J., Bates, M. & Zhuang, X. Sub-diffraction-limit imaging by stochastic optical reconstruction microscopy (STORM). *Nature methods* **3**, 793-796 (2006).
58 Betzig, E., Patterson, G. H., Sougrat, R., Lindwasser, O. W., Olenych, S., Bonifacino, J. S., Davidson, M. W., Lippincott-Schwartz, J. & Hess, H. F. Imaging intracellular fluorescent proteins at nanometer resolution. *science* **313**, 1642-1645 (2006).

59 Desailly, Y., Pierre, J., Couture, O. & Tanter, M. Resolution limits of ultrafast ultrasound localization microscopy. *Physics in medicine & biology* **60**, 8723 (2015).
60 Yoon, H., Hallam, K. A., Yoon, C. & Emelianov, S. Y. Super-resolution imaging with ultrafast ultrasound imaging of optically triggered perfluorohexane nanodroplets. *IEEE transactions on ultrasonics, ferroelectrics, and frequency control* **65**, 2277-2285 (2018).
61 Luke, G. P., Hannah, A. S. & Emelianov, S. Y. Super-resolution ultrasound imaging in vivo with transient laser-activated nanodroplets. *Nano letters* **16**, 2556-2559 (2016).
62 Noguchi, A., Ikegaya, Y. & Matsumoto, N. In vivo whole-cell patch-clamp methods: recent technical progress and future perspectives. *Sensors* **21**, 1448 (2021).
63 Chalfie, M., Tu, Y., Euskirchen, G., Ward, W. W. & Prasher, D. C. Green fluorescent protein as a marker for gene expression. *Science* **263**, 802-805 (1994).
64 Fernández-Suárez, M. & Ting, A. Y. Fluorescent probes for super-resolution imaging in living cells. *Nature reviews Molecular cell biology* **9**, 929-943 (2008).
65 Chalfie, M. Green fluorescent protein. *Photochemistry and photobiology* **62**, 651-656 (1995).
66 Feng, G., Mellor, R. H., Bernstein, M., Keller-Peck, C., Nguyen, Q. T., Wallace, M., Nerbonne, J. M., Lichtman, J. W. & Sanes, J. R. Imaging neuronal subsets in transgenic mice expressing multiple spectral variants of GFP. *Neuron* **28**, 41-51 (2000).
67 Jensen, E. C. Use of fluorescent probes: their effect on cell biology and limitations. *The Anatomical Record: Advances in Integrative Anatomy and Evolutionary Biology* **295**, 2031-2036 (2012).
68 Chudakov, D. M., Matz, M. V., Lukyanov, S. & Lukyanov, K. A. Fluorescent proteins and their applications in imaging living cells and tissues. *Physiological reviews* **90**, 1103-1163 (2010).
69 Kobat, D., Horton, N. G. & Xu, C. In vivo two-photon microscopy to 1.6-mm depth in mouse cortex. *Journal of biomedical optics* **16**, 106014 (2011).
70 Kawakami, R., Sawada, K., Sato, A., Hibi, T., Kozawa, Y., Sato, S., Yokoyama, H. & Nemoto, T. Visualizing hippocampal neurons with in vivo two-photon microscopy using a 1030 nm picosecond pulse laser. *Scientific reports* **3**, 1-7 (2013).
71 Lowry, O. H. The quantitative histochemistry of the brain: histological sampling. *Journal of Histochemistry & Cytochemistry* **1**, 420-428 (1953).
72 Araújo, T., Aresta, G., Castro, E., Rouco, J., Aguiar, P., Eloy, C., Polónia, A. & Campilho, A. Classification of breast cancer histology images using convolutional neural networks. *PloS one* **12**, e0177544 (2017).
73 Carovac, A., Smajlovic, F. & Junuzovic, D. Application of ultrasound in medicine. *Acta Informatica Medica* **19**, 168 (2011).
74 Papadacci, C., Pernot, M., Couade, M., Fink, M. & Tanter, M. High-contrast ultrafast imaging of the heart. *IEEE transactions on ultrasonics, ferroelectrics, and frequency control* **61**, 288-301 (2014).

75 Macé, E., Montaldo, G., Cohen, I., Baulac, M., Fink, M. & Tanter, M. Functional ultrasound imaging of the brain. *Nature methods* **8**, 662-664 (2011).
76 Spencer, J. K. & Adler, R. S. Utility of portable ultrasound in a community in Ghana. *Journal of Ultrasound in Medicine* **27**, 1735-1743 (2008).
77 Heckmatt, J., Pier, N. & Dubowitz, V. Measurement of quadriceps muscle thickness and subcutaneous tissue thickness in normal children by real-time ultrasound imaging. *Journal of clinical ultrasound* **16**, 171-176 (1988).
78 Forsberg, F., Merton, D., Liu, J., Needleman, L. & Goldberg, B. Clinical applications of ultrasound contrast agents. *Ultrasonics* **36**, 695-701 (1998).
79 Helfield, B. L. & Goertz, D. E. Nonlinear resonance behavior and linear shell estimates for Definity™ and MicroMarker™ assessed with acoustic microbubble spectroscopy. *The Journal of the Acoustical Society of America* **133**, 1158-1168 (2013).
80 Gao, Z., Kennedy, A. M., Christensen, D. A. & Rapoport, N. Y. Drug-loaded nano/microbubbles for combining ultrasonography and targeted chemotherapy. *Ultrasonics* **48**, 260-270 (2008).
81 Rapoport, N. Y., Kennedy, A. M., Shea, J. E., Scaife, C. L. & Nam, K.-H. Controlled and targeted tumor chemotherapy by ultrasound-activated nanoemulsions/microbubbles. *Journal of Controlled Release* **138**, 268-276 (2009).
82 Rapoport, N. Phase-shift, stimuli-responsive perfluorocarbon nanodroplets for drug delivery to cancer. *Wiley Interdisciplinary Reviews: Nanomedicine and Nanobiotechnology* **4**, 492-510 (2012).
83 Welch, P. J., Li, D. S., Forest, C. R., Pozzo, L. D. & Shi, C. Perfluorocarbon nanodroplet size, acoustic vaporization, and inertial cavitation affected by lipid shell composition in vitro. *The Journal of the Acoustical Society of America* **152**, 2493-2504 (2022).
84 Li, D. S., Schneewind, S., Bruce, M., Khaing, Z., O'Donnell, M. & Pozzo, L. Spontaneous nucleation of stable perfluorocarbon emulsions for ultrasound contrast agents. *Nano letters* **19**, 173-181 (2018).
85 Sheeran, P. S., Wong, V. P., Luois, S., McFarland, R. J., Ross, W. D., Feingold, S., Matsunaga, T. O. & Dayton, P. A. Decafluorobutane as a phase-change contrast agent for low-energy extravascular ultrasonic imaging. *Ultrasound in medicine & biology* **37**, 1518-1530 (2011).
86 Ishijima, A., Yamaguchi, S., Azuma, T., Kobayashi, E., Shibasaki, Y., Nagamune, T. & Sakuma, I. Selective intracellular delivery of perfluorocarbon nanodroplets for cytotoxicity threshold reduction on ultrasound-induced vaporization. *Cancer Reports* **2**, e1165 (2019).
87 Ishijima, A., Tanaka, J., Azuma, T., Minamihata, K., Yamaguchi, S., Kobayashi, E., Nagamune, T. & Sakuma, I. The lifetime evaluation of vapourised phase-change nano-droplets. *Ultrasonics* **69**, 97-105 (2016).
88 Lakshmanan, A., Lu, G. J., Farhadi, A., Nety, S. P., Kunth, M., Lee-Gosselin, A., Maresca, D., Bourdeau, R. W., Yin, M. & Yan, J. Preparation of biogenic gas vesicle nanostructures for use as contrast agents for ultrasound and MRI. *Nature protocols* **12**, 2050-2080 (2017).
89 Bar-Zion, A., Nourmahnad, A., Mittelstein, D. R., Shivaei, S., Yoo, S., Buss, M. T., Hurt, R. C., Malounda, D., Abedi, M. H. & Lee-Gosselin, A. Acoustically

triggered mechanotherapy using genetically encoded gas vesicles. *Nature Nanotechnology* **16**, 1403-1412 (2021).
90 Schneider, M. Characteristics of sonovue™. *Echocardiography* **16**, 743-746 (1999).
91 Goertz, D. E., de Jong, N. & van der Steen, A. F. Attenuation and size distribution measurements of Definity™ and manipulated Definity™ populations. *Ultrasound in medicine & biology* **33**, 1376-1388 (2007).
92 Faez, T., Goertz, D. & De Jong, N. Characterization of Definity™ ultrasound contrast agent at frequency range of 5–15 MHz. *Ultrasound in medicine & biology* **37**, 338-342 (2011).
93 Goertz, D., Frijlink, M., Bouakaz, A., Chin, C., De Jong, N. & Van Der Steen, A. in *IEEE Symposium on Ultrasonics, 2003.* 1503-1506 (IEEE).
94 Hannah, A. S., Luke, G. P. & Emelianov, S. Y. Blinking phase-change nanocapsules enable background-free ultrasound imaging. *Theranostics* **6**, 1866 (2016).
95 Yu, J., Chen, X., Villanueva, F. S. & Kim, K. Vaporization and recondensation dynamics of indocyanine green-loaded perfluoropentane droplets irradiated by a short pulse laser. *Applied Physics Letters* **109**, 243701 (2016).
96 Yin, T., Wang, P., Zheng, R., Zheng, B., Cheng, D., Zhang, X. & Shuai, X. Nanobubbles for enhanced ultrasound imaging of tumors. *International journal of nanomedicine* **7**, 895 (2012).
97 Achmad, A., Yamaguchi, A., Hanaoka, H. & Tsushima, Y. Thin-shelled PEGylated Perfluorooctyl bromide Nanocapsules for tumor-targeted ultrasound contrast agent. *Contrast media & molecular imaging* **2018** (2018).
98 Mountford, P. A. & Borden, M. A. On the thermodynamics and kinetics of superheated fluorocarbon phase-change agents. *Advances in colloid and interface science* **237**, 15-27 (2016).
99 Williams, R., Wright, C., Cherin, E., Reznik, N., Lee, M., Gorelikov, I., Foster, F. S., Matsuura, N. & Burns, P. N. Characterization of submicron phase-change perfluorocarbon droplets for extravascular ultrasound imaging of cancer. *Ultrasound in medicine & biology* **39**, 475-489 (2013).
100 Ji, Y., Zheng, J., Geng, Z., Tan, T., Hu, J., Zhang, L. & Zhang, Y. Controllable formation of bulk perfluorohexane nanodroplets by solvent exchange. *Soft Matter* (2022).
101 Goel, L., Wu, H., Zhang, B., Kim, J., Dayton, P. A., Xu, Z. & Jiang, X. Nanodroplet-mediated catheter-directed sonothrombolysis of retracted blood clots. *Microsystems & nanoengineering* **7**, 1-7 (2021).
102 Moyer, L. C., Timbie, K. F., Sheeran, P. S., Price, R. J., Miller, G. W. & Dayton, P. A. High-intensity focused ultrasound ablation enhancement in vivo via phase-shift nanodroplets compared to microbubbles. *Journal of therapeutic ultrasound* **3**, 1-9 (2015).
103 Aliabouzar, M., Kumar, K. N. & Sarkar, K. Effects of droplet size and perfluorocarbon boiling point on the frequency dependence of acoustic vaporization threshold. *The Journal of the Acoustical Society of America* **145**, 1105-1116 (2019).

104 Yarmoska, S. K., Yoon, H. & Emelianov, S. Y. Lipid shell composition plays a critical role in the stable size reduction of perfluorocarbon nanodroplets. *Ultrasound in medicine & biology* **45**, 1489-1499 (2019).
105 Kawabata, K.-i., Sugita, N., Yoshikawa, H., Azuma, T. & Umemura, S.-i. Nanoparticles with multiple perfluorocarbons for controllable ultrasonically induced phase shifting. *Japanese journal of applied physics* **44**, 4548 (2005).
106 Kang, S.-T., Lin, Y.-C. & Yeh, C.-K. Mechanical bioeffects of acoustic droplet vaporization in vessel-mimicking phantoms. *Ultrasonics sonochemistry* **21**, 1866-1874 (2014).
107 Schad, K. C. & Hynynen, K. In vitro characterization of perfluorocarbon droplets for focused ultrasound therapy. *Physics in Medicine & Biology* **55**, 4933 (2010).
108 Wu, Q., Mannaris, C., May, J. P., Bau, L., Polydorou, A., Ferri, S., Carugo, D., Evans, N. D. & Stride, E. Investigation of the acoustic vaporization threshold of lipid-coated perfluorobutane nanodroplets using both high-speed optical imaging and acoustic methods. *Ultrasound in Medicine & Biology* **47**, 1826-1843 (2021).
109 Mountford, P. A., Thomas, A. N. & Borden, M. A. Thermal activation of superheated lipid-coated perfluorocarbon drops. *Langmuir* **31**, 4627-4634 (2015).
110 Chattaraj, R., Goldscheitter, G. M., Yildirim, A. & Goodwin, A. P. Phase behavior of mixed lipid monolayers on perfluorocarbon nanoemulsions and its effect on acoustic contrast. *RSC advances* **6**, 111318-111325 (2016).
111 Şen, T., Tüfekçioğlu, O. & Koza, Y. Mechanical index. *Anatolian journal of cardiology* **15**, 334 (2015).
112 Chen, W.-S., Matula, T. J., Brayman, A. A. & Crum, L. A. A comparison of the fragmentation thresholds and inertial cavitation doses of different ultrasound contrast agents. *The Journal of the Acoustical Society of America* **113**, 643-651 (2003).
113 Guo, X., Li, Q., Zhang, Z., Zhang, D. & Tu, J. Investigation on the inertial cavitation threshold and shell properties of commercialized ultrasound contrast agent microbubbles. *The Journal of the Acoustical Society of America* **134**, 1622-1631 (2013).
114 Reznik, N., Williams, R. & Burns, P. N. Investigation of vaporized submicron perfluorocarbon droplets as an ultrasound contrast agent. *Ultrasound in medicine & biology* **37**, 1271-1279 (2011).
115 Fabiilli, M. L., Haworth, K. J., Fakhri, N. H., Kripfgans, O. D., Carson, P. L. & Fowlkes, J. B. The role of inertial cavitation in acoustic droplet vaporization. *IEEE transactions on ultrasonics, ferroelectrics, and frequency control* **56**, 1006-1017 (2009).
116 Ferri, S., Wu, Q., De Grazia, A., Polydorou, A., May, J. P., Stride, E., Evans, N. D. & Carugo, D. Tailoring the size of ultrasound responsive lipid-shelled nanodroplets by varying production parameters and environmental conditions. *Ultrasonics sonochemistry* **73**, 105482 (2021).
117 Kripfgans, O. D., Fabiilli, M. L., Carson, P. L. & Fowlkes, J. B. On the acoustic vaporization of micrometer-sized droplets. *The Journal of the Acoustical Society of America* **116**, 272-281 (2004).

118 Shpak, O., Verweij, M., Vos, H. J., de Jong, N., Lohse, D. & Versluis, M. Acoustic droplet vaporization is initiated by superharmonic focusing. *Proceedings of the National Academy of Sciences* **111**, 1697-1702 (2014).
119 Mercado, K. P., Radhakrishnan, K., Stewart, K., Snider, L., Ryan, D. & Haworth, K. J. Size-isolation of ultrasound-mediated phase change perfluorocarbon droplets using differential centrifugation. *The Journal of the Acoustical Society of America* **139**, EL142-EL148 (2016).
120 Ullmann, C., Babick, F. & Stintz, M. Microfiltration of submicron-sized and nano-sized suspensions for particle size determination by dynamic light scattering. *Nanomaterials* **9**, 829 (2019).
121 Paproski, R. J., Forbrich, A., Huynh, E., Chen, J., Lewis, J. D., Zheng, G. & Zemp, R. J. Porphyrin nanodroplets: sub-micrometer ultrasound and photoacoustic contrast imaging agents. *Small* **12**, 371-380 (2016).
122 Borden, M. A., Kruse, D. E., Caskey, C. F., Zhao, S., Dayton, P. A. & Ferrara, K. W. Influence of lipid shell physicochemical properties on ultrasound-induced microbubble destruction. *IEEE transactions on ultrasonics, ferroelectrics, and frequency control* **52**, 1992-2002 (2005).
123 Viitala, L., Pajari, S., Gentile, L., Määttä, J., Gubitosi, M., Deska, J., Sammalkorpi, M., Olsson, U. & Murtomäki, L. Shape and phase transitions in a PEGylated phospholipid system. *Langmuir* **35**, 3999-4010 (2019).
124 Seda, R., Li, D. S., Fowlkes, J. B. & Bull, J. L. Characterization of bioeffects on endothelial cells under acoustic droplet vaporization. *Ultrasound in medicine & biology* **41**, 3241-3252 (2015).
125 Niidome, T., Yamagata, M., Okamoto, Y., Akiyama, Y., Takahashi, H., Kawano, T., Katayama, Y. & Niidome, Y. PEG-modified gold nanorods with a stealth character for in vivo applications. *Journal of Controlled Release* **114**, 343-347 (2006).
126 Diaz, C., Benitez, C., Vidal, F., Barraza, L. F., Jiménez, V. A., Guzman, L., Fuentealba, J., Yevenes, G. E. & Alderete, J. B. Cytotoxicity and in vivo plasma kinetic behavior of surface-functionalized PAMAM dendrimers. *Nanomedicine: Nanotechnology, Biology and Medicine* **14**, 2227-2234 (2018).
127 Xiang, Y., Bernards, N., Hoang, B., Zheng, J. & Matsuura, N. Perfluorocarbon nanodroplets can reoxygenate hypoxic tumors in vivo without carbogen breathing. *Nanotheranostics* **3**, 135 (2019).
128 Sheng, D., Deng, L., Li, P., Wang, Z. & Zhang, Q. Perfluorocarbon nanodroplets with deep tumor penetration and controlled drug delivery for ultrasound/fluorescence imaging guided breast cancer therapy. *ACS Biomaterials Science & Engineering* **7**, 605-616 (2021).
129 Ichihara, M., Shimizu, T., Imoto, A., Hashiguchi, Y., Uehara, Y., Ishida, T. & Kiwada, H. Anti-PEG IgM response against PEGylated liposomes in mice and rats. *Pharmaceutics* **3**, 1-11 (2010).
130 Ishida, T., Wang, X., Shimizu, T., Nawata, K. & Kiwada, H. PEGylated liposomes elicit an anti-PEG IgM response in a T cell-independent manner. *Journal of controlled release* **122**, 349-355 (2007).
131 Suzuki, T., Ichihara, M., Hyodo, K., Yamamoto, E., Ishida, T., Kiwada, H., Ishihara, H. & Kikuchi, H. Accelerated blood clearance of PEGylated liposomes

containing doxorubicin upon repeated administration to dogs. *International journal of pharmaceutics* **436**, 636-643 (2012).
132 Verhoef, J. J. & Anchordoquy, T. J. Questioning the use of PEGylation for drug delivery. *Drug delivery and translational research* **3**, 499-503 (2013).
133 Pozzi, D., Colapicchioni, V., Caracciolo, G., Piovesana, S., Capriotti, A. L., Palchetti, S., De Grossi, S., Riccioli, A., Amenitsch, H. & Laganà, A. Effect of polyethyleneglycol (PEG) chain length on the bio–nano-interactions between PEGylated lipid nanoparticles and biological fluids: from nanostructure to uptake in cancer cells. *Nanoscale* **6**, 2782-2792 (2014).
134 Yoo, K., Walker, W. R., Williams, R., Tremblay-Darveau, C., Burns, P. N. & Sheeran, P. S. Impact of encapsulation on in vitro and in vivo performance of volatile nanoscale phase-shift perfluorocarbon droplets. *Ultrasound in medicine & biology* **44**, 1836-1852 (2018).
135 de Jong, N., Frinking, P. J., Bouakaz, A., Goorden, M., Schourmans, T., Jingping, X. & Mastik, F. Optical imaging of contrast agent microbubbles in an ultrasound field with a 100-MHz camera. *Ultrasound in medicine & biology* **26**, 487-492 (2000).
136 Huynh, E., Leung, B. Y., Helfield, B. L., Shakiba, M., Gandier, J.-A., Jin, C. S., Master, E. R., Wilson, B. C., Goertz, D. E. & Zheng, G. In situ conversion of porphyrin microbubbles to nanoparticles for multimodality imaging. *Nature nanotechnology* **10**, 325-332 (2015).
137 Xu, S., Chang, N., Wang, R., Liu, X., Guo, S., Wang, S., Zong, Y. & Wan, M. Acoustic droplet vaporization and inertial cavitation thresholds and efficiencies of nanodroplets emulsions inside the focused region using a dual-frequency ring focused ultrasound. *Ultrasonics Sonochemistry* **48**, 532-537 (2018).
138 Guo, S., Shi, A., Xu, S., Du, X., Wang, X., Zong, Y., Bouakaz, A. & Wan, M. Lowering of acoustic droplet vaporization threshold via aggregation. *Applied physics letters* **111**, 254102 (2017).
139 Ji, Y., Zheng, J., Geng, Z., Tan, T., Hu, J., Zhang, L. & Zhang, Y. Controllable formation of bulk perfluorohexane nanodroplets by solvent exchange. *Soft Matter* **18**, 425-433 (2022).
140 Chauhan, V. P. & Jain, R. K. Strategies for advancing cancer nanomedicine. *Nature materials* **12**, 958-962 (2013).
141 Yin, T., Wang, P., Zheng, R., Zheng, B., Cheng, D., Zhang, X. & Shuai, X. Nanobubbles for enhanced ultrasound imaging of tumors. *International journal of nanomedicine*, 895-904 (2012).
142 Gong, Z., He, Y., Zhou, M., Xin, H., Pan, M., Fiaz, M., Liu, H. & Yan, F. Ultrasound imaging tracking of mesenchymal stem cells intracellularly labeled with biosynthetic gas vesicles for treatment of rheumatoid arthritis. *Theranostics* **12**, 2370 (2022).
143 Kang, S.-T. & Yeh, C.-K. Intracellular acoustic droplet vaporization in a single peritoneal macrophage for drug delivery applications. *Langmuir* **27**, 13183-13188 (2011).
144 Jung, S., Bang, M., Kim, B. S., Lee, S., Kotov, N. A., Kim, B. & Jeon, D. Intracellular gold nanoparticles increase neuronal excitability and aggravate seizure activity in the mouse brain. *PloS one* **9**, e91360 (2014).

145 Kabalnov, A. S. & Shchukin, E. D. Ostwald ripening theory: applications to fluorocarbon emulsion stability. *Advances in colloid and interface science* **38**, 69-97 (1992).
146 Liu, N., Cui, Y., Khoo, B. & Zhang, A. Damage characteristics of elastic material through a thin membrane using high-intensity focused ultrasound (HIFU). *AIP Advances* **8**, 115123 (2018).
147 Ye, H., Gu, Z. & Gracias, D. H. Kinetics of ultraviolet and plasma surface modification of poly (dimethylsiloxane) probed by sum frequency vibrational spectroscopy. *Langmuir* **22**, 1863-1868 (2006).
148 Füger, P., Hefendehl, J. K., Veeraraghavalu, K., Wendeln, A.-C., Schlosser, C., Obermüller, U., Wegenast-Braun, B. M., Neher, J. J., Martus, P. & Kohsaka, S. Microglia turnover with aging and in an Alzheimer's model via long-term in vivo single-cell imaging. *Nature neuroscience* **20**, 1371-1376 (2017).
149 Trounson, A. & McDonald, C. Stem cell therapies in clinical trials: progress and challenges. *Cell stem cell* **17**, 11-22 (2015).
150 Lee, A. S., Tang, C., Rao, M. S., Weissman, I. L. & Wu, J. C. Tumorigenicity as a clinical hurdle for pluripotent stem cell therapies. *Nature medicine* **19**, 998-1004 (2013).
151 Sneddon, J. B., Tang, Q., Stock, P., Bluestone, J. A., Roy, S., Desai, T. & Hebrok, M. Stem cell therapies for treating diabetes: progress and remaining challenges. *Cell stem cell* **22**, 810-823 (2018).
152 Parmar, M., Grealish, S. & Henchcliffe, C. The future of stem cell therapies for Parkinson disease. *Nature Reviews Neuroscience* **21**, 103-115 (2020).
153 Craig, S. R., Welch, P. J. & Shi, C. Non-Hermitian complementary acoustic metamaterials for lossy barriers. *Applied Physics Letters* **115**, 051903 (2019).
154 Craig, S. R., Welch, P. J. & Shi, C. Non-Hermitian complementary acoustic metamaterials for imaging through skull with imperfections. *Frontiers in Mechanical Engineering* **6**, 55 (2020).
155 Schoen Jr, S., Kilinc, M. S., Lee, H., Guo, Y., Degertekin, F. L., Woodworth, G. F. & Arvanitis, C. Towards controlled drug delivery in brain tumors with microbubble-enhanced focused ultrasound. *Advanced Drug Delivery Reviews* **180**, 114043 (2022).